Towards high-rate magnetron sputter deposition: Influence of the discharge power on deposition process and coating properties

Dipl.-Ing. Christian Saringer

being a thesis in partial fulfilment of the requirements for the degree of a

Doktor der montanistischen Wissenschaften (Dr. mont.)

at the Montanuniversität Leoben

Leoben, September 2017

This work was financially supported by the Austrian Federal Government (in particular from Bundesministerium für Verkehr, Innovation und Technologie and Bundesministerium für Wissenschaft, Forschung und Wirtschaft) represented by the Österreichische Forschungsförderungsgesellschaft mbH within the project SmartCoat-Eco (project number 843621).

Affidavit:

I declare in lieu of oath, that I wrote this thesis and performed the associated research myself, using only literature cited in this volume.

Leoben, September 2017

Acknowledgments

Above all I would like express my gratitude to Prof. Christian Mitterer, head of the Chair of Functional Materials and Materials Systems at the Department of Physical Metallurgy and Materials Testing for offering me the opportunity to conduct the present work in his research group and guiding me so excellently through the maze of science.

I am most grateful to Dr. Robert Franz, my second supervisor at the chair, whose valuable comments and corrections of my writing helped considerably to improve the quality of the included publications. Also, his profound knowledge about plasma were exceptionally helpful in slowly starting to understand this complex topic.

I would like to thank all the colleagues at the Chair of Functional Materials for the casual yet fruitful working atmosphere. Especially I want to put forward the people sharing an office with me: Tanja, Birgit, Stefan, Nikolaus Pascal and Martin, without whom working would not have been half as much fun as it was.

I am also very grateful to the colleagues at the Department of Physics and NTIS at the University of West Bohemia in Pilsen, especially so to Dr. Andrea Pajdarová and Dr. Pavel Baroch. I have learned a lot during my two stays at your department and would not want to have missed it.

At this point I want to gratefully acknowledge the project partners at MIBA HTC, the Technische Universität Wien and the Donau-Universität Krems, who provided valuable input during all the project meetings in the last three years.

My sincerest gratitude is to my diploma student Christoph Oberroither, whose work is an essential part of the present thesis.

I am greatly indebted to my parents Elisabeth and Werner who provided me with all the support necessary for completing a dissertation from the very beginning of my life. Thank you for everything!

The greatest thanks and love, however, I owe to my wife Annemarie. Although it was not always an easy task being by my side you did not lose your patience and kept encouraging me during the hard times. I love you!

Table of contents

1 INTRODUCTION 1

2 PLASMA 3

2.1 Fundamentals of plasma 3

2.1.1 Characteristic plasma properties 4

2.1.2 Glow discharge..6

2.2 Langmuir Probe 8

2.2.1 Principle 8

2.2.2 Druyvesteyn evaluation procedure 10

3 MAGNETRON SPUTTER DEPOSITION 13

3.1 Physical principles 13

3.1.1 Diode sputter deposition..13

3.1.2 Magnetron discharge 14

3.1.3 Bias sputtering 16

3.2 Reactive sputtering..16

3.2.1 Target poisoning and hysteresis 17

4 THIN FILM GROWTH 19

4.1 Fundamentals of film growth..19

4.2 Structure zone model 21

4.3 Residual stresses in thin films 23

4.4 Residual stress measurements of thin films 25

4.4.1 Wafer curvature measurements 25

4.4.2 $\sin^2\psi$ method 27

5 INVESTIGATED COATING MATERIALS....29

5.1 Titanium nitride....29

5.2 Amorphous carbon....31

5.2.1 Raman spectroscopy of amorphous carbon....33

6 SUMMARY AND CONCLUSIONS....35

7 REFERENCES....37

8 PUBLICATIONS....43

8.1 List of included publications....43

8.2 Supervised diploma thesis....43

8.3 My contribution to the included publications....44

Publication I....45

Publication II....71

Publication III....89

Publication IV....109

1 Introduction

In our modern world of ceaseless progress, engineering and functional materials have to meet the ever increasing requirements. The high demands often result in the necessity for opposing surface and bulk properties and frequently the application of surface coatings is the only feasible way for satisfying the specialized needs. Typical fields of use for the mentioned coatings are optical, electrical, mechanical, chemical and decorative applications [1]. Resulting from this need of divergent bulk and surface properties, many different techniques to deposit various kinds of coating materials with different coating thicknesses have been developed up to now [1]. Among these, physical vapor deposition (or PVD) methods are the techniques of choice when thin coatings with a high quality consisting of immiscible elements and/or with specialized functional properties need to be produced in a controllable manner [2]. Magnetron sputter deposition (MSD) is a PVD process that stands out against the others as it shows a reasonable combination of coating surface quality and deposition rate, making it highly interesting for both, research and industry. Nonetheless, MSD is often not used for industrial depositions because of a lack of profitability compared to other methods such as cathodic arc evaporation, for instance, where the lower achievable quality is condoned in exchange for a higher deposition rate. Therefore, increasing the deposition rate for MSD is the key for the synthesis of coatings with good quality at superior productivity, and has hence been the subject of recent research [3–6]. Especially during reactive sputtering, avoiding the undesired poisoning effect (see section 3.2.1) and the consequent loss of deposition rate has led to the development of several, sometimes rather unusual solutions [7–10].

One simple approach to raise the deposition rate, independently of whether the process is reactive or not, is to increase the discharge power supplied to the target. Apart from the hence resulting enhanced productivity, deposition at higher powers has various additional advantages [5]:

- Increased purity of the films due to a reduced contamination from the residual gas in the vacuum chamber;
- For some materials there is the possibility of sputtering without working gas due to a high amount of ionized sputtered atoms (self sputtering [6]);
- Coating deposition on substrates with complex geometries, i.e. into deep trenches for instance, resulting from a lower scattering of sputtered particles with working gas particles;
- Increased influence on the resulting coating texture due to the high deposition rate (amorphous films);

- Higher efficiency of reactive processes as a result of the removal of the reacted film formed on the target surface.

However, MSD is a very complex procedure employing vacuum and plasma, and it can hence be expected, that increasing the deposition power will have a considerable impact on several process aspects, which results in possibly undesired side effects. The mentioned aspects include the plasma, the gas phase transport and the resulting coating properties. Hence, the influence of the discharge power needs to be thoroughly understood in order to be able to fully utilize the potential of an increased target power.

The present work investigates the influence of the discharge power applied to the target on the plasma and coating properties during reactive and non-reactive MSD. For that purpose, several topics are tackled within this work: Spatially resolved Langmuir probe investigations are performed during the sputtering of titanium in argon to determine the dependence of the plasma properties on the discharge power. Furthermore, the influence of the discharge power on the reactive sputtering of titanium in argon and nitrogen, as well as the non-reactive sputtering of carbon in argon and neon is investigated. In this case, a clear dependence of the target poisoning effect and thermal load subjected to the growing film on the discharge power is revealed. Consequently, coatings grown within these two systems at different discharge power levels were analyzed with respect to their structural and mechanical properties. This showed that the influence of the discharge power on the coating properties is strongly dependent on the coating material, thus impeding the establishment of general rules valid for all coating systems.

2 Plasma

2.1 Fundamentals of plasma

Today, there are many plasma assisted thin film deposition techniques. In principle, a plasma is a partly ionized gas, consisting of electrons and ions in an environment of neutral atoms and molecules [11–13]. Similar to the gas phase, in a plasma particles are able to move freely in space, which enables collisional processes to occur. In contrast to the gas state, however, in a plasma not only elastic collisions, but also inelastic collisional processes are important, mainly happening between electrons and atoms [12]. Among these inelastic processes, the most important ones are ionization, and excitation of atoms, as well as relaxation and recombination of ions and electrons. The mentioned relaxation typically results in the emission of photons, which gives the plasma its distinctive glow [11], making it visible to the bare eye. Another point, which distinguishes a plasma from a gas is its good electrical conductivity, being in the same range as for well-conducting metals, such as copper or gold [13]. The plasma state is often referred to as the "*fourth state of matter*" [11,13,14]. As suggested by this term, a plasma can be generated by increasing the temperature of a gas, analogously to heating a solid or liquid in order to melt it up or evaporate it, respectively [14]. For the plasma to evolve, the energies of the species must be in the range of the ionization energy of the present gas species. Therefore, the temperature necessary for the generation of such a "*thermal plasma*" is very high, ranging from approximately 4 000 to 20 000 K, depending on the ionization energy of the present species [14]. However, there exist also

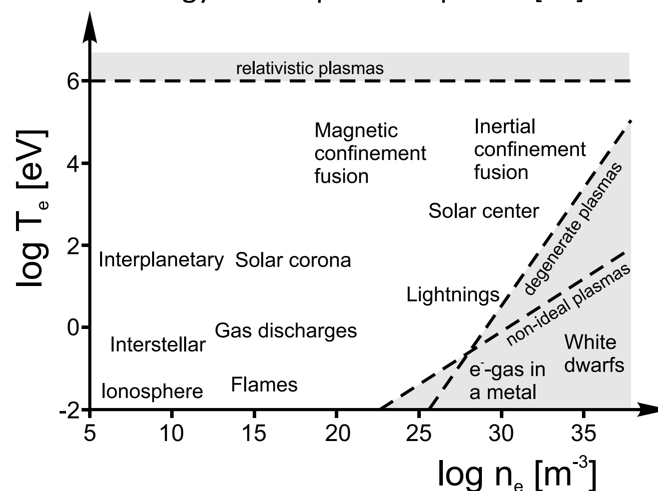

Figure 1: Existence ranges of different plasmas as a function of the electron density n_e and electron temperature T_e. The boundaries for non-relativistic and ideal plasmas are also indicated (redrawn after [11]).

"*non-thermal plasmas*" which can be generated at lower temperatures. One example for such a non-thermal plasma is the electric glow (or gas) discharge [15], see section 2.1.2.

Due to their distinct properties, plasmas are used in several technical applications, ranging from materials processing techniques such as etching or coating deposition [14], over medical applications [16,17] to nuclear fusion [18,19]. Plasmas are also quite abundant in nature and it is assumed, that more than 99% of the visible matter in the universe is in plasma state [13]. Figure 1 gives an overview of different plasmas as a function of the plasma density and electron temperature. These parameters are introduced in the following section.

2.1.1 Characteristic plasma properties

Plasma density

A plasma can be described by the amount of charged particles present. Electron density n_e and ion density n_i are the number of electrons and ions per volume, usually given in cm^{-3} or m^{-3}. One of the distinct properties of a plasma is the so-called quasineutrality, i.e. on the average the number of negative and positive charges is equal [11]:

$$n_e = \sum Z_{i,k} n_{i,k} \,. \tag{1a}$$

Here, $Z_{i,k}$ is the charge state of the ion k. For a plasma with just singly charged ions that yields [11–13]

$$n_e \cong n_i = n_P \,, \tag{1b}$$

where n_P is the so called plasma density. The plasma density can span several orders of magnitude, from close to zero for interplanetary plasmas up to 10^{18} cm^{-3} for high pressure arcs [13].

Degree of ionization

As mentioned above, a plasma consists of neutral as well as charged particles. The ratio of ions to neutral atoms and molecules is the degree of ionization x_{iz} [14]:

$$x_{iz} = \frac{n_i}{n_g + n_i} \,, \tag{2}$$

where n_g is the neutral gas density. x_{iz} ranges from 10^{-7} for weakly ionized plasmas to close to unity for fully ionized plasmas, such as those encountered in nuclear fusion [13,14].

Electron and ion temperature

In order to characterize the kinetic energy of the charged particles, their respective temperatures are used [12]:

$$\frac{1}{2} m_n \bar{v}_n^2 = \frac{3}{2} k T_n \, . \quad (3)$$

Here, m_n, $\bar{v}_n$ and T_n are the mass, the mean speed and the temperature of species n, and k is the Boltzmann´s constant. Conveniently, these temperatures are given in electron Volts instead of Kelvin (1 eV ≈ 11,600 K) [20]. In contrast to the ion and electron densities, the temperatures do not necessarily take up the same value. In many plasmas the electron temperature is much higher than the ion temperature: $T_e \gg T_i$. Since electrons and ions/neutrals are not in thermodynamic equilibrium in this case, such plasmas are referred to as non-thermal plasmas [20].

Electron energy distribution/probability functions

Naturally, the electrons in a plasma do not have one single energy, but adopt a distribution of different energies. This distribution is called the electron energy distribution function $f(E)$, or EEDF, representing the number of electrons for each energy E [13]. The EEDF depends strongly on the collisions taking place in the plasma. In many plasmas, the EEDF takes the form of a Maxwell distribution. However, especially for non-elastic energy ranges in gas discharges different EEDFs are found [21]. A distribution that is frequently encountered for such conditions is the so-called Druyvesteyn distribution [20,21]. In order to visualize the EEDF, a different function, termed the electron energy probability function $g(E)$, or EEPF is often used [22]. Both are closely related via [22,23]

$$g(E) = f(E)/\sqrt{E} \, . \quad (4)$$

This function has the advantage of directly showing deviations from a Maxwellian distribution as a divergence from linear behavior in the semi logarithmic plot $\log\{g(E)\}$ vs E.

Sheath formation

Inevitably, a technical plasma is in contact with some constructive surrounding confining the plasma, like a nozzle or vacuum chamber for instance. Consequently, the surrounding object is in contact with the charge carriers in the plasma, i.e. electrons and ions arrive at its surface. This leads to the generation of a thin positively charged layer separating the plasma from the object, called sheath (Fig.2). There the ion and electron densities are not equal, as in

the bulk of the plasma [12,14]. Due to the difference in mass, the electrons typically have a much higher average speed than the ions and they hit the object with a higher current density [12]. Therefore, the electron density decreases stronger than the ion density in the vicinity of the object and n_i becomes larger than n_e. This leads to the development of a potential difference repelling the electrons from and attracting the ions towards the object [14]. The plasma thus gathers a positive potential with respect to the object, which is termed the plasma or space potential V_P. The object in contact with the plasma might be grounded, as typical for a vacuum chamber. If the object, however, is electrically insulated the arriving electron current leads to a negative charging of the so-called "*floating*" object. The gathered potential is consequently termed the floating potential V_{fl}.

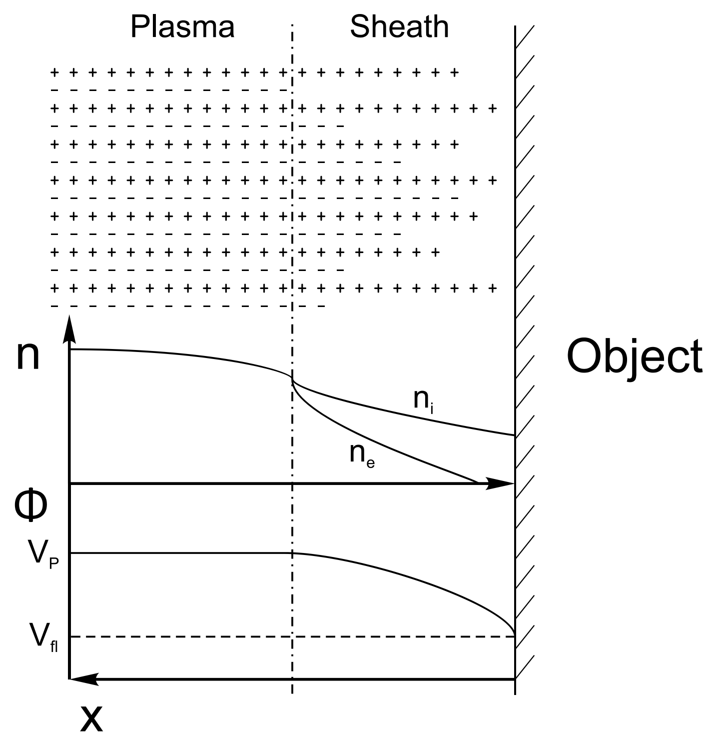

Figure 2: Sheath developed between a plasma and the surface of a floating object. (+) indicates an ion while a (-) represents an electron. Particle density n (ion density n_i and electron density n_e) and potential Φ are indicated as a function of the distance x (reproduced after [12,14]).

2.1.2 Glow discharge

As mentioned above, one example for a plasma is the electric glow discharge [12,13,15]. Glow discharges are widely applied for several technical applications, including thin film deposition, etching, medical applications and room lighting [13,16,24,25], just to name a few. For the ignition of the discharge, two electrodes are inserted into a low-pressure gas and a negative voltage V_C of a few hundred Volts is applied to the cathode [12,14], see Fig.3a. This voltage can be a direct current (DC) voltage, a pulsed DC voltage or radio frequency (rf)

voltage [15]. A few free electrons are always present in the background gas due to ionization caused by cosmic rays or radioactivity. These electrons are accelerated towards the positive anode by the electric field resulting from the cathode voltage [12,15]. On their way the electrons, before being absorbed at the anode, may ionize atoms, which are then in turn accelerated towards the negative cathode. At the cathode, the ions cause the emission of additional electrons, called secondary electrons [12,14]. The emitted electrons ionize atoms by the energy they gain from the high electric fields in the cathode sheath. This results in an avalanche of ionization processes and the number of electrons grows exponentially with the distance from the cathode, with the corresponding exponent α being known as the first Townsend coefficient [14]. Given by continuity, the ion flux towards the cathode must balance the electron current leaving the cathode region at the sheath edge at distance d minus the secondary electron emission at the cathode surface. This is known as breakdown condition [14] and the following equation must be satisfied

$$\alpha d = \ln\left(1 + \frac{1}{\gamma_{SE}}\right), \tag{5}$$

with γ_{SE} being the secondary electron emission coefficient.

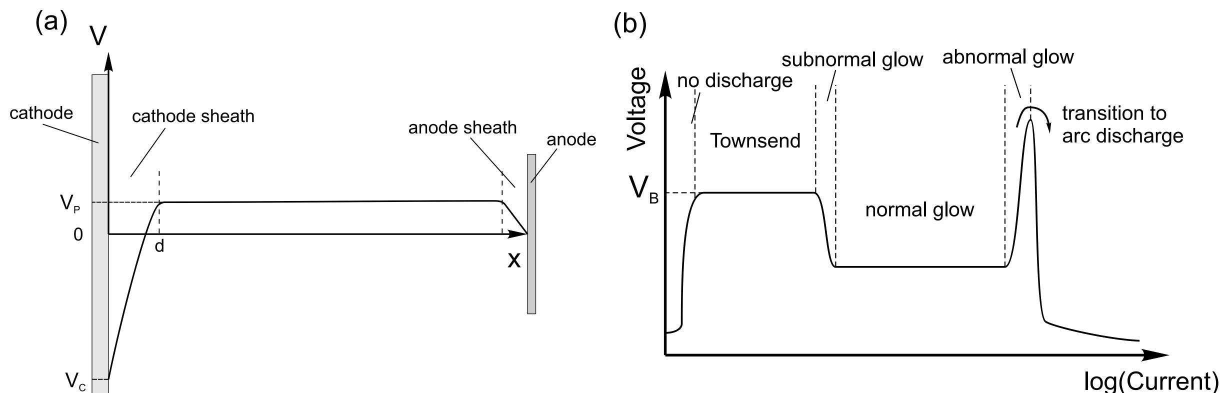

Figure 3: Voltage V as a function of the distance x between cathode and anode in a DC glow discharge (a). Voltage-current characteristic of a DC glow discharge (b). V_B is called the break down voltage (after [12,13]).

Depending on the current, different types of discharges can be distinguished. Figure 3b shows a typical current-voltage characteristic of a DC glow discharge. The critical voltage, below which equation 5 is not satisfied and no self-sustained discharge is formed is called the break down voltage V_B. The following region, where a stable discharge is first established is known as the Townsend-dark glow. As suggested by the name, there is no visual glow present, which is due to a very low plasma density. The voltage in this region does not depend on the current and an external electric field applied to the plasma is undisturbed. When the current

is increased above a certain limit, an external field, however, is redistributed leading to the formation of a cathode sheath and the transition from dark Townsend to glow discharge (subnormal glow). Due to the redistribution, not the whole cathode is covered in the normal glow region and the voltage is lower. The normal glow is characterized by a constant current density, which means that with increasing current only the area of the cathode spot is growing, while the voltage stays constant. As soon as the whole cathode is covered by the current conducting spot, the abnormal glow region is entered. There, an increase of the voltage results in an increased current density. If the voltage/current is further increased, the thermionic emission of electrons increases due to a heating of the target and at some point the discharge transforms to an arc discharge. A low cathode voltage with an exceedingly high current density is characteristic for this type of discharge [13,24].

2.2 Langmuir Probe

2.2.1 Principle

The Langmuir probe was developed by Irving Langmuir and co-workers in the 1920´s [21,26,27], practically at the same time when Langmuir introduced the term "*plasma*" for the region of equal numbers of ions and electrons in a glow discharge [13]. This technique is one of the simplest plasma characterization tools. It is based on the estimation of the charged particle flux towards a small metal probe, that is brought directly in contact with the plasma [11,12,26]. The measurement is based on the determination of the current-voltage characteristic – also termed probe characteristic – of a circuit of two electrodes [26]. Two different cases are distinguished [11,26,28,29]:

(a) The first electrode is the probe and the second one is the chamber wall. Here, the difference in the surface of the two electrodes is several orders of magnitude and the reference potential is the ground potential of the chamber wall. This setup is termed single probe.

(b) Two small electrodes with comparable or same surface area are inserted into the plasma. This configuration is called double probe and is typically used when there is no well-defined ground electrode in the plasma [14] or with rf plasmas [29].

Setup (a) is the most commonly employed and is in the focus of the following section.

The Langmuir probe can have several different geometries (see Fig.4a), however, the most widely used type is the cylindrical probe [26]. In order to have a defined area in contact with the plasma, the connection towards the probe is covered by an insulation, which is represented by the grey shaded area in Fig.4a. Figure 4b shows the resulting probe characteristics for a single probe for the different probe geometries. In general, three different regions can be defined, irrespective of the probe geometry [26,28,30]. When the potential is strongly negative, the positively charged ions are accelerated towards the probe and essentially an ion current is measured. Therefore, $|I_i/I_e| \gg 1$ in this region, where I_i and I_e are the ion and electron current at the probe surface, respectively. On the other hand, at strongly positive probe potentials the ions are repelled and the electrons are attracted towards the probe ($|I_i/I_e| \ll 1$). These two regions are called the ion and electron acceleration (or saturation) regions [26]. Situated between the ion acceleration region and the plasma potential V_P, is the transition region, where $|I_i| \approx |I_e|$. Within this part of the characteristics the floating potential is located, which can easily be determined, as the ion and electron current balance each other and the resulting net current is zero. All three regions carry information on the plasma, however, an analysis of the transition region is the most advantageous, because there less restrictive limitations are encountered [30].

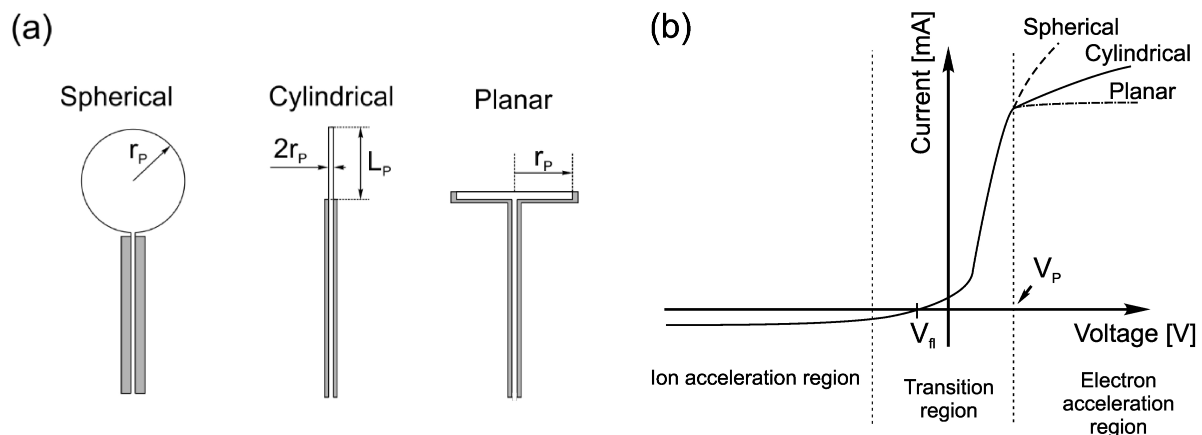

Figure 4: (a) Typical Langmuir probe geometries. r_P is the probe radius and L_P is the probe length. (b) Probe current-voltage characteristics for the three different geometries in (a) (after [11,26,28]).

Additionally to the floating potential, the Langmuir probe is able to yield several plasma parameters, including plasma density, plasma potential and electron temperature [11,14,26,28,29]. However, since the probe is in direct contact with the plasma it represents a serious perturbation and as soon as the probe potential differs from the plasma potential, a sheath is formed around the probe [11,31], similar to the sheath presented in Fig.2. That means, that the actual surface of the probe is not its geometrical surface, but of the probe and the sheath together [12]. In order to minimize the plasma perturbation, the probe

therefore needs to be as small as possible [23,26], so that the following inequalities are satisfied [23,28]:

$$r_P \, ln\left(\frac{\pi L_P}{4r_P}\right), r_H, \lambda_D \ll \lambda_e, \tag{6}$$

with r_P and r_H being the radius of the probe and probe holder, respectively. L_P is the length of the probe, λ_D the Debye length (the characteristic parameter for the size of plasma perturbations) and λ_e is the mean free path of the electrons. The perturbation is also dependent on the probe geometry, which can particularly be seen for the electron acceleration region in Fig.4b. An increased positive voltage leads to an increase in sheath thickness and consequently to a higher electron current in the case of a spherical or cylindrical probe geometry [11,14,31].

Most probe theories (including the standard Langmuir procedure) were developed and are only valid for a Maxwellian EEDF [14,21]. This is often not the case in technical plasmas, including glow discharges [21,32] and magnetron sputtering discharges [33]. However, there exists an evaluation method, which directly determines the EEDF from the probe characteristic. This method is known as Druyvesteyn procedure [21,26,34] and is described in the following section.

2.2.2 Druyvesteyn evaluation procedure

The basis for EEDF measurements using a Langmuir probe is the Druyvesteyn formula [14,30]:

$$f(E) = f(V_P - V) = \frac{2m_e}{eA}\sqrt{\frac{2e(V_P - V)}{m_e}} I_e^{"}, \tag{7}$$

where E is the electron energy, V is the probe voltage and $I_e^{"}$ is the second derivative of the electron current with respect to V, m_e is the electron mass, e is the electron charge and A is the probe area. In order to be collected at the probe, an electron needs to overcome the potential difference between plasma and probe. Therefore, its energy in electron Volts is equal to the potential difference $V_P - V$. V_P can be determined as the point where $I_e^{"}$ equals zero [26,35], see Fig.5. Since the probe characteristic is the sum of the ion and electron contributions, also the second derivative consists of both currents and $I^{"} = I_i^{"} + I_e^{"}$ [23]. However, the contribution of the ion current is usually much smaller than of the electron current [30] and can thus be neglected for the evaluation and $I_e^{"} \cong I^{"}$. From the known EEDF, the electron density can be calculated by integrating over all electron energies [14,21,26]

$$n_e = \int_0^\infty f(E)dE. \tag{8}$$

When EEDF and n_e are calculated the average electron energy $\bar{E}$ follows as [14]

$$\bar{E} = \frac{1}{n_e}\int_0^\infty E\, f(E)dE. \tag{9}$$

In the case of a Maxwellian plasma, T_e equals $^2/_3$ of $\bar{E}$. In analogy to that, an effective electron temperature $T_{e,eff}$ for the case of an arbitrary, isotropic EEDF can be defined [14,21]

$$T_{e,eff} = \frac{2}{3}\bar{E}. \tag{10}$$

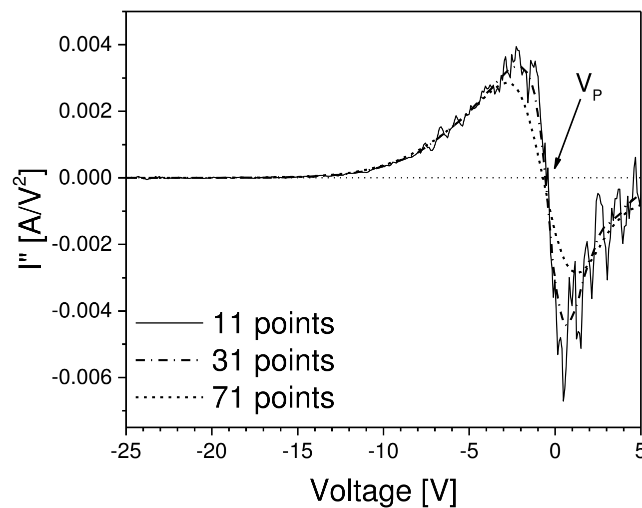

Figure 5: Influence of the size of the fitting window for the determination of the second derivative of a single-probe characteristic using Savitzky-Golay filtering (own work).

The critical point of this evaluation procedure is the determination of the second derivative, since any noise stemming from the plasma is augmented by differentiation [21]. There are two principal groups of methods [26]: (1) measuring the second derivative directly, also known as online methods. These are based on creating a second harmonic or using analog differentiators with a sawtooth or stepwise-like voltage signal. And (2) offline methods which are based on algorithms of numerical analysis, a numeric solution of the integral equation [26] or on digital filtering [26,36]. Figure 5 shows the influence of the size of the fitting window for a digital Savitzky-Golay filtering [37] of the probe characteristic with subsequent differentiation. It can be seen, that a smoothing is necessary in order to obtain reasonable results (compare the curves for 11 and 31 points). However, excessive smoothing leads to an intolerable distortion of the curve (31 and 71 points). In spite of the fact, that determining the second derivative is challenging without influencing the results, the Druyvesteyn procedure

has several advantages compared to the standard technique [14]: (a) It is valid for any isotropic electron distribution including non-Maxwellian distributions. (b) It is valid for any convex probe geometry, i.e. all geometries shown in Fig.4a. And (c), the ratio of probe dimension to Debye length is not important.

3 Magnetron sputter deposition

Magnetron sputter deposition (MSD), or more briefly magnetron sputtering, is a plasma assisted thin film deposition technique that belongs to the rather extensive group of physical vapor deposition (PVD) methods [2]. Since several decades it has been successfully used in industry and research for the deposition of virtually all kinds of different functional coatings [38,39]. Within the strengths of MSD are its flexibility and the ability of depositing coatings under strongly non-equilibrium conditions. This allows the deposition of almost any coating material and even immiscible elements can be brought together in solid solutions with properties that are not achievable with bulk materials. Due to the unique possibilities MSD was and still is the subject of extensive research and several books and review articles are available focusing on MSD [2,12,14,38–44].

3.1 Physical principles

3.1.1 Diode sputter deposition

Diode sputter deposition, which is the fundament for MSD, is based on the physical process termed sputtering, which is the evaporation of atoms by the momentum transfer of particles bombarding the surface of a solid target material [2]. The bombarding particles are ions originating from a gas discharge (usually argon is used as process gas [39]), in which the cathode is the material to be evaporated, termed the target. When an ion hits the solid surface of the target, several processes may occur [12], see Fig.6. Ions may be reflected or incorporated [2], which, however, does not contribute to the evaporation of the target material. Furthermore, secondary electrons are occasionally emitted sustaining the discharge [38]. The process causing atoms in the solid state to evaporate, however, is the collision cascade [42]. This is a series of collisions taking place under the target surface. A collision cascade leading to the emission of a target atom is depicted in Fig.6 and works as follows [42]: An incoming ion hits the surface, where its energy gathered in the cathode sheath is transferred to the atoms in the first few layers under the target surface. The delivered energy is converted into a number of low-energy recoils of the target atoms. Most of these recoils are directed towards the target, but some of the recoiling target atoms get an impulse towards the surface. If their energy exceeds the surface binding energy, they leave the target and are transferred into the vapor phase. The characteristic parameter for this process is the sputter yield, i.e. the average number of atoms ejected per incoming ion [12,40]. The sputter yield

depends on several parameters including pressure, ion energy, ion to atom mass ration, incoming angle and surface energy [40,41].

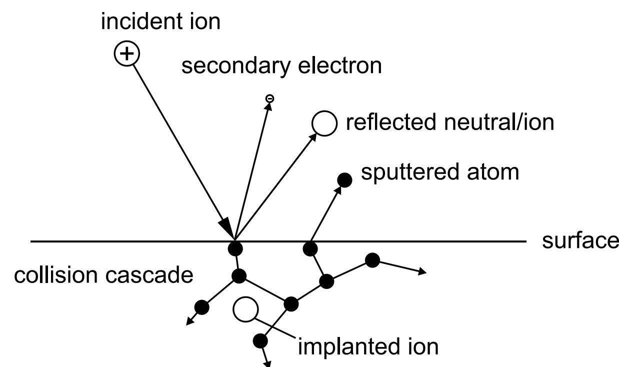

Figure 6: Processes taking place between bombarding ions and a bombarded surface (after [12]).

3.1.2 Magnetron discharge

Diode sputtering has become obsolete as a deposition process nowadays due to several drawbacks, including a low ionization efficiency of the plasma, large substrate heating effects and a low deposition rate [38,40]. These shortcomings led to the invention of the magnetron, the basic principle of which can be seen in Fig.7. The term "*magnetron*" refers to the installation of magnets behind the target. These magnets generate a magnetic field in front of the target confining the secondary electrons emitted at the target surface due to the ion bombardment [38]. For an optimized electron confinement the magnetic field needs to be parallel to the substrate surface. Hence, there are two magnetic rings installed in a typical planar circular target, one outer and one inner pole ring of opposite polarization to generate a closed magnetic field configuration [39]. The most intense plasma region is formed where the electric field $\vec{E}$ and magnetic field $\vec{B}$ are perpendicular. There the confined electrons start to drift along the target surface as a result of the Lorentz force, which is also known as $\vec{E} \times \vec{B}$ drift. The resulting drift current is called Hall current and it usually exceeds the actual discharge current considerably [39,45]. Due to this high electron current more ions are produced in the vicinity of the target by electron impact ionization, leading to an increased ion current at the target which then raises the sputtering rate significantly [40]. Furthermore, magnetron discharges can be sustained at lower pressures compared to the diode setup. When the pressure is decreased, the atoms experience fewer collisions and arrive at the target with a lower degree of thermalization, i.e. with a higher energy [2]. The degree of thermalization can thus be adjusted in a wider range by varying the pressure.

However, magnetron sputtering suffers from two main drawbacks [2]: The first disadvantage is, that in the conventional magnetron the plasma is only confined close to the target and no energetic particles originating from the plasma, which are necessary for activating chemical processes, arrive at the substrate holder. This is needed for reactive sputtering, for instance [2] (see section 3.2). This issue was overcome by the introduction of the unbalanced magnetron as depicted in Fig.7 [46–48]. In the unbalanced configuration, some magnetic field lines extend to the substrates enabling the electrons to follow them, expanding the plasma to the vicinity of the substrate. This enhances the ion bombardment on the growing film. The second, probably more severe disadvantage, is the non-uniform target erosion. Consequently, two problems arise [2]: Firstly, the sputtering rate and consequently the deposition rate depend on the position of the substrate relative to the target. And secondly, the target usage is strongly non-linear, which leads to a low target utilization of sometimes only 10 - 30 %. There are magnetron configurations which allow for a much better target utilization, in particular the cylindrical rotary magnetron [49,50] or the high target utilization sputtering setup [51].

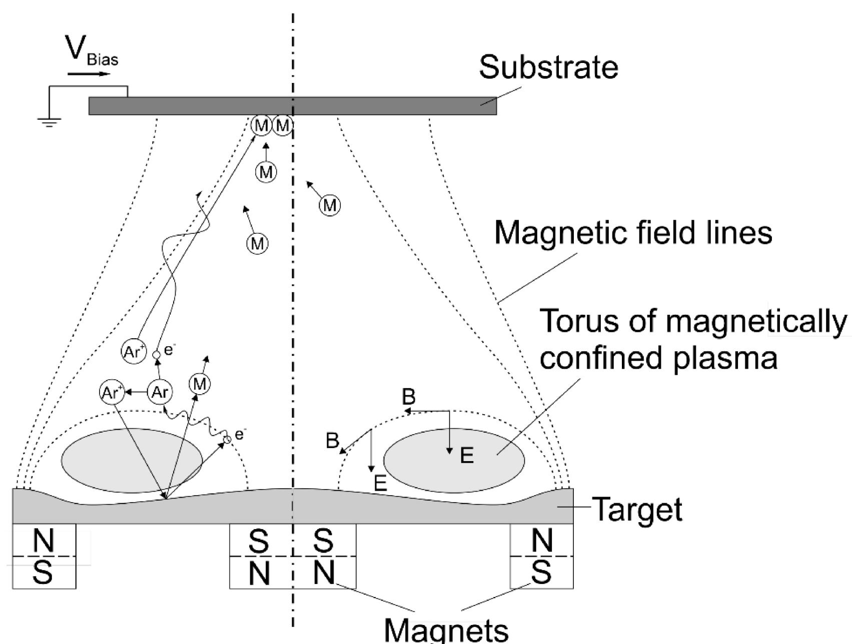

Figure 7: Basic principle of an unbalanced magnetron sputtering discharge with a planar circular target. B and E are the magnetic and electric field, respectively. The bombardment of the metallic target by argon ions (Ar^+) leads to the emission of metal atoms (M) and secondary electrons (e^-), which gyrate around the magnetic field lines causing the ionization of other argon atoms (Ar). Some electrons follow the magnetic field lines towards the substrate expanding the plasma to the vicinity of the substrate. This results in an enhanced ion current at the growing film during growth, which can be influenced by applying a bias voltage U_{Bias} (reproduced after [39,48]).

3.1.3 Bias sputtering

Due to the plasma present, the film growing on the substrate is subjected to a considerable bombardment of all types of different plasma particles [52]. Since the nucleation and resulting film properties strongly depend on the type and energy of the arriving species, see section 4, influencing them will have a significant effect on the resulting film properties. Modifying the neutral particle behavior directly, however, is very difficult, but the charged particles can be influenced quite easily by applying a voltage to the substrate, known as bias voltage [12,41] (Fig.7). In principle both, negative and positive voltages can be applied to the substrate. If it is biased positively, the plasma potential around the substrate will increase until the resulting loss of electrons is compensated for, while the ion current does not change. This leads, however, to an increased electron current significantly raising the thermal load of the substrate. If it is biased negatively on the other hand, the situation becomes similar to the situation at the target, and ions are accelerated towards the substrate, with all accompanying effects such as sputtering, ion implantation and heating, but typically at lower intensity [40]. The low intensity ion bombardment is beneficial for the coating properties [48] and is known to improve coating adhesion, to densify the coatings and to lead to a finer grain size [41]. Other properties controlled by the bias can be resistivity, hardness, gas content and residual stress [12,41].

3.2 Reactive sputtering

In addition to the deposition of materials purely from a solid target, MSD offers the possibility of growing compound coatings from a metallic target in a reactive gas atmosphere. This process is called reactive MSD [53–55]. By this technique a large variety of compounds can be deposited including oxides, nitrides, fluorides, carbides and arsenides [39,54], just to name a few. Reactive MSD sometimes even seems to be the only reasonable way to produce some of the materials, since the compound, if it is an oxide for instance, might be non-conductive and could therefore not be used as cathode for a DC glow discharge [12]. An rf or pulsed excitation would be necessary in this case, which is considerably more expensive and more complicated [39,54].

As already mentioned a metallic target, for instance titanium or aluminum, is used for reactive MSD, while the reactive component is added to the working gas (argon). Typically employed reactive gasses are nitrogen, oxygen, hydrocarbons, or any combinations of those [41]. The use of elemental targets has several advantages compared to ceramic targets [54].

Metallic targets are manufactured and machined more easily and can be produced with a higher purity. Also, they show a higher heat-conductivity and bonding is less difficult, which makes them heat-conductive, enabling a more efficient cooling. And, as already mentioned above, metallic targets are electrically conductive which avoids the use of expensive rf equipment.

3.2.1 Target poisoning and hysteresis

Despite all its merits, reactive MSD is an inherently instable process and it suffers from one large drawback, the so called "*target poisoning*" effect [48,54–58]. The main issue that needs to be considered with target poisoning is, that it results in the undesired hysteresis-like dependence of several process parameters on the reactive gas flow [54,55], as systematically shown in Fig.8. Basically, two different modes of operation can be identified, one mode at low reactive gas flow rates, also referred to as metallic mode, and one mode that is present at high reactive gas flow rates, called poisoned mode. In between is the transition region, which is strongly non-linear and shows the said hysteresis behavior. In the metallic mode, i.e. at low reactive gas flow rates, all reactive gas is gettered by the sputtered metal atoms. Hence, no reaction of the reactive gas with the target surface takes place and the absolute pressure in

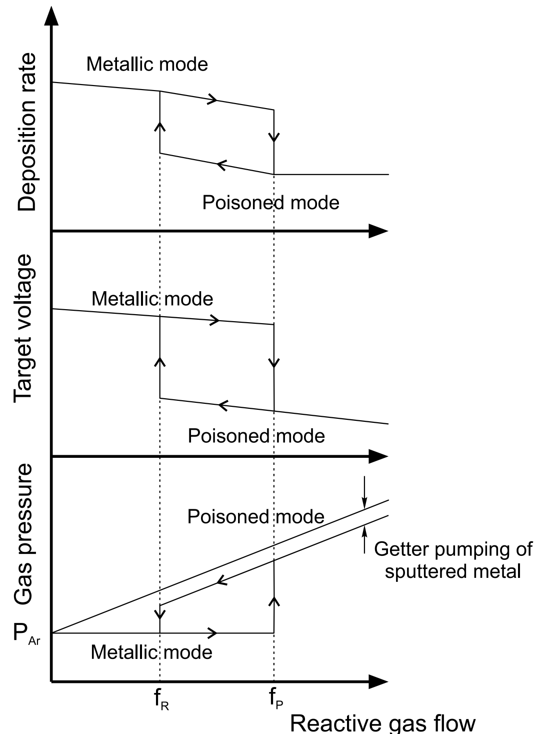

Figure 8: Hysteresis effect during reactive sputtering. The arrows indicate the direction of the change in reactive gas flow, i.e. increase or decrease. P_{Ar} is the argon partial pressure, f_P and f_R are the gas flows where target poisoning and recovering, respectively, occur (redrawn after [54,55]).

the chamber is constant, even at increasing reactive gas flow. Furthermore, the deposition rate remains high and practically independent of the reactive gas present. Unfortunately, however, the resulting coatings are substoichiometric and do not exhibit the desired composition [59].

When the reactive gas flow is increased, at some instant a critical point is reached, which is indicated as f_P in Fig.8. There, the reaction product forms at the metal target covering its surface and the process switches from the metallic to the poisoned, or compound mode. Not all of the gas can be gettered by the sputtered material anymore, which results in an abrupt and irreversible change of the pressure. Accompanied by the formation of the compound on the target surface, the secondary electron emission coefficient γ_{SE} is changing as well. Usually, γ_{SE} is higher for the compound, thus resulting in a lower voltage [41,54]. A higher γ_{SE} also means that more energy of the arriving ions is put into the breaking of bonds and the emission of secondary electrons. This, with a lower sputter yield of the compounds leads to a decreased deposition rate for the poisoned mode [54]. The decrease can be quite severe – typical factors for the deposition with nitrogen are around 3-4 and around 10-15 for oxide deposition [55]. However, in the poisoned mode the resulting coatings usually have a stoichiometric composition. A further increase of the reactive gas flow is accompanied by a linear rise of the reactive gas partial pressure. When the flow is reduced the pressure is similarly decreasing again. The de-poisoning or recovery of the target surface, i.e. the removal of the reactive compound, does, however, not occur at f_P, but at a considerably lower value f_R. This is owing to the reduced sputtering rate because less material is available for gettering the present reactive gas in the compound mode thus shifting the transition to lower values.

By conventional methods the transition region is inaccessible for deposition, although it would be the ideal case, since stoichiometric compounds could be formed at high deposition rates [54]. Therefore, much research focuses on the investigation of reactive MSD. There are several models describing this process, e.g. the well-known Berg model [60]. Also several approaches were developed to circumvent the hysteresis including increasing the pumping speed [53,54], gas pressure or flow control by optical emission spectroscopy or voltage monitoring [10,54,61], decreasing the target erosion area [9], increasing the target to substrate distance [62], localized gas addition [63], the “baffled target” approach [7], increasing the inert gas pressure [59] and the use of substoichiometric targets instead of purely metallic [8]. Some of these methods are, however, difficult and/or expensive to implement.

4 Thin film growth

Thin film deposition by PVD-methods generally takes place under non-thermodynamic equilibrium conditions [64,65]. In thermodynamic equilibrium the rates of opposing processes, like for instance condensation and evaporation, are the same and both processes consequently sum up to zero. Therefore, no film growth can take place in thermodynamic equilibrium, since for the formation of a film the condensation rate must be higher than the evaporation rate [65]. Also, deposition temperatures are often quite low around 0.2-0.3 T_m, where T_m is the melting temperature of the condensing coating material (in Kelvin), hindering diffusion [64]. Due to these reasons, film growth is a kinetically driven process. In return, the kinetic limitations during film formation allow the synthesis of metastable phases and artificial structures that would otherwise not be achievable [64].

4.1 Fundamentals of film growth

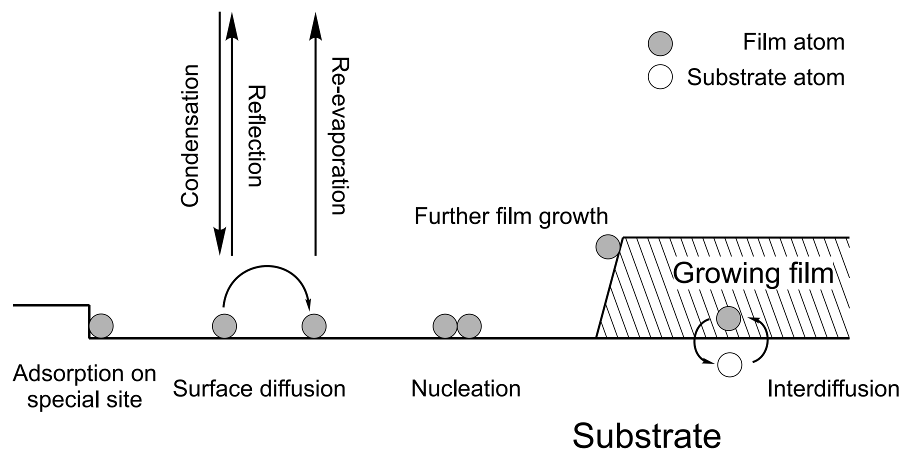

Figure 9: Schematic representation of the processes occurring during film growth (after [65]).

Figure 9 shows the atomic processes going on in the initial stage of film growth under vacuum conditions: Atoms can undergo two different processes upon arriving at the substrate: They may either be reflected directly or be loosely adsorbed becoming so-called adatoms. As adatoms they diffuse over the surface exchanging energy with the lattice or other adsorbed particles until they re-evaporate after some time or eventually become trapped at low-energy sites, like edges or defects, or at sites where the surface chemistry is different [2,52,65]. The migration of the atoms on the surface is governed by their surface mobility, which is dependent on the energy of the arriving atom, chemical interactions and thermal energy of the substrate surface [2]. The activation energy necessary for the migration depends on the melting temperature for both, surface and bulk diffusion. Since the surface atoms have fewer bonds to other atoms, the activation energy for surface diffusion is much less [40]. One

important process connected with bulk diffusion is the so called interdiffusion between film and substrate. This process is responsible for the smoothening of the substrate-film interface [65].

Despite diffusion and the adsorption at special sites, atoms may congregate on the surface to form so-called nuclei, small clusters of several atoms. This process is termed nucleation. In order to form a dense film and to obtain a good contact to the surface the number of nuclei per area, or nucleation density, needs to be high [2]. In the early growth stages these nuclei coalesce leading to a decrease in the nucleation density, which then denudes the substrate allowing further nucleation to take place. This coalescence continues until a network with unfilled channels in between evolves. These channels fill up during the subsequent deposition until only voids remain which, eventually, also become filled and a continuous film is formed [41].

For film growth, three characteristic growth modes are encountered, displayed in Fig.10a [65,66]. In the layer by layer growth, also known as Frank-van der Merve mode, a new layer only forms when the former one is completed. This mode can be found for semiconductor growth on semiconductors, for instance [66]. The second mode is called Vollmer-Weber, or island growth mode. Here, the film grows as several islands, which are formed at various positions on the substrate building up a continuous film through growing and subsequent coalescence [41]. Which one of these modes evolves depends on the interaction between substrate and film atoms [41,65]. If the interaction between film and substrate atoms is larger than the interaction between the film atoms, layer growth occurs. The opposite case, i.e. the interaction between the deposited film atoms is greater, leads to the formation of islands and the growth in the island mode. This interaction can be described by the surface and interface energies, see Fig.10b [65]. The force equilibrium in this situation can be expressed as

$$\gamma_S = \gamma_{S/F} + \gamma_F \cdot cos\phi. \qquad (11)$$

Here, γ_S, γ_F and $\gamma_{S/F}$ are the surface free energies between substrate and vacuum, deposit and vacuum and substrate and deposit with ϕ being the contact angle. For the two different growth modes the conditions are [65]

(i) Layer growth: $\phi = 0,\ \gamma_S \geq \gamma_F + \gamma_{S/F}$ (12a)

(ii) Island growth: $\phi > 0,\ \gamma_S < \gamma_F + \gamma_{S/F}.$ (12b)

The third mode is the so-called Stranski-Krastanov, or layer plus island mode. This is an intermediate case, where the film starts to grow as a layer trying to adjust its lattice to the substrate lattice. However, the thus generated elastic strain cannot be sustained into the bulk of the film and the growth mode switches to island growth after the completion of one or several layers. This change occurs as soon as the elastic strain forces exceed the adhesion forces within the deposit [65].

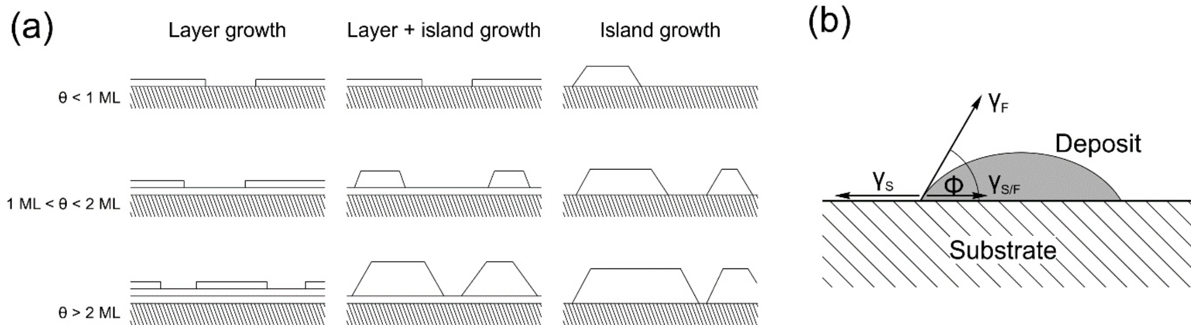

Figure 10: (a) Schematic representation of the three modes of film growth (θ is the coverage, ML stands for monolayer) (redrawn after [66]). (b) Schematic of a nucleus deposited onto a substrate. γ_S, γ_F and $\gamma_{S/F}$ are the surface free energies between substrate and vacuum, deposit and vacuum and substrate and deposit, respectively. Φ is the contact angle between the deposit and the substrate (after [65]).

4.2 Structure zone model

The growth and nucleation of coatings is strongly influenced by the process parameters during deposition including pressure, temperature, ion energies [67] etc. In order to qualitatively show the developing structure as a function of these parameters, several structure zone models (SZMs) were proposed. The first SZM was developed by Movchan and Demchishin for thick coatings deposited by electron beam evaporation [68]. They have found that depending on the homologous deposition temperature T_h ($T_h = T_{dep}/T_m$, with T_{dep} being the deposition temperature) three zones with different, characteristic structures are encountered. Later, Thornton developed an SZM for sputter-deposited coatings, where he added an additional axis representing the deposition pressure and introduced another zone between zone 1 and zone 2, called the transition zone [69]. Messier et al. exchanged the pressure in the SZM by the floating potential, which is more appropriate for sputtered coatings [70]. A more generalized SZM which was suggested by Anders [71] is displayed in Fig.11. This SZM is based on Thornton's with the extension to energetic deposition methods like cathodic arc evaporation and high power impulse magnetron sputtering. In this model the axes are the

generalized temperature T^*, being the substrate temperature plus the potential energy of the arriving species, the generalized kinetic energy E^* of the arriving ions including the mass ratio of ions and film atoms and the coating thickness t^*. In contrast to the other SZMs, this model is also capable of showing thickness reductions due to densification and sputtering of the film [71].

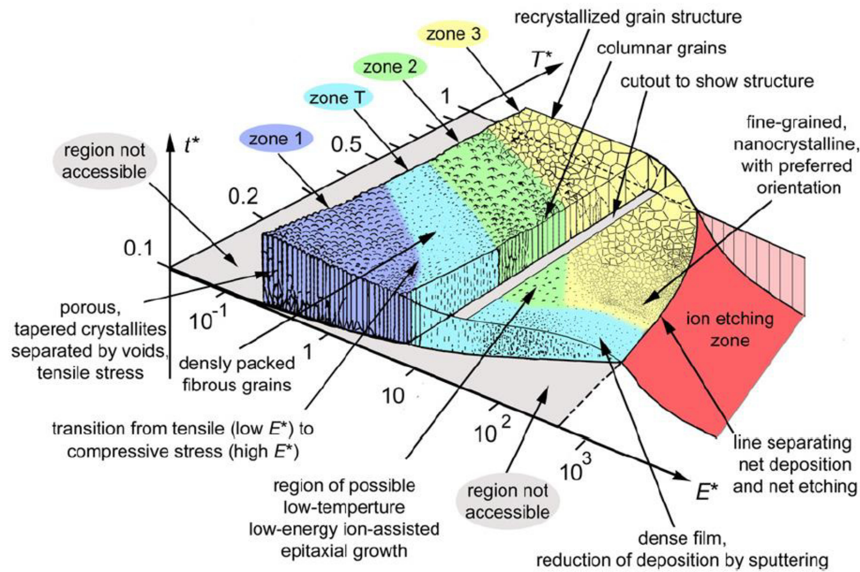

Figure 11: Structure zone model for PVD-processes proposed by Anders [71].

In Anders' SZM the same four zones as in Thornton's can be identified. At low temperature and ion energy zone 1 prevails. Due to the low energy the adatoms are practically immobile and a porous columnar structure with a pronounced surface roughness evolves [40]. Typical for zone 1 is the dependence of film growth on the deposition geometry [69]. When temperature and/or the ion energy is increased, the resulting coating evolves towards a denser structure (zone T). In this zone the adatom diffusion becomes large enough, so that the surface roughness of the substrate can be overcome in the initial growth stage. Thus, the surface is smooth [72]. The grains are smaller than in zone 1 and the microstructure appears to be fibrous without greatly voided grain boundaries [52]. Upon further increase of the temperature at some point surface diffusion begins to be the dominant factor and the coating "*loses all memory of earlier steps in its growth*" [72]. Therefore, considerations such as the deposition geometry become unimportant. In zone 2 the growth process is mostly dominated by the adatom diffusion, which leads to the development of faceted surfaces of the single columnar grains, separated by dense boundaries. The boundary condition for zone 3 type structure is a temperature of around 0.45 - 0.5 T_h [68]. There bulk diffusion gains a dominant influence leading to recrystallization with the development of equiaxed grains [52]. The model

by Anders also shows regions of high intensity ion bombardment conditions, where severe re-sputtering of the coatings and etching occur. These regions are, however, not important for MSD.

4.3 Residual stresses in thin films

Sputtered coatings are generally in a state of residual stress [52,73]. The residual stresses range from tensile, as typical for sputtered metallic coatings deposited at a high pressure [40], to very high compressive stresses in the range of several GPa for hard coatings deposited at high bias potentials [73,74]. The residual stresses in thin films strongly depend on several process parameters [75] including but not limited to temperature [75,76], bias potential [74,77], tilt angle of the substrate relative to the deposition flux [78], gas pressure [40] and target power [77,79,80]. Furthermore, the residual stresses are not constant over the coating thickness [81]. Especially in the early growth stages the induced stresses vary and close to the interface a different stress state than in the bulk of the coating is observed. The stresses in the early growth stage strongly depend on the nucleation conditions [82] and adatom mobility [83]. High stresses can cause coating failure by cracking or delamination in the case of excessive tensile stresses and buckling at very high compressive stresses [84]. On the other hand, stresses can also be beneficial and it was found that compressive stresses improve the hardness of coatings [85].

The residual stresses in coatings are generally comprised of three contributions [73,86]:

$$\sigma_{tot} = \sigma_{ext} + \sigma_{int} + \sigma_{th}, \tag{13a}$$

where σ_{tot}, σ_{ext}, σ_{int} and σ_{th} are the total, the extrinsic, the intrinsic and the thermal stresses, respectively. The extrinsic stresses are due to structural misfits, phase transformations, precipitations, chemical reactions, etc. Often these stresses are a priori assumed to be negligible or to be relaxed by misfit dislocation networks [73] and therefore, only σ_{int} and σ_{th} remain. Thus equation 13a becomes

$$\sigma_{tot} = \sigma_{int} + \sigma_{th}. \tag{13b}$$

σ_{th} is a result of the different thermal expansion coefficients of substrate α_s and coating α_c and is induced by the cooling after deposition. σ_{th} can be calculated by [87]

$$\sigma_{th} = \frac{E_c}{1-\nu_c}(\alpha_s - \alpha_c)(T - T_{dep}). \tag{14}$$

Here, E_c and ν_c are the elastic modulus and Poisson´s ration of the coating, respectively, and T is the temperature. σ_{int} is generated during the growth of the coatings and is comprised of the stress resulting from a volume shrinkage during grain growth, adatom diffusion to the grain boundaries and the stress related to the ion irradiation of the growing film [86].

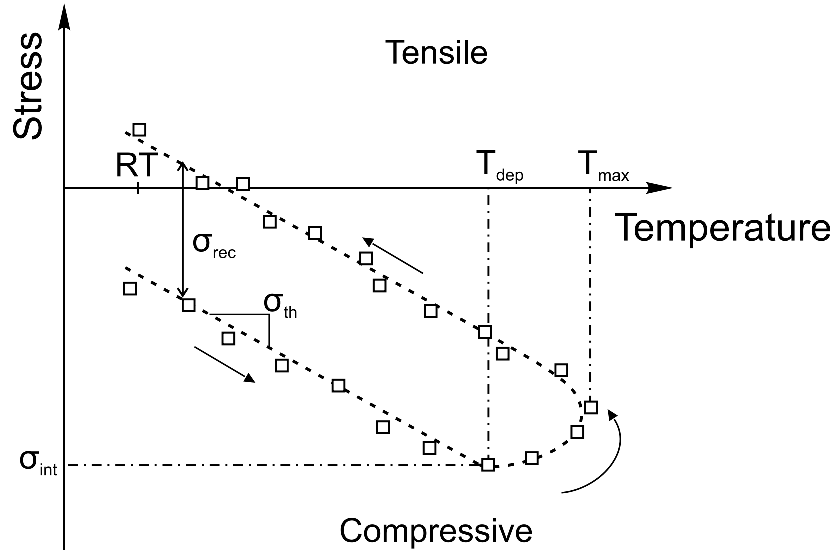

Figure 12: Residual stress as a function of the annealing temperature. RT stands for room temperature and T_{max} is the maximum annealing temperature (modified after [87,89]).

Due to the growth conditions, PVD coatings are in general not thermally stable but tend to recover at high temperatures [88,89]. This can be seen when the stress is measured during thermal cycling to high temperatures, known as biaxial stress-temperature measurement (BSTM). Figure 12 shows a typical stress-temperature curve obtained by BSTM. Upon heating from room temperature (RT) the thermal stresses which are induced during the cooling after the deposition are successively removed. The slope of the curve depends on the thermal expansion coefficients: If α_c is greater than α_s then tensile stresses are induced during cooling and the slope in Fig.12 is negative, and vice versa. At T_{dep} all induced thermal stresses are removed and only the intrinsic stresses remain. When T_{dep} is exceeded, the defects generated during the deposition start to be annealed out which results in a compressive stress relaxation. When the maximum temperature T_{max} of the measurement is reached, the sample is cooled down and the thermal stresses are induced again. Provided that no phase transformation, recrystallization or decomposition has occurred, α_c is not changed and the slopes are the same for heating and cooling. There are two important types of information that can be obtained from BSTM measurements [90]. Firstly, the onset temperature of recovery T_{rec}, which is an indicator for the thermal stability of the coating. Secondly, the amount of stress relaxation due to recovery σ_{rec}, which is related to the hardness loss of the coating due to the

annealing treatment. The recovery includes effects such as the annihilation of point defects, migration of dislocations and the growth and coalescence of subgrains [89].

4.4 Residual stress measurements of thin films

Apart from the above mentioned classification of stresses, residual stresses can also be divided with respect to the dimension into first, second and third order stresses [91,92], see Fig.13. First order stresses, or macrostresses, are the volume average of the stress over all crystallites in the investigated volume. They have a field of action in the range of millimeters and are macroscopically observable. Second and third order stresses are called microscopic stresses and are the deviation from the first order stresses averaged over one crystallite (second order) and stresses on the atomic scale (third order) [91]. Several techniques are available for the determination of residual stresses including mechanic, acoustic, optic, radiographic, magnetic and electric methods [92]. All of these but the radiographic methods using electrons and X-rays are able to assess only the macroscopic stresses. The two most commonly used techniques for the determination of residual stresses in coatings are the wafer curvature method [81] and X-ray techniques [93,94].

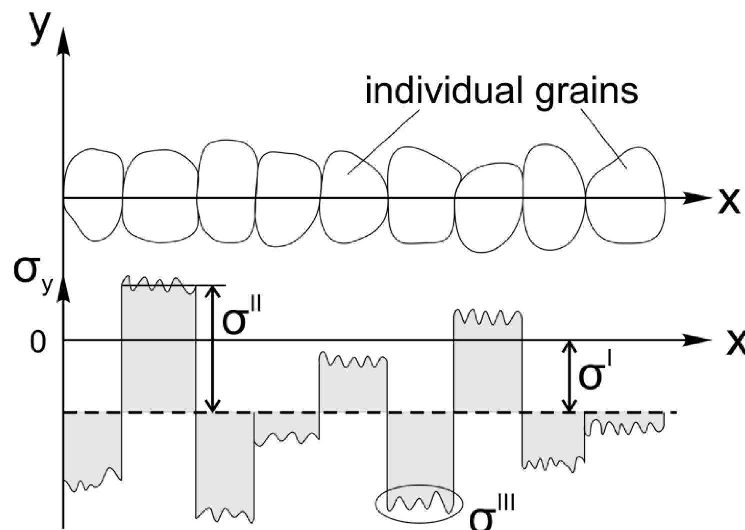

Figure 13: Stress (σ_y) distribution in a coating over several grains. σ^I, σ^{II} and σ^{III} are the first, second and third order stresses, respectively (redrawn and modified after [91]).

4.4.1 Wafer curvature measurements

When a film is deposited onto a flexible substrate, a bending of the film-substrate composite will be induced by to the residual stresses present in the film [41], as presented in Fig.14a. Depending on the nature of the stresses, i.e. tensile or compressive, the bending will be either concave or convex. Stoney was the first to use this bending in 1909 to calculate the

present stresses [95,96]. He has developed the following equation, which is also known as "*Stoney-formula*". In its modified form it reads [97]

$$\sigma_c t_c = M_S \frac{d^2}{6R}, \tag{15}$$

where σ_c is the coating stress, t_c is the coating thickness, M_S is the biaxial modulus of the substrate, d is the substrate thickness and R is the bending radius of the composite. Two requirements need to be fulfilled in order to correctly determine the stress. (a) The coating thickness must be small compared to the substrate but still large enough so that a bending is induced. And (b) the coating must be in the state of plane stress, that is the stress in-plane is independent of the direction. Thus, the stress tensor becomes [96]

$$\bar{\bar{\sigma}} = \begin{pmatrix} \sigma_c & 0 & 0 \\ 0 & \sigma_c & 0 \\ 0 & 0 & 0 \end{pmatrix}. \tag{16}$$

Most commonly single crystalline silicon wafers are used as elastic substrates for this technique, which hence explains the term "*wafer curvature technique*" [81].

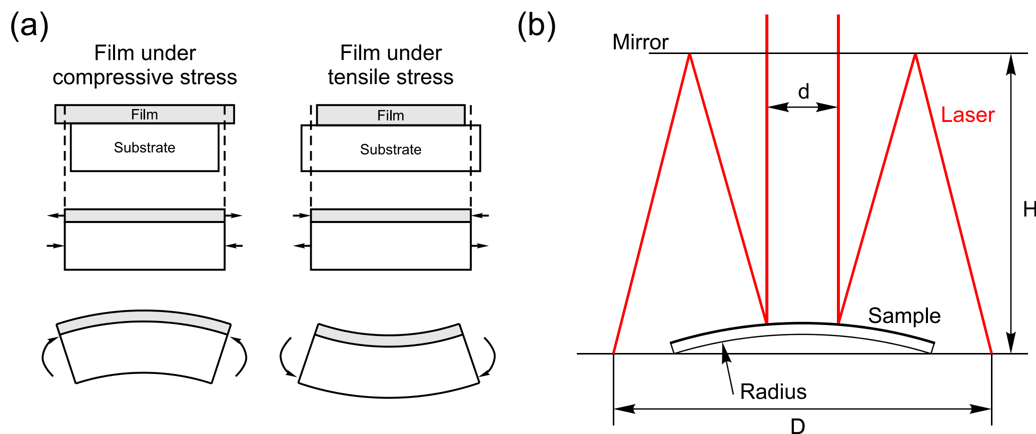

Figure 14: (a) Bending of a film-substrate composite due to compressive and tensile residual stresses (redrawn after [41]). (b) Typical experimental setup for the determination of the bending radius used for wafer curvature measurements employing two parallel laser beams (not in scale).

In order to be able to calculate the stress, one has to determine the bending radius of the composite. Quite commonly the bending radius is measured using laser beams [81]. In the case of a sample that is clamped on one side, one laser beam is sufficient, but also multi-arrays of beams are possible which enable the determination of the spatial distribution of the residual stresses [81]. Figure 14b shows the situation for two parallel laser beams. In this case, the sample is positioned on a plane where the initially parallel laser beams, having a distance

d are reflected towards a mirror placed at the distance H. After being reflected again at the mirror, the distance D can be measured and the bending radius R can be calculated using:

$$R = \frac{2\,H \cdot d}{D - d}. \quad (17)$$

The wafer curvature technique is simple in principle. Therefore, it is quite effortlessly possible to conduct BSTMs as the one presented in Fig.12, for instance when the sample is placed in a vacuum chamber on a heating device [88]. By heating the substrate, also the coefficient of thermal expansion can be determined from the slope of the linear region in Fig.12. This is done by rearranging equation 14, however, knowledge of the mechanical and thermal properties of the substrate is required [98]. Abadias and co-workers frequently use this technique to determine the stress during film growth in situ by a multiple array of laser beams focused on the substrate, where they are reflected and recorded with a CCD camera [82,83,99,100]. Wafer curvature can be quite sensitive and the stresses in even nm-thin coatings can be assessed. Despite all its merits, some critical points need to be mentioned. Firstly, it is only possible to assess the average stress over the coating thickness when measured ex-situ. Secondly, the beams are never perfectly parallel and the alignment might change over time [81]. A third point that needs consideration is the potential plastic deformation of the substrate during film growth and/or annealing [101]. This deformation might alter the measured values considerably and make a reliable measurement impossible.

4.4.2 sin²ψ method

Apart from the mechanical methods, there are several stress measurement techniques involving X-ray diffraction (XRD) [93]. These are based on the determination of the strain as the change of the lattice parameter due to the present residual stresses:

$$\varepsilon^{hkl} = (d^{hkl} - d_0^{hkl})/d_0^{hkl}, \quad (18)$$

where ε^{hkl} is the strain of the lattice planes with Laue indices h, k and l resulting from the residual stress, and d^{hkl} and d_0^{hkl} are the actual and unstrained lattice parameters of the same planes. One of the most common XRD-techniques is the so-called sin²ψ method, with the basic principle shown in Fig.15a [91]. The figure displays a coating with several differently oriented grains under compressive stress. The drawn planes all have the same hkl-indices. It can be seen, that the lattice parameter changes with the orientation to the applied stress. When the planes are normal to the stress, i.e. ψ = 90°, the planes are compressed and the lattice

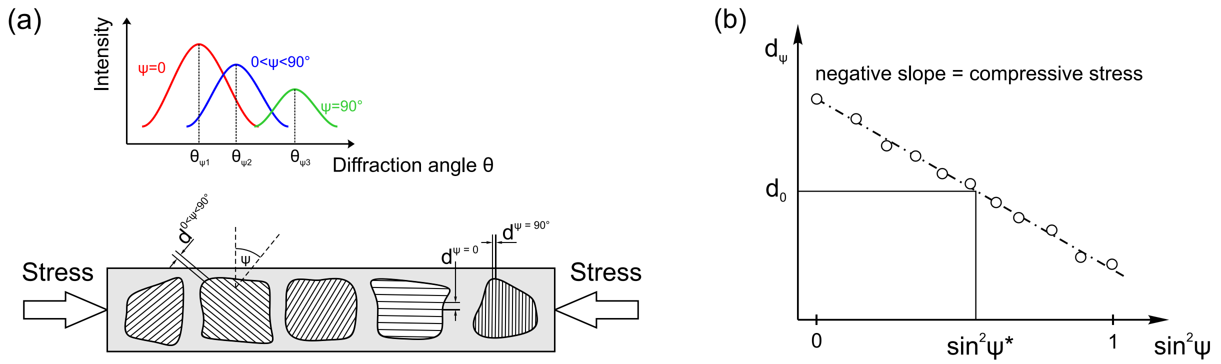

Figure 15: (a) Measurement principle of the sin²ψ method for a coating under compressive stress. (b) Exemplary result for the situation displayed in (a) (after [91]).

parameter is smaller compared to the unstrained lattice. On the other hand, if the planes are parallel to the stress, i.e. $\psi = 0$, they are widened due to lateral contraction. In between those two extrema exists an angle ψ^*, where the lattice parameter is unstrained (d_0^{hkl}). By rotating the sample around ψ and measuring the position of the peak for the lattice planes with the indices h, k and l in the diffractogram θ_ψ^{hkl}, one can determine the lattice parameters at different ψ-angles using Bragg's law

$$\lambda = 2d_\psi^{hkl} sin(\theta_\psi^{hkl}), \quad (19)$$

where λ is the wavelength of the used X-ray beam. For a biaxial stress as in equation 16 the relationship between the strain ε_ψ, ψ and the stress σ_c is [91]

$$\varepsilon_\psi = \frac{d_\psi^{hkl} - d_0^{hkl}}{d_0^{hkl}} = \frac{1+\nu_c}{E_c}\sigma_c \, sin^2\psi - \frac{\nu_c}{E_c}\sigma_c. \quad (20)$$

Equation 20 suggests that there is a linear relationship between d_ψ^{hkl} and $sin^2\psi$. Figure 15b displays an illustrative result for the situation in (a). In order to calculate σ_c, d_0^{hkl} needs to be determined since this value is often not known a-priori. d_0^{hkl} is measured at ψ^*, where the strain equals zero, which can be calculated from equation 20 to be [91]

$$\sin\psi^* = \sqrt{\frac{2\nu_c}{1+\nu_c}}. \quad (21)$$

This relationship only holds for an isotropic coating material [91]. Coatings, however, frequently have a texture and determining d_0^{hkl} precisely is thus often a difficult task.

5 Investigated coating materials

5.1 Titanium nitride

The titanium-nitrogen system with corresponding films deposited by both, physical [102] and chemical vapor deposition (CVD) methods [103,104], is one of the most-investigated coating systems since approximately the beginning of the seventies of the last century. Particularly stoichiometric titanium nitride (TiN) is of special interest since it has several outstanding properties which makes it useful for a number of applications. For instance, it has a high melting temperature of more than 3 000 K, depending on the exact composition [105] and coatings made thereof are known to have high hardness values [106]. At the same time it has a good thermal conductivity of about 25 W/mK [107] which makes it ideal for the use as protective coatings for cutting tools. Additionally, TiN is biocompatible and TiN-based coatings are frequently used for bio-implants [108,109]. Further applications include the use as diffusion barriers in the microelectronics industry [110–112] and as decorative coatings [113,114]. The latter is owing to the golden appearance of TiN which makes it suitable as an abrasive resistant alternative for gold [114]. Also, for the investigation of basic principles of magnetron sputtering TiN has served as a model coating system and many works exist on the reactive sputtering of titanium in nitrogen containing atmosphere [62,106,115–117].

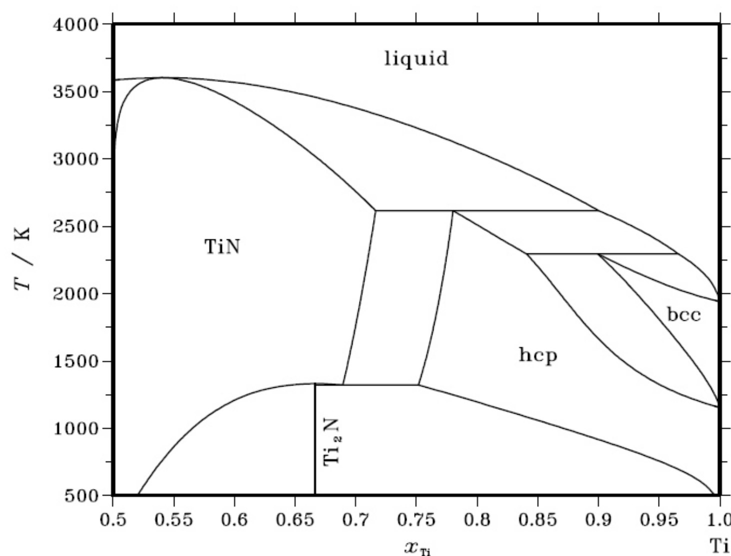

Figure 16: Binary phase diagram of titanium and nitrogen [105].

Figure 16 shows the binary phase diagram of titanium and nitrogen up to a composition of 50 at.-% nitrogen. As can be seen, there are three stable phases extending to room temperature. The hexagonal closed packed (hcp) titanium phase, and the two compound

phases Ti_2N and TiN. Ti_2N crystallizes in tetragonal structure and has only a very small field of existence, while TiN has a face centered cubic (fcc) NaCl-structure and spans over a comparatively large range of compositions [105]. The resulting coating properties strongly depend on which of these phases are present after deposition and several different phase combinations were reported. Basically, however, two cases are of interest [102]:

- ***Single-phase TiN***

  As already mentioned above, the TiN phase has the NaCl-structure and it has a lattice parameter of 4.24 Å [102]. The fcc structure is stable over a comparatively large compositional range. When the coatings are slightly under or over-stoichiometric, the lattice parameter and the coating density decrease in both cases due to the generation of voids, which leads to a hardness decrease for non-stoichiometric TiN. The color of the coating is also strongly dependent on the exact composition and changes from light yellow to golden yellow to brown with increasing nitrogen content from under to over-stoichiometric compositions [118,119]. This color can be used as an indication for the hardness [118]. The grain size is generally below 100 nm if the films are deposited below 600 °C (0.27 T_h) and the typically evolving microstructure is a fibrous zone T structure [102]. The electrical resistivity is comparable to metals. For stoichiometric TiN it is approximately 25 µΩcm, which is even lower than the value for pure titanium [102].

- ***Films containing the Ti_2N-phase***

  When the composition is under-stoichiometric a fine-grained two phase structure containing Ti_2N evolves. At nitrogen contents below 25 at.-% the coating consists of hcp titanium grains with a size in the range of 250 nm, surrounded by highly deformed Ti_2N. At higher nitrogen contents the structure is depending on whether the nitrogen content is below or above 35 at.-%. In this region the grains are subdivided into alternating lamellae either consisting of hcp titanium/Ti_2N or Ti_2N/TiN. These lamellae have widths in the range of 100-200 Å. Although an increased hardness would be expected for the small lamellae compared to single phase TiN due to the Hall-Petch effect [90], this is not observed for these coatings. The reason might be the strong orientation relationship between the lamellae, which does not provide a considerable obstacle for the movement of dislocations [102]. The electrical resistivity, however, is strongly increased due to the two-phase structure, and shows a maximum at a nitrogen content around 25 - 35 % [102].

Although TiN has several useful properties that make it suitable as wear protective hard coating it suffers from some disadvantages limiting its usability. One drawback is the rather low oxidation resistance. TiN can only be used up to temperatures around 550 °C before it starts to oxidize [120]. Also, the high temperature hardness is somewhat limited for TiN. This led to the invention of second and third generation coating systems based on TiN, such as titanium aluminum nitride (TiAlN) and titanium carbon nitride (TiCN), for instance. These coating materials exhibit a superior performance like increased tool lifetime and decreased wear [121]. As a more specific example, TiAlN shows an age hardening effect due to coherency strains resulting from the spinodal decomposition to TiN and cubic AlN at temperatures above 600 °C [122]. Furthermore, it exhibits an improved resistance against high-temperature oxidation due to the formation of a protective oxide scale at elevated temperatures [120,123].

5.2 Amorphous carbon

Depending on the hybridization of the electron orbitals, solid carbon exists in numerous different forms [124], the most recognized of which are probably the two crystalline forms graphite and diamond. Graphite is sp^2-hybridized carbon consisting of several layers of hexagonal planes which have strong σ-bonds in plane, but only weak π-bonds normal to the planes. Therefore, graphite is anisotropic with different electrical and mechanical properties in and out of plane [125]. Due to the weak π-bonds, the planes can glide easily and carbon is (among several other applications) frequently used as solid state lubricant [126]. On the other hand, diamond is an exceptionally hard material which has the highest heat conductivity of all materials and wide band gap of 5.5 eV [127]. This is owing to the tetragonal, covalent bonding structure resulting from sp^3-hybridized orbitals. Due to its exceptional properties, diamond is used as tool material for stone cutting [128] or heat sinks in electronic devices [129], for instance.

Amorphous carbon (a-C) is a class of thin film materials that spans a wide range of different coatings with diverse properties [130]. The versatility is mainly owing to the fact that the structure and physical properties of carbon strongly depend on the hybridization, as discussed above. Therefore, the amount of each bonding type in carbon coatings grown from the vapor phase greatly influences their properties [127,130]. In order to qualitatively assess the microstructure of a-C coatings, Jacob and Möller [131] and, based on this work, Ferrari and Robertson [132] have developed a ternary phase diagram which is displayed in Fig.17. The diagram shows the different types of a-C as a function of the amount of sp^2 and sp^3-hybridized

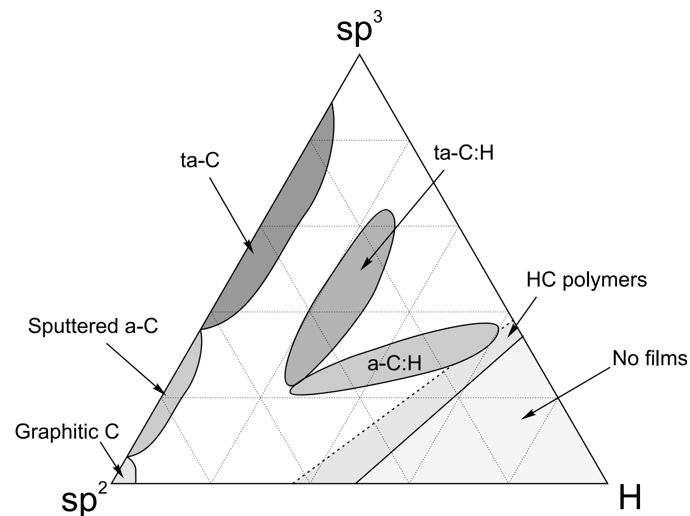

Figure 17: Ternary phase diagram redrawn after Ferrari and Robertson [132] of amorphous carbon coatings. The three corners correspond to graphite (sp^2), diamond (sp^3) and hydrogen (H).

carbon, as well as the hydrogen content. Purely sp^2-bonded carbon (situated in the lower left-hand corner of the diagram) refers to a material with graphite-like properties, i.e. low hardness and high electrical conductivity, as well as a low density. Coatings in this region, grown for instance by thermal evaporation, are known as graphitic carbon coatings or glassy carbon [127]. When the a-C coatings are deposited by MSD, some sp^3 bonds are introduced by the ion bombardment. In order to reach higher values of sp^3 a pronounced ion bombardment is necessary, as for instance present during cathodic arc evaporation. These coatings are known as tetrahedral amorphous carbon (ta-C) and show a more “diamond-like” character [127]. Hence, carbon coatings containing a significant amount of sp^3 bonding are known as diamond-like carbon, or DLC [132].

Frequently, hydrogen is added to the carbon coatings in order to modify the properties [133,134]. Hydrogen reduces the friction coefficient by saturating the dangling bonds of the carbon [134]. Both, coatings with a high (ta-C:H) and low (a-C:H) sp^3 content are encountered. Such films are produced by a variety of methods [135] including plasma enhanced CVD [134] and sputtering in a hydrocarbon gas containing reactive atmosphere [136]. All DLCs (with or without hydrogen) are metastable and tend to transform to graphitic carbon upon heating or irradiation [137]. The formation of polyethylene and polyacetylene defines the limit between a-C and hydrocarbon polymer coatings at high hydrogen contents [127]. Due to the wide range of achievable properties there are many applications of DLC today, including as protective and antireflective coatings for infrared windows, coatings in magnetic recording devices, wear protection of bearings, precision gauges in the automotive industry and biomedical applications [138–141].

5.2.1 Raman spectroscopy of amorphous carbon

Because of the strong influence on the properties, assessing the amount of sp^2 and sp^3 bonded carbon is of vital interest. However, determining the sp^3-content quantitatively is not trivial and sophisticated methods such as electron energy loss spectroscopy or nuclear magnetic resonance are needed [127]. In contrast, Raman spectroscopy is a comparatively simple technique that provides the possibility of qualitatively assessing the microstructure and indirectly concluding on the sp^3 content [132,142]. This technique is non-destructive and it is often used for the investigation of a-C coatings. It is based on the inelastic scattering of photons with molecules or phonons and offers the possibility to determine phase compositions, bonding types or internal stresses of materials [143].

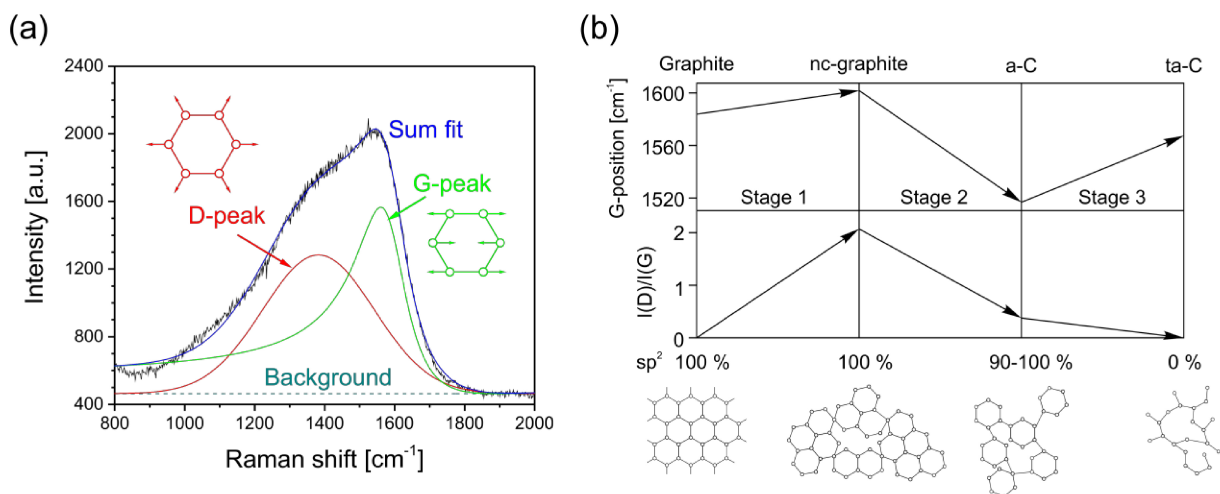

Figure 18: (a) Fit of a Raman spectrum of an a-C coating deposited by magnetron sputtering. The spectrum is fitted using a Gauss function (D-peak) and a Breit-Wigner-Fano function (G-peak) assuming a linear background (own work). The two different vibrational modes are also schematically displayed [132]. (b) Three stage model for the qualitative estimation of the microstructure of a-C proposed by Ferrari and Robertson (modified after [132]).

For the Raman spectroscopic investigation of a-C mainly two observed peaks are of interest. These peaks correspond to the stretching-vibration of carbon-carbon bonds and to the breathing of hexagonal carbon rings and are termed the G and D-modes, respectively [132], see Fig.18a. Figure 18a illustrates the result of a typical Raman measurement for a Raman shift between 800 and 2000 cm^{-1}, where these peaks are located. In order to assess the microstructure, the two peaks are fitted by appropriate mathematical functions. Frequently employed functions are Gauss, Lorentz and Breit-Wigner-Fano (BWF) peak functions, but a priori none of these are preferred over the others [132]. Two parameters are then used to assess the microstructure: The position of the G-mode and the intensity ratio of the D-peak over the G-peak ($I(D)/I(G)$). Ferrari and Robertson [132] developed a

phenomenological three stage model based on these two values, which can be consulted for the estimation of the coating microstructure. The three stages are [132]:

- Stage 1 from single crystalline to nanocrystalline carbon: At the beginning of stage 1 single crystalline graphite is present. The breathing is forbidden for perfect graphite and hence $I(D)/I(G)$ is zero and the G-position is positioned at approximately 1580 cm^{-1}, which is the single graphite Raman mode. The intensity ratio is inversely proportional to the diameter of graphite clusters, which is known as Tuinstra-Koenig relationship [144]. Hence, $I(D)/I(G)$ starts to increase with the introduction of graphitic clusters. The appearance of the D-peak due to the clusters results in a shift of the G-peak to higher values. At the end of stage 1 the cluster size is approximately 20 nm.

- Sage 2 from nanocrystalline to amorphous carbon: Defects are progressively induced in this stage which leads to an amorphization of the coatings. At cluster sizes below 20 nm, $I(D)/I(G)$ is proportional to the square of the cluster size, and hence decreases with ongoing amorphization. Some sp^3 bonds are introduced but the amount of sp^2 is still more than 80 %, although the structure is completely disordered. Sputtered a-C coatings are usually found to be in stage 2.

- Stage 3 from amorphous carbon to tetrahedral amorphous carbon: In this stage sp^3-bonds are introduced up to a content of $\sim$85 % and the rings present are gradually transferred to chains. Therefore, no breathing can occur and $I(D)/I(G)$ is very low, or even zero. The G-position shifts to higher values which is due to the introduction of olefinic carbon-carbon double bonds (C=C) by the change from rings to chains. The olefinic double bonds are shorter than the carbon-carbon single bonds (C-C) and hence have a higher frequency explaining the higher Raman shift.

6 Summary and conclusions

When opposing bulk and surface properties are crucial for a certain application, the deposition of single or multilayer coatings on suitable substrates is inevitable. Due to its flexibility and the possibility to deposit well-homogenous films, magnetron sputtering is one of the most widely used deposition techniques for such high-end coating systems. However, deposition rates are frequently low which results in an only limited efficiency and productivity, thus restricting its applicability in industry. The present work therefore investigates the possibility of overcoming this issue by the in principle simple approach of increasing the power applied to the sputtering target. The influence of the discharge power on the plasma as well as on the process and resulting coating properties was systematically assessed, in order to obtain a comprehensive understanding of the correlation between target power and resulting coatings. It was found that the discharge power has a strong effect on the plasma discharge, the process and the resulting coating properties.

Plasma

Spatially resolved Langmuir probe measurements were conducted to assess the influence of the discharge power on the plasma properties during the direct current magnetron sputtering of titanium in an argon discharge. For this purpose the target power was varied over one order of magnitude during the measurements. Increasing the target power resulted in a higher plasma density, electron energy and shielding of the plasma, which was attributed to the higher discharge current. It was also found, that there is a minimum power necessary to obtain a stable discharge. At low power values, the electron distribution as well as floating potential were non-linearly changing, while at high powers the discharge appeared to be homogenous. Irrespective of the applied power, however, the discharge can be divided into three distinct zones with characteristic electron distributions (see publication I).

Process

Two different sputter deposition processes were investigated: the reactive sputtering of TiN_x ($x \leq 1$) coatings deposited at 200 °C and the non-reactive sputter deposition of amorphous carbon in argon and neon at initially room temperature, i.e. without external heating. Due to the increased amount of sputtered material at elevated discharge power, the poisoning of the titanium target is shifted to higher reactive nitrogen gas flow values, which enables the opportunity to increase the amount of the incorporated nitrogen in the coatings. Thus, stoichiometric coatings can be deposited at a high deposition rate when the power is raised

sufficiently. When no external heating is applied, raising the target power leads to a more pronounced temperature load of the substrate. This in turn results in a lower amount of incorporated inert gas atoms due to the more pronounced desorption of adsorbed gas atoms. In all cases, however, a proportional increase of the deposition rate can be observed with discharge power (see publications II and III).

Coating

Coatings of the two model systems were subsequently deposited and investigated with respect to their properties. From the presented results it can be concluded that generalizing the influence of the discharge power on different coating systems with different deposition parameters is difficult. In the case of TiN deposited at a constant temperature, an increase of the discharge power has a beneficial influence on the hardness due to the introduction of residual stresses and grain refinement resulting from the higher deposition rate. The stress of the amorphous carbon coatings on the other hand, is not altered by an increased deposition power. However, the increased deposition temperature leads to the growth of the present graphitic clusters which results in a hardness drop, irrespective of whether argon or neon is used as process gas, or whether a bias is applied or not (see publications II and III). The residual stress state, being influenced by the deposition power, was found to be a crucial parameter in determining the properties of the deposited coatings. In addition to the above mentioned studies, the limitation of the widely applied wafer curvature method for residual stress measurement was investigated (see publication IV).

7 References

[1] R.F. Bunshah (Ed.), Deposition Technologies for Films and Coatings, Noyes Publications (1982) Park Ridge, USA.

[2] D.M. Mattox, Handbook of Physical Vapor Deposition (PVD) Processing: Film Formation, Adhesion, Surface Preparation and Contamination Control, Noyes Publications (1998) Westwood, USA.

[3] J. Musil, J. Vac. Sci. Technol. A 14 (1996) 2187.

[4] M. Jílek, F. Mendez Martin, P.H. Mayrhofer, S. Veprek, Thin Solid Films 556 (2014) 361–368.

[5] W. Posadowski, Thin Solid Films 392 (2001) 201–207.

[6] W.M. Posadowski, Vacuum 46 (1995) 1017–1020.

[7] F. Engelmark, J. Westlinder, T. Nyberg, S. Berg, J. Vac. Sci. Technol. A 21 (2003) 1981.

[8] H. Ohsaki, Y. Tachibana, A. Hayashi, A. Mitsui, Y. Hayashi, Thin Solid Films 351 (1999) 57–60.

[9] T. Nyberg, S. Berg, U. Helmersson, K. Hartig, Appl. Phys. Lett. 86 (2005) 164106.

[10] W.D. Sproul, D.J. Christie, D.C. Carter, Thin Solid Films 491 (2005) 1–17.

[11] U. Stroth, Plasmaphysik: Phänomene, Grundlagen, Anwendungen, Vieweg und Teubner (2011) Wiesbaden, Germany.

[12] B.N. Chapman, Glow Discharge Processes: Sputtering and Plasma Etching, John Wiley and Sons (1980) New York, USA.

[13] A. Fridman, Plasma Chemistry, Cambridge University Press (2008) Cambridge, UK.

[14] M.A. Lieberman, A.J. Lichtenberg, Principles of Plasma Discharges and Materials Processing, 2nd ed., Wiley-Interscience (2005) Hoboken, USA.

[15] M. Schmidt, H. Conrads, in: R. Hippler, et al. (Eds.), Low Temperature Plasmas: Fundamentals, Technologies and Techniques, 2nd ed., Wiley-VCH (2008) Weinheim, Germany, pp. 363–383.

[16] M. Laroussi, et al. (Eds.), Plasma Medicine: Applications of Low-Temperature Gas Plasmas in Medicine and Biology, Cambridge University Press (2012) Cambridge, UK.

[17] M.G. Kong, G. Kroesen, G. Morfill, T. Nosenko, T. Shimizu, J. van Dijk, J.L. Zimmermann, New J. Phys. 11 (2009) 115012.

[18] A. Piel, Plasma Physics: An Introduction to Laboratory, Space, and Fusion Plasmas, Springer (2010) Heidelberg, Germany.

[19] W.M. Stacey, Fusion Plasma Physics, Wiley-VCH (2005) Weinheim, Germany.

[20] A. Rutscher, in: R. Hippler, et al. (Eds.), Low Temperature Plasmas: Fundamentals, Technologies and Techniques, 2nd ed., Wiley-VCH (2008) Weinheim, Germany.
[21] V.A. Godyak, B.M. Alexandrovich, J. Appl. Phys. 118 (2015) 233302.
[22] V.M. Donnelly, J. Phys. D: Appl. Phys. 37 (2004) R217-R236.
[23] V.A. Godyak, V.I. Demidov, J. Phys. D: Appl. Phys. 44 (2011) 269501.
[24] A.A. Fridman, L.A. Kennedy, Plasma Physics and Engineering, 2nd ed., CRC Press (2011) Boca Raton, USA.
[25] Y. Itikawa, Molecular Processes in Plasmas: Collisions of Charged Particles with Molecules, Springer (2007) Berlin, Germany.
[26] Pfau S, Tichý M, in: R. Hippler, et al. (Eds.), Low Temperature Plasmas: Fundamentals, Technologies and Techniques, 2nd ed., Wiley-VCH (2008) Weinheim, Germany, pp. 175–213.
[27] I. Langmuir, H. Mott-Smith, Gen. Elec. Rev. 27 (1924) 449.
[28] B.E. Cherrington, Plasma Chem. Plasma Process. 2 (1982) 113–140.
[29] R.M. Clements, J. Vac. Sci. Technol. 15 (1978) 193.
[30] V.A. Godyak, in: O. Auciello, et al. (Eds.), Plasma-Surface Interactions and Processing of Materials, Springer Netherlands (1990) Dordrecht, Netherlands, pp. 95–134.
[31] R.L. Merlino, Am. J. Phys. 75 (2007) 1078.
[32] V. Godyak, B. Alexandrovich, Plasma Sources Sci. Technol. 24 (2015) 52001.
[33] S.-H. Seo, J.-H. In, H.-Y. Chang, Plasma Sources Sci. Technol. 13 (2004) 409.
[34] M.J. Druyvesteyn, Z. Physik 64 (1930) 781.
[35] V. A. Godyak, R. B. Piejak, B. M. Alexandrovich, J. Appl. Phys. 73 (1993) 3657.
[36] F. Magnus, J.T. Gudmundsson, Rev. Sci. Instrum. 79 (2008) 73503.
[37] A. Savitzky, M.J.E. Golay, Anal. Chem. 36 (1964) 1627–1639.
[38] P. Kelly, R. Arnell, Vacuum 56 (2000) 159–172.
[39] K. Ellmer, in: R. Hippler, et al. (Eds.), Low Temperature Plasmas: Fundamentals, Technologies and Techniques, 2nd ed., Wiley-VCH (2008) Weinheim, Germany, pp. 675–714.
[40] W.D. Westwood, Sputter Deposition, AVS (2003) New York, USA.
[41] M. Ohring, The Materials Science of Thin Films, Academic Press (1991) San Diego, USA.
[42] P. Sigmund, Phys. Rev. 184 (1969) 383–416.
[43] R.K. Waits, J. Vac. Sci. Technol. 15 (1978) 179.
[44] J.A. Thornton, J. Vac. Sci. Technol. 15 (1978) 188.
[45] S.M. Rossnagel, H.R. Kaufman, J. Vac. Sci. Technol. A 5 (1987) 2276.
[46] R. Arnell, P. Kelly, Surf. Coat. Technol. 112 (1999) 170–176.

[47] B. Window, N. Savvides, J. Vac. Sci. Technol. A 4 (1986) 196.
[48] B. Window, Surf. Coat. Technol. 81 (1996) 92–98.
[49] J.A. Thornton, J. Vac. Sci. Technol. 15 (1978) 171–177.
[50] M. Wright, T. Beardow, J. Vac. Sci. Technol. A 4 (1986) 388–392.
[51] P.J. Hockley, High target utilisation sputtering system with remote plasma source, UK Patent Application No. GB 2360530 A (2001).
[52] J.A. Thornton, in: R.F. Bunshah (Ed.), Deposition Technologies for Films and Coatings, Noyes Publications (1982) Park Ridge, USA, pp. 170–243.
[53] D. Depla, Magnetrons, Reactive Gases and Sputtering, 3rd ed., Diederick Depla (2014) Ghent.
[54] I. Safi, Surf. Coat. Technol. 127 (2000) 203–218.
[55] J. Musil, P. Baroch, J. Vlček, K.H. Nam, J.G. Han, Thin Solid Films 475 (2005) 208–218.
[56] D. Depla, R. de Gryse, Surf. Coat. Technol. 183 (2004) 184–189.
[57] D. Depla, R. de Gryse, Surf. Coat. Technol. 183 (2004) 196–203.
[58] D. Depla, R. de Gryse, Surf. Coat. Technol. 183 (2004) 190–195.
[59] E. Särhammar, K. Strijckmans, T. Nyberg, S. van Steenberge, S. Berg, D. Depla, Surf. Coat. Technol. 232 (2013) 357–361.
[60] S. Berg, H.-O. Blom, T. Larsson, C. Nender, J. Vac. Sci. Technol. A 5 (1987) 202.
[61] W.D. Sproul, Vacuum 51 (1998) 641–646.
[62] S. Schiller, G. Beister, W. Sieber, Thin Solid Films 111 (1984) 259–268.
[63] D. Depla, J. Haemers, R. de Gryse, Surf. Coat. Technol. 235 (2013) 62–67.
[64] I. Petrov, P.B. Barna, L. Hultman, J.E. Greene, J. Vac. Sci. Technol. A 21 (2003) S117.
[65] H. Lüth, Solid Surfaces, Interfaces and Thin Films, 4th ed., Springer (2001) Berlin, Germany.
[66] J.A. Venables, G.D.T. Spiller, M. Hanbucken, Rep. Prog. Phys. 47 (1984) 399–459.
[67] I. Petrov, F. Adibi, J.E. Greene, L. Hultman, J.-E. Sundgren, Appl. Phys. Lett. 63 (1993) 36.
[68] B.A. Movchan, A.V. Demchishin, Fiz. Metal. Metalloved. 28 (1969) 83–90.
[69] J.A. Thornton, J. Vac. Sci. Technol. 11 (1974) 666–670.
[70] R. Messier, A.P. Giri, R.A. Roy, J. Vac. Sci. Technol. A 2 (1984) 500–503.
[71] A. Anders, Thin Solid Films 518 (2010) 4087–4090.
[72] J.A. Thornton, J. Vac. Sci. Technol. A 4 (1986) 3059–3065.
[73] H. Oettel, R. Wiedemann, Surf. Coat. Technol. 76-77 (1995) 265–273.
[74] Y. Pauleau, Vacuum 61 (2001) 175–181.
[75] O. Knotek, R. Elsing, G. Krämer, F. Jungblut, Surf. Coat. Technol. 46 (1991) 265–274.
[76] J.A. Thornton, D.W. Hoffman, Thin Solid Films 171 (1989) 5–31.

[77] A.J. Perry, M. Jagner, P.F. Woerner, W.D. Sproul, P.J. Rudnik, Surf. Coat. Technol. 43-44 (1990) 234–244.

[78] A. Neidhardt, U. Reinhold, E. Schroeter, W. Wuttke, Thin Solid Films 192 (1990) 263–275.

[79] C. Saringer, R. Franz, K. Zorn, C. Mitterer, J. Vac. Sci. Technol. A 34 (2016) 41517.

[80] A.J. Perry, M. Jagner, W.D. Sproul, P.J. Rudnik, Surf. Coat. Technol. 39-40 (1989) 387–395.

[81] G. Janssen, Thin Solid Films 515 (2007) 6654–6664.

[82] A. Fillon, G. Abadias, A. Michel, C. Jaouen, Thin Solid Films 519 (2010) 1655–1661.

[83] G. Abadias, A. Fillon, J.J. Colin, A. Michel, C. Jaouen, Vacuum 100 (2014) 36–40.

[84] V. Teixeira, Vacuum 64 (2002) 393–399.

[85] P.H. Mayrhofer, C. Mitterer, J. Musil, Surf. Coat. Technol. 174-175 (2003) 725–731.

[86] R. Daniel, K.J. Martinschitz, J. Keckes, C. Mitterer, Acta Mater. 58 (2010) 2621–2633.

[87] R. Daniel, D. Holec, M. Bartosik, J. Keckes, C. Mitterer, Acta Mater. 59 (2011) 6631–6645.

[88] C. Mitterer, P. Mayrhofer, J. Musil, Vacuum 71 (2003) 279–284.

[89] L. Hultman, C. Mitterer, in: H. Cavaleiro (Ed.), Nanostructured Coatings, Springer (2006) New York, USA, pp. 464–510.

[90] P.H. Mayrhofer, C. Mitterer, L. Hultman, H. Clemens, Prog. Mater. Sci. 51 (2006) 1032–1114.

[91] M. Birkholz, Thin Film Analysis by X-Ray Scattering, Wiley-VCH (2006) Weinheim, Germany.

[92] K. Nitzsche, Schichtmeßtechnik, Vogel (1997) Würzburg, Germany.

[93] U. Welzel, J. Ligot, P. Lamparter, A.C. Vermeulen, E.J. Mittemeijer, J. Appl. Crystallogr. 38 (2005) 1–29.

[94] I.C. Noyan, T.C. Huang, B.R. York, Crit. Rev. Solid State 20 (1995) 125–177.

[95] G.G. Stoney, Proc. R. Soc. Lond. 82 (1909) 172–175.

[96] G. Janssen, M.M. Abdalla, F. van Keulen, B.R. Pujada, B. van Venrooy, Thin Solid Films 517 (2009) 1858–1867.

[97] W.D. Nix, Metall. Trans. A 20A (1989) 2217–2245.

[98] M. Tkadletz, N. Schalk, R. Daniel, J. Keckes, C. Czettl, C. Mitterer, Surf. Coat. Technol. 285 (2016) 31–46.

[99] G. Abadias, L.E. Koutsokeras, P. Guerin, P. Patsalas, Thin Solid Films 518 (2009) 1532–1537.

[100] I.A. Saladukhin, G. Abadias, A. Michel, S.V. Zlotski, V.V. Uglov, G.N. Tolmachova, S.N. Dub, Thin Solid Films 538 (2013) 32–41.

[101] C. Saringer, M. Tkadletz, C. Mitterer, Surf. Coat. Technol. 274 (2015) 68–75.

[102] J.-E. Sundgren, Thin Solid Films 128 (1985) 21–44.

[103] S.R. Kurtz, R.G. Gordon, Thin Solid Films 140 (1986) 277–290.

[104] K. Sugiyama, J. Electrochem. Soc. 122 (1975) 1545.

[105] P. Franke, D. Neuschütz (Eds.), Binary Systems Part 4 in: SpringerMaterials (online database), Binary Systems from Mn-Mo to Y-Zr · N-Ti (Springer, Heidelberg, 2016) http://materials.springer.com/lb/docs/sm_lbs_978-3-540-32593-2_21, accessed August 2017.

[106] P. Mayrhofer, F. Kunc, J. Musil, C. Mitterer, Thin Solid Films 415 (2002) 151–159.

[107] Pierre Villars (Chief Editor), PAULING FILE in: Inorganic Solid Phases, SpringerMaterials (online database), TiN ht thermal conductivity (Springer, Heidelberg, 2016), http://materials.springer.com/isp/physical-property/docs/ppp_092440, accessed August 2017.

[108] B. Subramanian, C.V. Muraleedharan, R. Ananthakumar, M. Jayachandran, Surf. Coat. Technol. 205 (2011) 5014–5020.

[109] B.F. Coll, P. Jacquot, Surf. Coat. Technol. 36 (1988) 867–878.

[110] M. Mühlbacher, F. Mendez-Martin, B. Sartory, N. Schalk, J. Keckes, J. Lu, L. Hultman, C. Mitterer, Thin Solid Films 574 (2015) 103–109.

[111] S.-Q. Wang, I. Raaijmakers, B.J. Burrow, S. Suthar, S. Redkar, K.-B. Kim, J. Appl. Phys. 68 (1990) 5176.

[112] V. Merie, M. Pustan, G. Negrea, C. Bîrleanu, Appl. Surf. Sci. 358 (2015) 525–532.

[113] B. Zega, M. Kornmann, J. Amiguet, Thin Solid Films 45 (1977) 577–582.

[114] S. Niyomsoan, W. Grant, D. Olson, B. Mishra, Thin Solid Films 415 (2002) 187–194.

[115] S. Mahieu, D. Depla, J. Phys. D: Appl. Phys. 42 (2009) 53002.

[116] L. Combadiere, J. Machet, Surf. Coat. Technol. 82 (1996) 145–157.

[117] S.M. Borah, H. Bailung, A.R. Pal, J. Chutia, J. Phys. D: Appl. Phys. 41 (2008) 195205.

[118] W.D. Sproul, P.J. Rudnik, C.A. Gogol, Thin Solid Films 171 (1989) 171–181.

[119] M. Wittmer, J. Vac. Sci. Technol. A 3 (1985) 1797.

[120] W. Münz, J. Vac. Sci. Technol. A 4 (1986) 2717–2725.

[121] P. Jindal, A. Santhanam, U. Schleinkofer, A. Shuster, Int. J. Refract. Met. H. 17 (1999) 163–170.

[122] P.H. Mayrhofer, A. Hörling, L. Karlsson, J. Sjölén, T. Larsson, C. Mitterer, L. Hultman, Appl. Phys. Lett. 83 (2003) 2049–2051.

[123] S. PalDey, S. Deevi, Mat. Sci. Eng. 342 (2003) 58–79.

[124] B. McEnaney, in: T.D. Burchell (Ed.), Carbon Materials for Advanced Technologies, Pergamon (1999) Amsterdam, Netherlands, pp. 1–34.

[125] D.D.L. Chung, J. Mater. Sci. 37 (2002) 1475–1489.

[126] F.J. Clauss, Solid lubricants and self-lubricating solids, Academic Press (1972) New York, USA.

[127] J. Robertson, Mat. Sci. Eng. R 37 (2002) 129–281.

[128] H.K. Tönshoff, H. Hillmann-Apmann, J. Asche, Diam. Relat. Mater. 11 (2002) 736–741.

[129] J. Custers, F.A. Raal, Novel diamond particle particularly for use in heat sinks, US Patent No US 3,828,848 (1974).

[130] J. Robertson, Adv. Phys. 35 (1986) 317–374.

[131] W. Jacob, W. Möller, Appl. Phys. Lett. 63 (1993) 1771–1773.

[132] A.C. Ferrari, J. Robertson, Phys. Rev. B 61 (2000) 14095–14107.

[133] D.I. Jones, A.D. Stewart, Philos. Mag. B 46 (2006) 423–434.

[134] A. Grill, IBM J. Res. & Dev. 43 (1999) 147–162.

[135] L.-P. Andersson, Thin Solid Films 86 (1981) 193–200.

[136] E.D. Babich, A.C. Callegari, F.E. Doany, S. Purushothaman, Sputter deposition of hydrogenated amorphous carbon film and applications thereof, US Patent No US 5,830,332 (1998).

[137] A. Grill, Diam. Relat. Mater. 8 (1999) 428–434.

[138] Y. Lifshitz, Diam. Relat. Mater. 8 (1999) 1659–1676.

[139] A. Matthews, S.S. Eskildsen, Diam. Relat. Mater. 3 (1994) 902–911.

[140] A.H. Lettington, Carbon 36 (1998) 555–560.

[141] G. Dearnaley, J.H. Arps, Surf. Coat. Technol. 200 (2005) 2518–2524.

[142] R. O. Dillon, John A. Woollam, and V. Katkanant, Phys. Rev. B 29 (1984) 3482–3489.

[143] B. Schrader, D. Bougeard (Eds.), Infrared and Raman Spectroscopy: Methods and Applications, VCH (1995) Weinheim, Germany.

[144] F. Tuinstra, J.L. Koenig, J. Chem. Phys. 53 (1970) 1126–1130.

8 Publications

8.1 List of included publications

I. C. Saringer, A.D. Pajdarová, P. Baroch, K. Zorn, R. Franz and C. Mitterer, Three zone model for electron distribution in dc unbalanced magnetron sputtering plasma and influence of the discharge power, manuscript in final preparation

II. C. Saringer, R. Franz, K. Zorn and C. Mitterer, Effect of discharge power on target poisoning and coating properties in reactive magnetron sputter deposition of TiN, J. Vac. Sci. Technol. A 34 (2016) 041517

III. C. Saringer, C. Oberroither, K. Zorn, R. Franz and C. Mitterer, Influence of discharge power and bias potential on microstructure an hardness of sputtered a-C coatings, submitted for publication to the Journal of Vacuum Science and Technology A

IV. C. Saringer, M. Tkadletz and C. Mitterer, Restrictions of stress measurements using the curvature method by thermally induced plastic deformation of silicon substrates, Surf. Coat. Technol. 274 (2015) 68-75

8.2 Supervised diploma thesis

V. C. Oberroither, Sputter Deposition of Amorphous Carbon Thin Films in Argon, Neon and Helium Atmospheres, Montanuniversität Leoben, 2017

8.3 My contribution to the included publications

	Conception and planning[1]	Experiments	Analysis and interpretation	Manuscript preparation[1]
Publication I	90 %	80 %	80 %	90 %
Publication II	100 %	100 %	100 %	100 %
Publication III	100 %	30 %	80 %	100 %
Publication IV	100 %	100 %	100 %	100 %

[1] Supervision not included

Publication I

Three zone model for electron distribution in dc unbalanced magnetron sputtering plasma and influence of the discharge power

Christian Saringer, Andrea Dagmar Pajdarová, Pavel Baroch, Katrin Zorn, Robert Franz, Christian Mitterer

Manuscript in final preparation

Three zone model for electron distribution in dc unbalanced magnetron sputtering plasma and influence of the discharge power

Christian Saringer[a,*], Andrea Dagmar Pajdarová[b], Pavel Baroch[b], Katrin Zorn[c], Robert Franz[a],

Christian Mitterer[a]

[a] Department of Physical Metallurgy and Materials Testing, Montanuniversität Leoben, Franz-Josef-Strasse 18, 8700 Leoben, Austria

[b] Department of Physics and NTIS – European Center of Excellence, University of West Bohemia, Univerzitní 8, 306 14 Plzeň, Czech Republic

[c] MIBA High Tech Coatings, Dr.-Mitterbauer-Strasse 3, 4655 Vorchdorf, Austria

Abstract

In this paper we report on the spatial distribution of the electron energy probability function (EEPF) and several plasma properties in a direct current planar magnetron discharge, and their dependence on the discharge power. Spatially resolved Langmuir probe measurements were performed in axial and radial direction with respect to the discharge axis and the discharge power was varied between 300 and 3200 W. Based on the position within the discharge we found that the central part of the magnetron plasma can be divided into three zones, each possessing a characteristic shape of the EEPF. The plasma density and electron energy were found to be highest above the target center and to decrease quickly with increasing axial and radial distance due to a loss of high-energetic electrons. An increase of the discharge power led to a linear increase of the plasma density in the whole discharge, while the influence on the electron energy and the plasma potential was mainly confined to the discharge center. The floating potential and the EEPF remained unaltered at power levels of 800 W and above. At a lower power, however, a strongly non-linear behavior was observed,

* Corresponding author:
E-mail address: christian.saringer@unileoben.ac.at
Tel.: +43/3842 402 4239
Fax: +43/3842 402 4202

leading to the conclusion that a homogenous plasma is only established above a critical power. Based on the results a schematic model for the motion of the electrons is suggested.

1. Introduction

Magnetron sputtering as a means of depositing (multi-)functional coatings is nowadays widely used amongst researchers and in industry. It is a plasma-assisted deposition technique where a solid target is transferred to the vapor phase (i.e. sputtered), by the momentum transfer from impinging energetic ions that originate from a glow discharge. The thus generated vapor condenses on surfaces exposed to the discharge consequently forming a film [1]. The term "magnetron" refers to the installation of magnets behind the target confining electrons by a magnetic field, which considerably enhances the ionization of the working gas and thus raises the efficiency of the deposition process [1,2]. Hence, magnetron sputtering allows the deposition of thin films and coatings at low pressure at an increased deposition rate compared to the nowadays obsolescent diode sputtering [2]. Although magnetron sputtering has been subject to much research since its invention at the beginning of the 1970ies, there are still open questions remaining today. Especially phenomena occurring in the plasma, like the energy input of the particles for instance [3], and their impact on the coating properties are still not completely understood [4].

One method, that has often been used for the determination of the plasma properties in a magnetron discharge, is the so-called Langmuir probe [5,6]. Various important properties can be determined using such probes, e.g. the electron density, plasma and floating potentials and the electron mean energy. If the right measures are taken it is even possible to determine the energy distribution of the electrons [7]. Very often these probes have a spatial resolution or are movable and can hence be used for the determination of the spatial distribution of the above mentioned parameters. Rossnagel and Kaufmann [8,9] and Petrov et al. [10] performed pioneering work in the 1980ies and characterized the spatial distribution of the plasma properties at different discharge conditions and gas pressures. Bingsen and Zhou found that the characteristics of the plasma in a magnetron discharge do not depend on the target material [11]. Furthermore, Sheridan et al. [12] observed two-temperature electron energy distributions in the magnetron discharge with a subsequent investigation of the topic by Field et al. [4]. More recently, Seo et al. elucidated the influence of the substrate bias on the electron drift and loss balance of the charged particles in a magnetron discharge by the use of both, cylindrical and planar spatial Langmuir probes [13].

Although much work has already been devoted to the investigation of the plasma properties in magnetron discharges, it is up to now still not thoroughly understood. Especially the influence of the discharge power on the plasma properties and their spatial distribution have not yet been sufficiently investigated. The application of higher discharge powers is desirable in order to achieve higher thin film growth rates, which in turn can improve productivity of industrial deposition processes. In this work we have therefore used the Langmuir probe to examine the spatial distribution of the plasma properties in the central part of a planar magnetron discharge and assessed the influence of the discharge power on their spatial distribution. In total, the discharge was characterized at 15 measurement positions at axial distances from a cylindrical planar titanium target between 30 and 72 mm and at radial distances from the target center between 0 and 72 mm. The influence of the discharge power was evaluated by stepwise increasing the power from 300 to 3200 W during the probe measurements. The results presented not only allow conclusions on the spatial distribution of the plasma properties and the influence of the discharge power, but also on the motion of the electrons in the discharge.

2. Experimental methods

2.1 Magnetron sputtering system

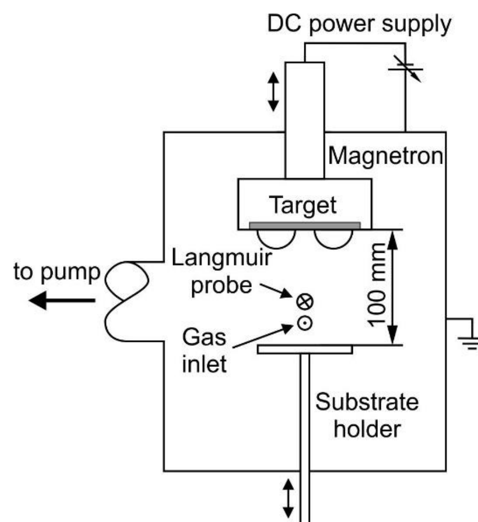

Figure 1: Schematic side view of the magnetron sputtering system used for the Langmuir probe investigations

The discharge power dependent Langmuir probe investigations were performed in a custom-made sputter deposition system which is schematically displayed in Fig.1. The system consists of two connected cylindrical steel chambers where the gas is fed into one chamber

and the pumps are attached to the other, so that the gas flows through the whole apparatus. The discharge, however, is confined to only the first chamber (which is depicted in Fig.1) where an unbalanced magnetron is used as sputtering source. This magnetron is movable along its axis, thus enabling Langmuir probe measurements at several distances from the target surface. As target, a pure titanium disc with a diameter of 100 mm and a thickness of 6 mm was used. In order to have a reproducible discharge for all the measurements, a substrate holder was positioned at 100 mm from the target surface and moved along with the magnetron to keep a constant target to substrate distance. Prior to igniting the discharge, the vacuum chamber was pumped down to a base pressure of $< 5 \cdot 10^{-3}$ Pa using a turbomolecular pump backed by a membrane pump. The base pressure was monitored with a hot cathode ion gauge. Argon was then introduced as working gas with a flow of 50 sccm. During the experiments a throttle valve was used to decrease the pumping speed in order to adjust the total pressure to 1 Pa. A capacitance manometer was used to monitor the pressure. Subsequently, a discharge was ignited using a SPIK 2000 A MELEC power generator in DC mode and the target power was set to six different values between 300 and 3200 W, which resulted in power densities with respect to the target erosion zone between 5.7 and 61 W/cm. The size of the erosion zone was determined by measuring the width of the erosion track with a sliding caliper. Figure 2 shows the discharge voltage and current density as a function of the discharge power. The substrate holder was electrically insulated from the grounded chamber walls, thus gaining a floating potential, which is also displayed as a function of the discharge power in Fig.2.

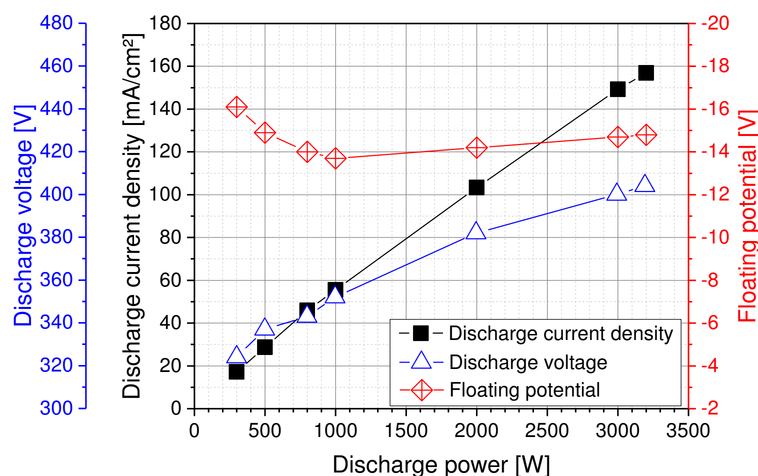

Figure 2: Discharge voltage, discharge current and floating potential as a function of the discharge power.

Figure 3 shows the magnetic field configuration of the unbalanced magnetron as measured by a Hall probe. The magnetic field in both, axial and radial direction, is strongest close to the target surface where the maximum axial field is almost 80 mT in the target center. The maximum radial field, however, is somewhat smaller (~37 mT) and occurs at a radial distance of 20 mm. The radial and axial fields strongly decrease with distance from target until they eventually become 0 and ~-2 mT, respectively. The insert in Fig.3 qualitatively demonstrates the direction of the magnetic field. It shows that the magnetron is a typical type 2 unbalanced magnetron, where the outer magnets are stronger than the center magnet [14,15]. The maximum target erosion due to the electron confinement caused by the magnetic field was observed at a radial distance of 36 mm.

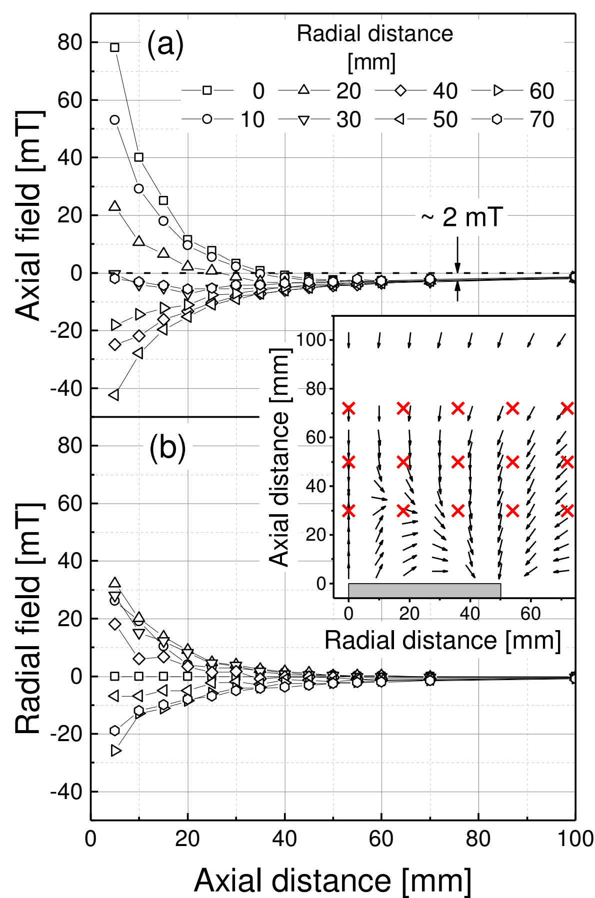

Figure 3: Magnetic field in (a) axial and (b) radial directions as a function of the axial and radial distances from the center of the target surface. The small insert qualitatively gives the direction of the magnetic field lines. The crosses (×) indicate the positions where Langmuir probe measurements were performed (see also Fig.4).

2.2 Langmuir probe measurements

The spatially resolved Langmuir probe investigations were carried out using an ALP system from IMPEDANS. It was operated with two cylindrical tungsten tips at a distance of approximately 3 mm from each other. Both tips were 12 mm in length and had a radius of 0.2 mm. During the measurements one of the two probe tips was used as reference probe accounting for possible plasma potential fluctuations. Measurements were performed at three different axial distances from the target surface (30 mm, 50 mm and 72 mm) and five different radial distances (see Fig.4). Starting from the target center (0 mm) every 18 mm one measurement was performed up to a maximum distance of 72 mm, resulting in a total of 15 different measurement positions. At each position 500 voltage runs from -50 to +15 V were performed and averaged to obtain one probe characteristic. Prior to each set of runs the probe surface was cleaned for 5 s by ion etching. For this purpose -150 V was applied to the probe tips.

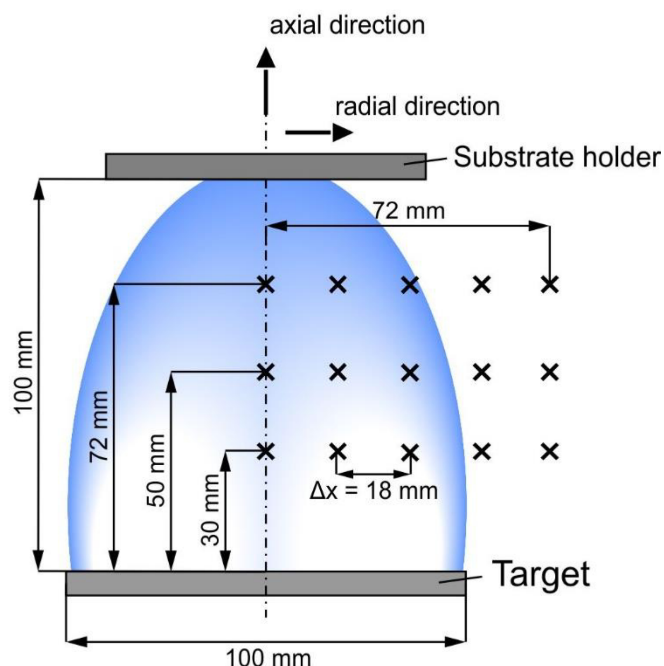

Figure 4: Schematic of the magnetron discharge. The crosses (×) indicate the locations where Langmuir probe measurements were conducted.

2.3. Langmuir probe evaluation procedure

The probe characteristics were analyzed by means of the so-called Druyvesteyn procedure [16–18]. This technique is based on the derivation of the electron energy distribution function (EEDF) from the second derivative of the measured current-voltage-characteristic. According to this procedure the EEDF, $f(E)$, with the energy E in electron volts can be written as [17–19]

$$f(E) = f(V_{pl} - V) = \frac{2\,m_e}{e\,A}\sqrt{\frac{2\,e\,(V_{pl}-V)}{m_e}}\,\frac{d^2I}{dV^2}, \quad (1)$$

where m_e is the electron mass, e is the elementary charge, A is the probe surface, I is the probe current, V is the probe voltage and V_{pl} is the plasma potential. The plasma potential was determined from the zero-crossing of the second derivative [16,20]. The difference between plasma and probe potential V_{pl}-V is equal to the energy of the electrons at potential V given in the unit of electron volts (eV). Instead of the EEDF, the electron energy probability function (EEPF), $g(E)$, is also frequently found in literature for the presentation of the electron distribution and is also used here. EEDF and EEPF are, however, closely related via the following relationship [17,20]

$$g(E) = \frac{f(E)}{\sqrt{E}}. \quad (2)$$

The measured EEPF can be fitted using the following function [21]:

$$g(E) = a\,exp(-b\,E^x), \quad (3)$$

where a, b and x are constants. The so-called Maxwellian and Druyvesteynian EEPFs are special cases with x = 1 and x = 2, respectively [18,21]. Another special case which is often encountered in magnetron sputtering discharges is the so called Bi-Maxwellian distribution function, with two Maxwellian groups of electrons. In this case the EEPF becomes

$$g(E) = g_1(E) + g_2(E) \quad (4)$$

where x_1 = x_2 = 1. In real-life magnetron sputtering plasmas, however, these ideal EEPFs are often not present and the exponents x, x_1 and x_2 range from 1 to 2. Figure 5 shows three measured EEPFs with the above mentioned fits. Although the simulated curves strongly resemble the measured ones, some deviation can be observed which is owing to fitting exponents deviating from the ideal values.

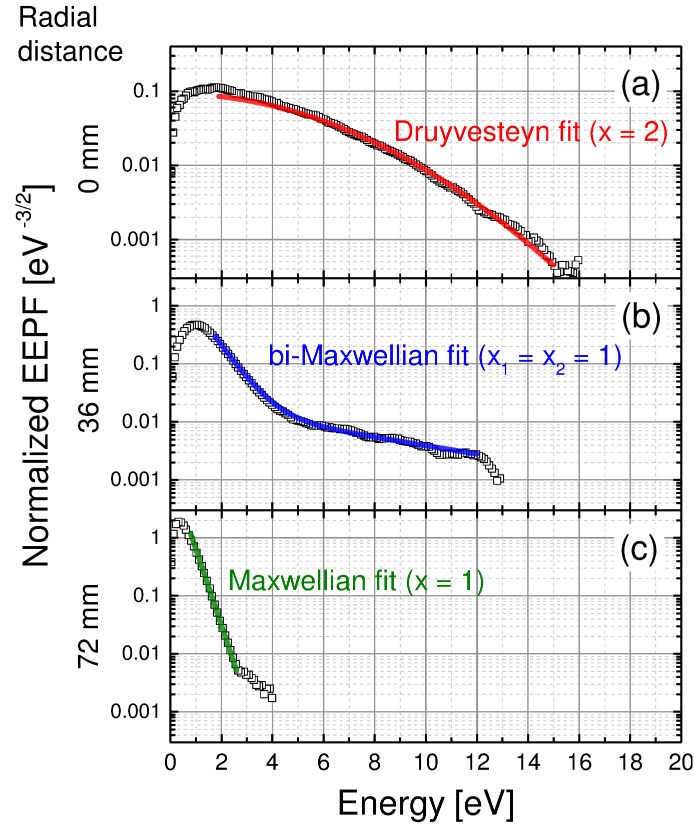

Figure 5: Fit of the EEPF of the measurements at a radial distance of 0 mm (a), 36 mm (b) and 72 mm (c), respectively, recorded at 50 mm from the target surface and at a discharge power of 2000 W. The EEPF was normalized to the electron density.

From the known EEDF the electron density n_e can be calculated by integrating over all energies [17,18]

$$n_e = \int_0^\infty f(E)\, dE \,. \tag{4}$$

From the known EEDF and electron density the average electron energy $\bar{E}$ can be calculated as

$$\bar{E} = \frac{1}{n_e}\int_0^\infty E\, f(E)\, dE \,. \tag{5}$$

In analogy to the Maxwellian energy distribution, where the electron temperature T_e is 2/3 of the mean electron energy, an effective electron temperature $T_{e,eff}$ can be defined as a measure for the kinetic energy of electrons having an arbitrary, isotropic distribution function, i.e. for electrons not having a Maxwellian EEDF [18]:

$$T_{e,eff} = \frac{2}{3}\bar{E} \,. \tag{6}$$

The floating potential V_{fl} was found directly from the I-V characteristic as the potential where the current equals zero.

A Savitzky-Golay filter [22] employing polynomials of second order was applied to smoothen the probe characteristics prior to performing the analysis explained above. This is necessary because by numerically deriving the probe characteristic, the noise originating from the plasma is amplified [20]. Thus, a smoothing procedure needs to be performed to obtain evaluable results [23]. The number of points used for fitting (i.e. the size of the fitting window) was chosen in order to obtain best smoothing at minimum distortion of the maximum of the second derivative. The number of points used as a function of the radial distance is displayed in table 1.

Table 1: Number of points used for the Savitzky-Golay smoothing of the probe characteristics.

Radial distance [mm]	0	18	36	54	72
Number of points used for fitting	21	21	31	11	11

In order to determine, whether a correction of the Langmuir probe measurements due to the magnetic field needed to be performed or not, a mean electron gyration radius $\bar{\rho}$ was calculated using the following equation [24]

$$\bar{\rho} = \frac{m_e \, \overline{v_T}}{e \, |\vec{B}|} = \frac{\sqrt{2 \, m_e \, T_{e,eff}}}{e \, |\vec{B}|}, \tag{7}$$

where $\overline{v_T}$ is the mean thermal velocity of the electrons and $|\vec{B}|$ is the absolute value of the magnetic field. Since the magnetic field at the measurement positions was quite low ($\lesssim$ 10 mT), the calculated mean gyration radii were in all cases larger than the probe radius and hence no corrections for the magnetic field needed to be performed [16,25].

3. Results

3.1 Spatial distribution of the electron energy probability function

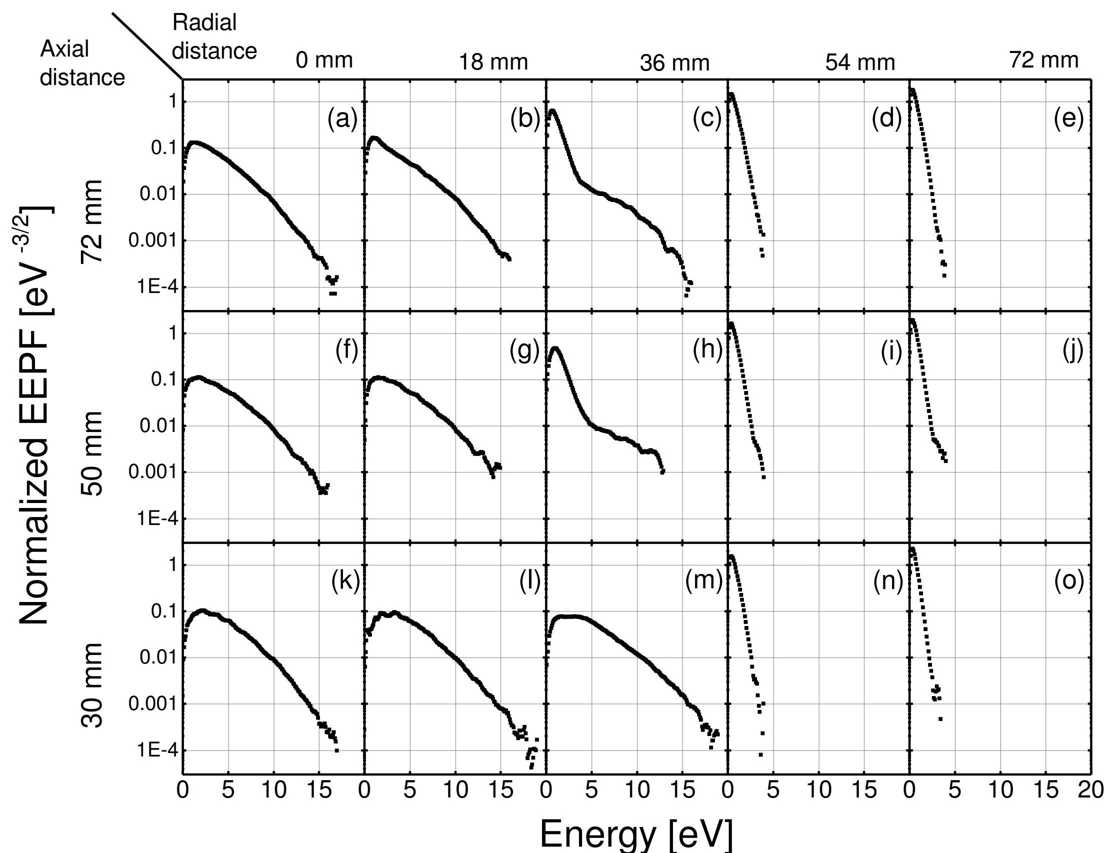

Figure 6: The EEPF as a function of the axial and radial distances at a discharge power of 2000 W. The EEPF was normalized to the electron density.

Figure 6 shows the spatial distribution of the normalized EEPF measured at a constant discharge power of 2000 W. The shape of the EEPF is apparently strongly dependent on the position within the discharge. Based on the observed EEPF, the discharge can be divided into different zones. At the axial distances of 50 and 72 mm from the target surface, three distinct zones as a function of the radial distance can be observed. Zone 1 is directly above the target center (radial distance 0 to 18 mm) where the shape of the EEPF is strongly Druyvesteyn-like (compare also the fit in Fig.5a). The energy range of the electrons spans from lower energies to higher energies exceeding 15 eV. Moving farther away from the center, the shape of the EEPF indicates a depletion of the high-energetic electrons. This depletion of electrons with a high energy results in a typical two-group-EEPF, similar to a bi-Maxwellian shape (see Fig.5b) at a radial distance of 36 mm, i.e. directly above the zone of maximum target erosion. This zone 2 can be seen as a transition zone between zone 1 and zone 3 (radial distance ≥ 54 mm),

where the EEPF is Maxwellian-like (Fig.5c). Only electrons with very low energy $\lesssim$ 4 eV are present in zone 3. Closer to the target, i.e. at 30 mm from the target surface, the transition region apparently vanishes and only the zones 1 and 3 were observed.

In general, two major trends can be observed from the spatially resolved EEPF:

1. With increasing radial distance a depletion of high energy electrons takes place, which leads to a change of the shape of the EEPF from Druyvesteyn-like to Maxwellian-like (Figs.6f-j). Similar trends were observed by Sheridan et al. [26] and Seo et al. [13,27].

2. Above the region of maximum target erosion (radial distance 36 mm) the EEPF changes from a two-temperature-EEPF to Druyvesteyn-like with decreasing axial distance, i.e. closer to the target surface more high-energetic electrons are found (Figs.4 h and m).

The second trend is in accordance to Sheridan et al. who reported a plasma with a single hot electron component close to the target [12]. With increasing target distance they noticed a change to a bi-Maxwellian plasma with a hot and cold electron component. The same trend can also be recognized in the current work when comparing Fig.6b and Fig.6g. The EEPF in Fig.6b is not purely Druyvesteynian and some minor “peak” of the EEPF can be observed at approximately 2 eV which is not present in Fig.6g.

Figure 7 shows the influence of the discharge power on the shape of the EEPF. The curves were taken at an axial distance of 50 mm, with each graph representing a typical EEPF for the three encountered zones. Furthermore, the energies for the most important inelastic collisions are indicated [28]. At first glance the discharge power does not seem to have a large influence on the shape of the EEPF. Essentially, the EEPF stays Druyvesteynian-like, Maxwellian-like or bi-Maxwellian-like depending solely on the position in the discharge and simply the number of electrons is rising with power. However, if taking a closer look at Fig.7b and c (zones 2 and 3), where the EEPFs are (bi-)Maxwellian-like, one can see that the EEPF is changing nonlinearly between 300 and 800 W. In both zones, the density of higher energetic electrons decreases while the low energy electrons increase. At powers exceeding 800 W, the EEPF is stabilized and the increase is linear with power. In zone 1 (Fig.7a) mainly the proportion of the high-energetic electrons is increasing while the proportion of the low-energetic electrons decreases with power.

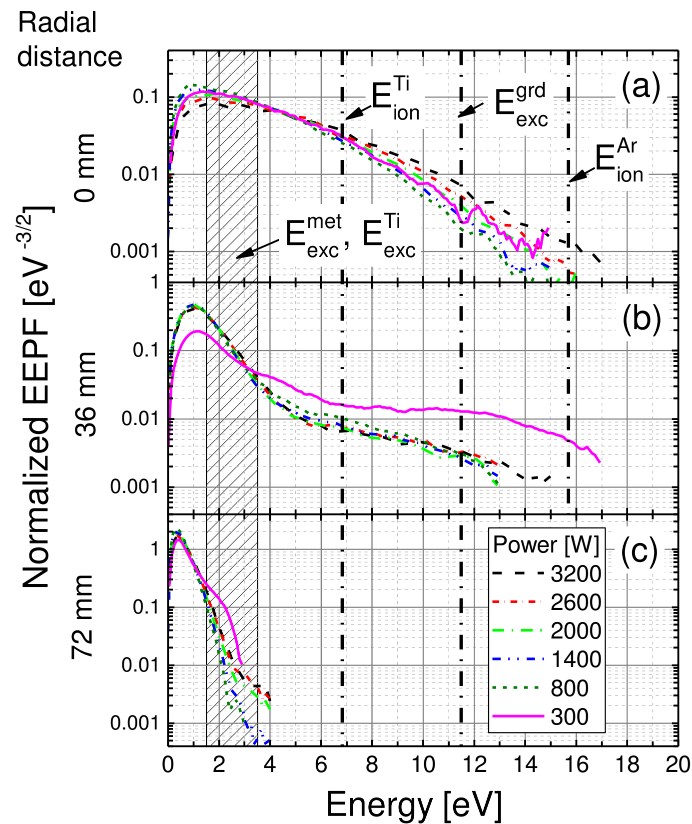

Figure 7: Influence of the discharge power on the EEPF for zone 1 (a), zone 2 (b) and zone 3 (c). The EEPF was normalized to the electron density. The discharge power was 2000 W. The distance from the target surface was 50 mm. The ionisation energies of argon E_{ion}^{Ar} and titanium E_{ion}^{Ti}, the minimum energy necessary to excite argon from the ground state E_{exc}^{grd} and the energy range for the most important transitions from metastable states of argon E_{exc}^{met} and the excitation energies of titanium E_{exc}^{Ti} are also indicated.

3.2 Spatial distribution of plasma properties

The change of the electron density within the discharge at different power levels is summarized in Fig.8. Depending on the position within the discharge and the discharge power, density values between ~10^{15} and 10^{17} m^{-3} were encountered, which are typical plasma density values for an argon magnetron discharge [9,10,29]. For all investigated discharge powers, the electron density was found to be highest above the target center (radial distance ≤ 18 mm) and to decrease strongly with increasing radial distance. In all cases, the values at the edge of the discharge are approximately one order of magnitude lower than in the center. The densest plasma is not formed above the point of maximum target erosion (radial distance 36 mm) but at about 18 mm. The change of the electron density with increasing distance from the target surface, however, is less pronounced. Only a small decrease can be detected above

the target center, where the discharge is mainly confined. An increase of the discharge power results in an increase of the electron density which is roughly linear being a result of the higher current that is present at higher power levels [9,11,30]. As the power was raised from 300 to 3200 W, i.e. by a factor of 10, the electron density increased by almost one order of magnitude homogeneously over the investigated area, as well.

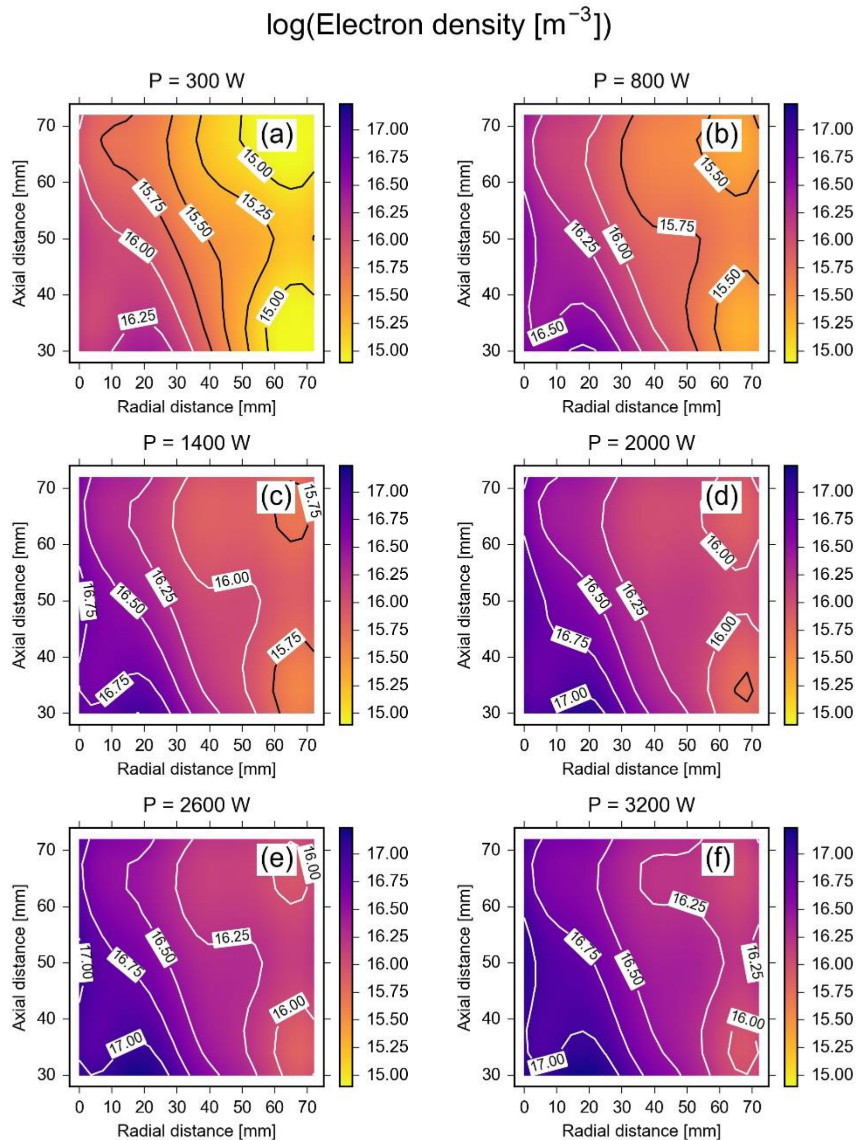

Figure 8: Color mappings representing the spatial distribution of the electron density at different discharge powers. The electron density is presented as the common logarithm of its value. The measurement points were interpolated using a multiquadric interpolation.

As shown in Fig.9, the three zones observed for the shape of the EEPF (Fig.6) can also be recognized from the spatial distribution of the effective electron temperature at discharge

powers exceeding 800 W. It can be seen that the more energetic electrons are found above the target center and close to the target surface, where the EEPF was found to be mainly Druyvesteynian-like. The effective electron temperature there is high (≳ 3 eV). With increasing distance from the target the electron temperature decreases. At the edge of the discharge (Maxwellian-like EEPF, radial distance ≥ 54 mm), the electron temperature is low ($T_{e,eff}$ < 1 eV) and constant for all axial distances. In between there is the bi-Maxwellian-like transition zone, where the electron temperature rapidly decreases from above 3 to below 1 eV. Similar spatial trends have already been reported in literature for other magnetron discharges [4,9,10,26].

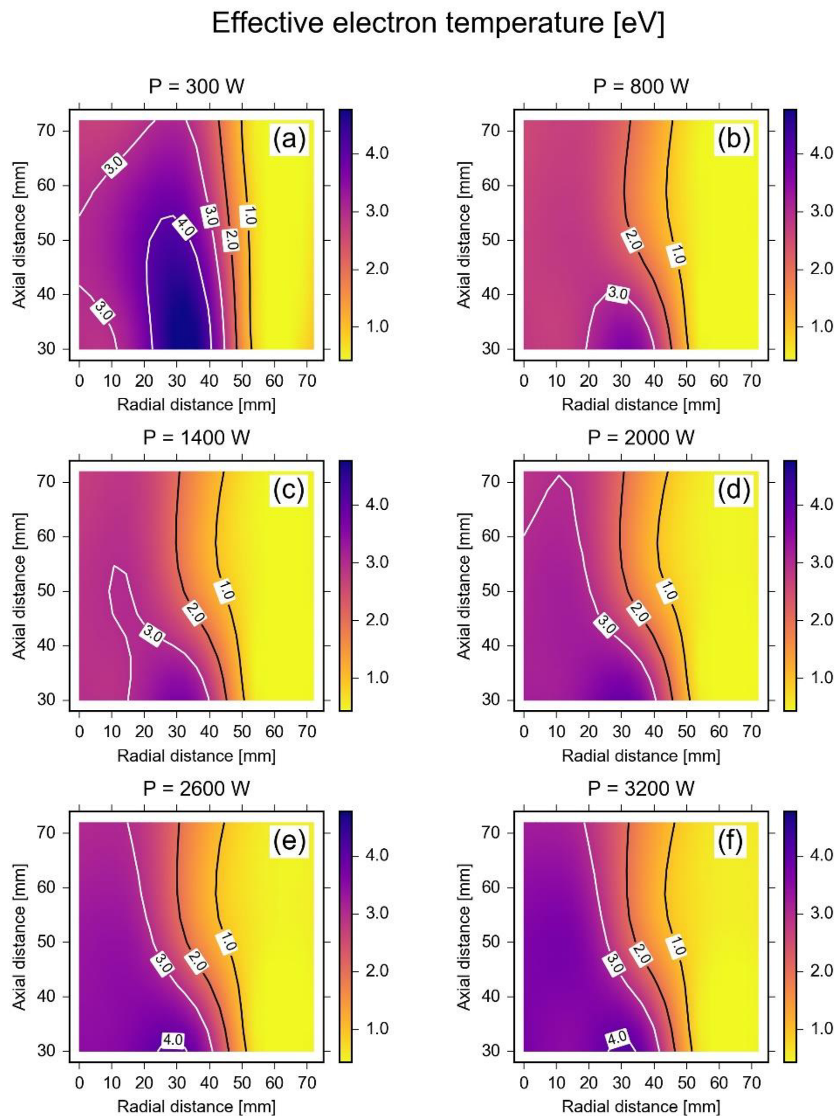

Figure 9: Color mappings representing the spatial distribution of the effective electron temperature at different discharge powers. The measurement points were interpolated using a multiquadric interpolation.

The overall effect of a higher discharge power is mainly an increase of the electron temperature in the center of the discharge, see Fig.9 b-f. At 800 W the maximum effective electron temperature in the volume examined is approximately 3 eV and increases to 4 eV at 3200 W. At a radial distance exceeding 40 mm, the electron temperature is mainly unaffected. This change is also reflected by the shape of the EEPF (compare Fig.7). At the edge of the discharge the EEPF is simply increasing linearly with power and the effective electron temperature is unaffected. In the center, however, it was found that mainly the density of the high-energetic electrons increases when the power is raised above 1400 W, hence elevating the effective electron temperature. From 300 to 800 W, on the other hand, a different trend

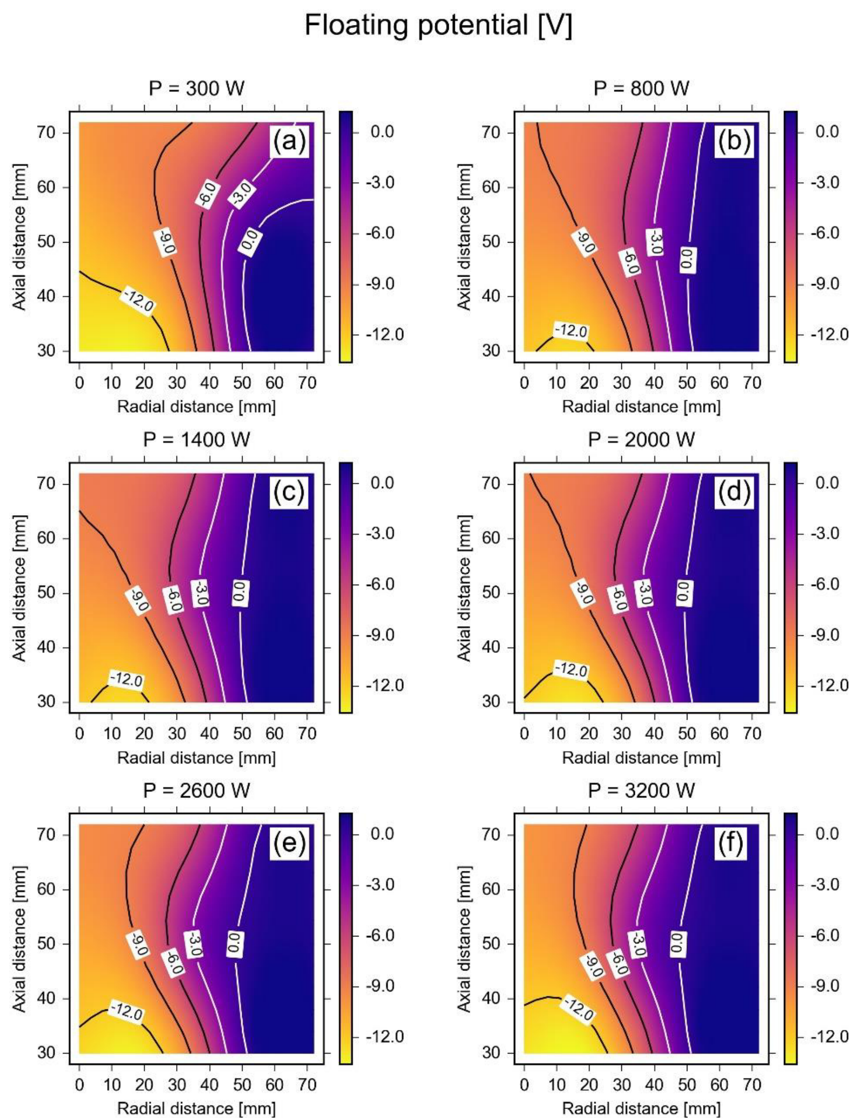

Figure 10: Color mappings representing the spatial distribution of the floating potential at different discharge powers. The measurement points were interpolated using a multiquadric interpolation.

is observed. At 300 W a zone with highly energetic electrons can be detected, which vanishes at 800 W. This can also be explained by the change of the EEPF from 300 to 800 W (again compare Fig.7). Wu et al. have also found a decrease of the electron temperature at discharge powers below 2000 W for their sputtering system, which changed to an increase at elevated powers [30]. However, they have not given a clear explanation on this.

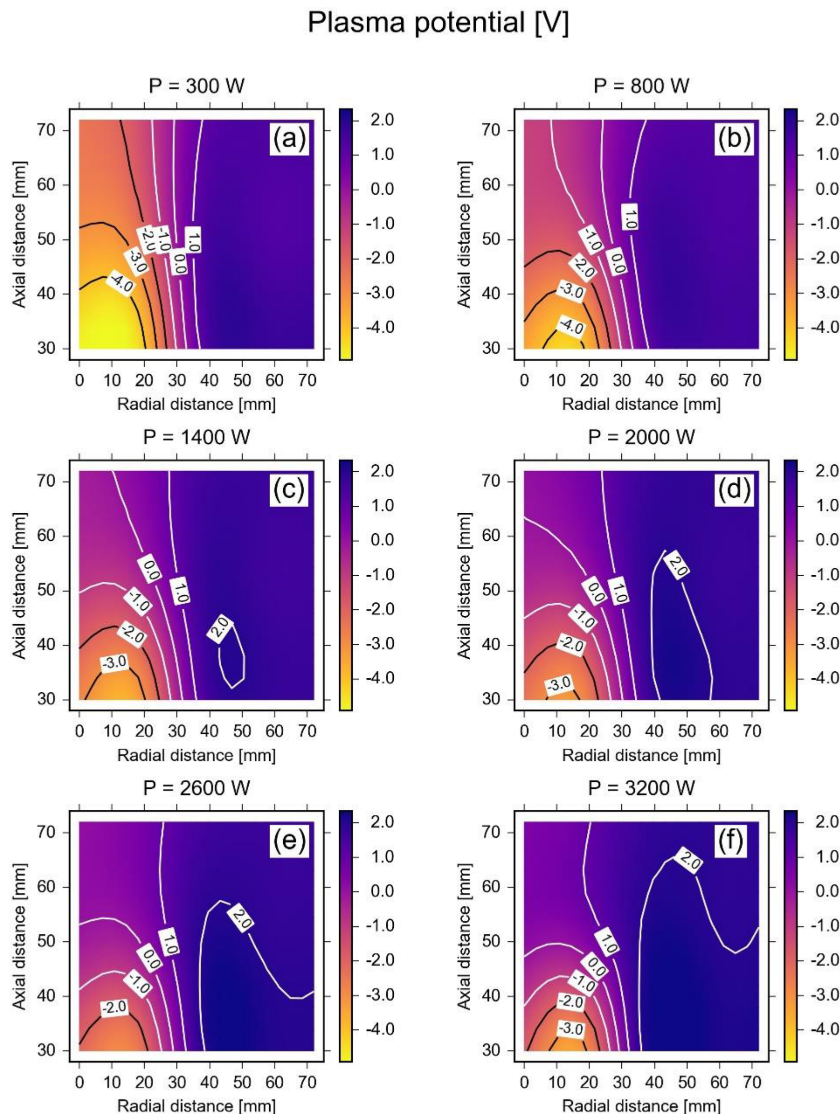

Figure 11: Color mappings representing the spatial distribution of the plasma potential at different discharge powers. The measurement points were interpolated using a multiquadric interpolation.

The spatial distributions of floating and plasma potential are shown in Figs.10 and 11, respectively. Evidently both potentials are most negative above the target center and close to the target surface ($V_{fl} \approx$ -12 V, $V_{pl} \approx$ -4 V). With radial and axial distance they increase to more positive values. Above the target center, the floating potential is generally strongly negative and only a small increase with axial distance can be found. The increase, however, is much

stronger with radial distance and the floating potential becomes even slightly positive with respect to the chamber wall when the radial distance is larger than 54 mm, i.e. in zone 3. The plasma potential shows a similar trend, however, a stronger increase with axial distance can be detected in the discharge center. Although, the plasma potential is usually the most positive potential in a dc glow discharge [31], negative plasma potential values are frequently observed in magnetron discharges, especially at distances closer to the target surface [12,13,27,32,33]. The distribution of the plasma potential presented here is consistent with the results of Goeckner et al., who reported the negative plasma potential to be a consequence of the cathode pre-sheath [34].

While the spatial distributions of floating and plasma potential are quite similar, the effect of the discharge power is different. Fig.10 shows that the floating potential is hardly influenced by the discharge power. From 800 to 3200 W the values as well as the shape of the contour lines remain largely unaltered. A major change with discharge power can only be seen at the lowest power densities, i.e. when comparing the graphs for 300 and 800 W. At 300 W a negative floating potential can be detected not only above the target center, but also at larger radial distances at 72 mm from the target surface. When increasing the discharge power to 800 W, a positive floating potential evolves at this point and an increase of the power does not have any further influence on the floating potential. A similar non-linear behavior is observed for the floating potential gathered by the substrate holder (Fig.2). Below 800 W, there is an increase of the substrate holder from -16 to -14 V, above which the floating potential slightly decreases again to -15 V.

In contrast to the floating potential, which is not influenced by the discharge power, the plasma potential shows a clear increase with power above the target center (zone 1) and also some minor increase at the edge of the discharge (zone 3). While at 300 W, the minimum plasma potential is < -4 V above the center, it increases to approximately -2 V at 2600 W. From 2600 to 3200 W a decrease of the minimum plasma potential can be seen.

4. Discussion

4.1 Spatial distribution of the plasma properties

The presented Langmuir probe results are by trend largely in agreement with those reported by other researchers [4,8,11,13,27]. As expected, the plasma in the central part of the magnetron discharge is inhomogeneous. However, according to the obtained results the discharge can be divided into three zones, which are characterized by specific EEPFs and

plasma properties. Furthermore, the results allow conclusions on the electron transport within the discharge. Figure 12 presents a schematic model of the discharge summarizing the main spatial trends encountered. In the following section the discharge will be discussed in detail.

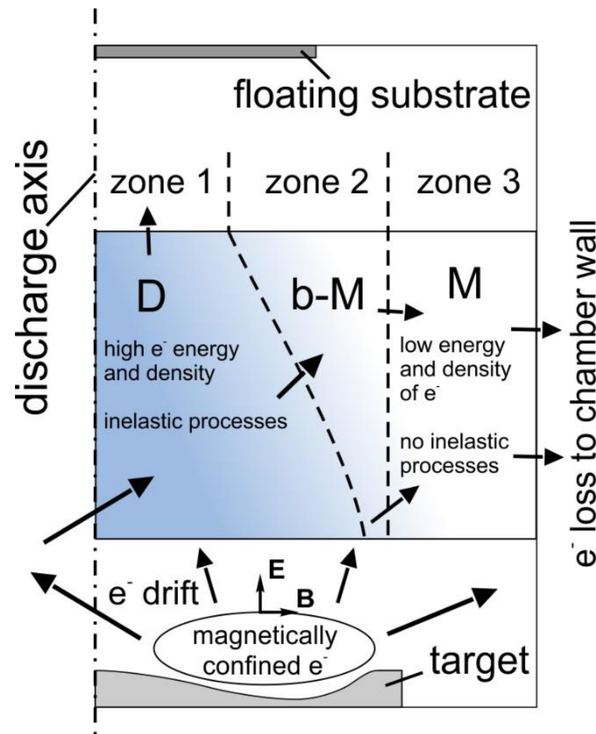

Figure 12: Schematic model for the spatial structure of the plasma and electron transport in a DC planar magnetron discharge with floating substrate. The blue colour is indicative for the visually observed glow of the discharge. D, b-M and M indicate the shape of the EEPF in the respective zones to be Druyvesteynian-like, bi-Maxwellian-like and Maxwellian-like, respectively. The arrows indicate the direction of the electron motion with their size qualitatively representing the amount of drifting electrons. E and B are the electrical and magnetic field, respectively.

The principle of magnetron sputtering is based on the confinement of electrons close to the target surface by a magnetic field [31]. This enhances the ionization of the working gas and the sputtered material in that region and leads to the usually recognized inhomogeneous erosion of the target in the planar configuration. The confinement of the electrons is strongest in the region where the electric field E and the magnetic field B are oriented orthogonally with respect to each other, which is also the region where the $E \times B$ drift is most pronounced. This leads to the situation that electrons preferentially escape in directions other than along the target surface normal, i.e. in the direction of the electric field [27,31]. The electrons escaping the drift region then follow the magnetic field lines, which are directed towards the center of the discharge. Hence, the electrons from the total target surface are concentrated above the target center and the highest electron density is found in zone 1 and not above the point of

maximum target erosion, where the amount of titanium atoms is highest in the plasma (radial distance 36 mm). Additionally, the electrons obviously exhibit a comparatively high energy in the center, reflected by the elevated effective temperature. However, according to our measurements (Fig.7a) only a small amount of electrons has an energy exceeding the first ionization energy of argon (15.76 eV [35]). Consequently, ion generation can only take place in a region closer to the target, where the electrons have sufficient energy. The minimum energy necessary for argon excitation from the ground state is considerably lower (11.55 eV [28]) and excitation from the ground state takes place in zone 1. Furthermore, two step excitation mechanisms are possible, which need a noticeably lower electron energy (approximately 2-3 eV [28]) when the argon atom is already in an excited state. As a consequence, the visually observed glow indicated in Fig.11 is strongest above the target center. Also, the ionization and excitation energies of titanium are comparatively low (6.83 eV for the ionization of titanium [35]). Thus inelastic collisions with titanium play a considerable role as well, especially at elevated powers, since at higher powers more atoms are sputtered from the target. Resulting from the concentration of electrons escaping the magnetic trap and the inelastic collisions with atoms and ions, a non-equilibrium Druyvesteyn-like electron distribution is present in zone 1.

From zone 1 the electrons drift away following the increasing plasma potential in both axial and radial direction and the loss of the electrons in the radial direction leads to a decrease of the plasma density along the discharge axis in zone 1. The high-energetic electrons have sufficient energy to overcome the potential barrier between plasma and chamber wall/substrate. Thus, since the mean free path for electrons is comparatively high ($\sim$ 10 cm [1]) these high-energetic electrons are lost, while the low-energetic electrons are confined in the discharge [27]. This causes a decrease in the number of electrons with energies exceeding approximately 5 eV and results in an EEPF with two groups of electrons in zone 2 [12,27]. Consequently, the effective electron temperature rapidly drops in this zone. Due to the fact, that high-energetic electrons are lost, metastable argon atoms become less abundant as well and inelastic collisions are less likely. Furthermore, the density of sputtered titanium atoms is comparatively low at the edge of the discharge. Thus, electron-electron collisions become predominant and the EEPF evolves towards a more equilibrium distribution. Finally, at the edge of the discharge in zone 3 only low-energetic electrons are present. As light electrons and heavy atoms exhibit a great difference in mass, the elastic energy exchange between them is practically non-existing [31] and electrons can only exchange energy among themselves. Thermalized in this way, the electrons evolve towards the equilibrium Maxwellian EEPF.

4.2 Influence of discharge power

According to the obtained results, two power ranges can be differentiated, a low power range below 800 W and a high power range above 800 W. When the discharge power was increased from 300 to 800 W, some plasma properties showed a strongly non-linear behavior. More specifically, the floating potential was strongly negative at large distances from the target (> 60 mm) at 300 W and increased to a constant value at discharge powers higher than 800 W. Also, in zone 1 a high effective electron temperature of > 4 eV could be found at 300 W which diminished at 800 W. This high electron temperature is due to the non-linear change of the shape of the EEPF from 300 to 800 W displayed in Fig.6. The reason for this behavior at the lower discharge power is most probably the gas rarefaction in front of the target, or "sputtering wind" first described by Hoffman [36]. The decrease of pressure in front of the target due to this gas rarefaction is strongest at lower discharge currents. When the current is increased, however, the pressure change due to the gas rarefaction is not pronounced [37]. Since at lower power the electron density is quite low, the high-energetic electrons can escape the trap into the discharge without experiencing too many collisions with other electrons. When the power however is increased, the pressure in front of the target is not changing any more while the electron density keeps increasing. Consequently the high-energetic electrons suffer from increasing collisions on their way to the anode and the shape of the EEPF changes. This can be best seen in Fig.6b, when comparing the curves for 300 and 800 W. There, the number of high-energetic electrons decreases, while the low-energetic electrons accumulate.

Above 800 W the influence of the discharge power is mainly confined to zone 1 and at radial distances exceeding 36 mm only a small increase of the plasma potential can be observed. Above the target center, however, both, the plasma potential and the effective electron temperature, increase. The higher effective electron temperature can be connected to the increased target voltage at elevated power: When the voltage is rising, the secondary electrons generated at the target surface gain a higher energy when being accelerated through the cathode fall. However, the electrons suffer from collisions, both elastic and inelastic, quickly distributing their energy. Thus the average electron temperature rises only in zone 1 and the effective electron temperature is not affected at the edge of the discharge.

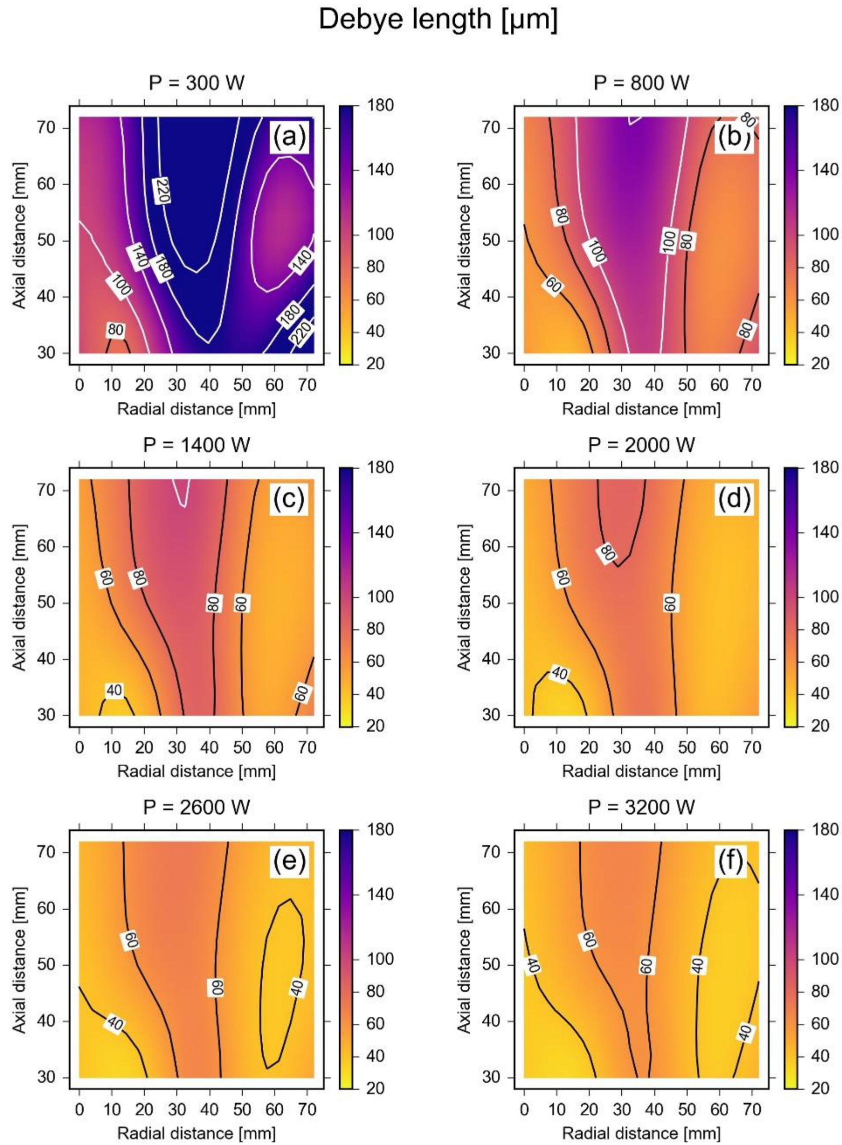

Figure 13: Color mappings representing the spatial distribution of the Debye length calculated using equation 8 at different discharge powers. The measurement points were interpolated using a multiquadric interpolation.

In order to discuss the increasing plasma potential it is useful to evaluate the Debye length λ_D, which is a parameter describing the shielding of the plasma. λ_D can be calculated using the following equation [31]

$$\lambda_D = \left(\frac{k\,\epsilon_0\,T_e}{e^2 n_e}\right)^{\frac{1}{2}}, \tag{8}$$

with k being the Boltzmann constant and ϵ_0 being the permittivity of vacuum. The lower λ_D, the smaller is the range of a disturbance within the plasma, like the disturbances caused by

the chamber walls or the cathode for instance. The sheath, that is established when the plasma is in contact to an object, usually has a dimension of some λ_D, while the pre-sheath extends much farther into the discharge [38]. The spatial distribution of λ_D calculated by equation 8 is displayed in Fig.13. As a rough approximation $T_{e,eff}$ was used for the calculation instead of T_e. While the electron density in zone 1 increases by a factor of around 3 when the power is raised from 800 to 3200 W, the maximum effective electron temperature increases only slightly (from ~ 3 to 4 eV). Thus, λ_D decreases from approximately 80 to less than 40 µm with power and consequently the shielding is more effective. The cathode sheath and pre-sheath contract, leading to an elevated plasma potential in the center. This reduced sheath thickness with increasing target voltage/current has also been reported by Rossnagel and Kaufman [8,9]. From the spatial distribution of λ_D zone 2, i.e. the zone where the high-energetic electrons are lost, can clearly be recognized as a zone of low shielding and λ_D is consequently highest. In zone 3 a high shielding is again predominant, however, contrary to zone 1 where the small λ_D was caused by a high plasma density, the high shielding in zone 3 is a result of the low effective electron temperature.

5. Conclusions

A Langmuir probe was used to investigate the spatial distribution of the plasma properties and electron transport in the central part of a planar magnetron discharge at discharge powers between 300 and 3200 W. The obtained probe characteristics were analyzed by the Druyvesteyn procedure in order to determine the electron energy probability function (EEPF) as well as plasma density and potential, the floating potential and the effective electron temperature. Based on these measurements we found that the central region of a magnetron discharge can be divided into three distinct zones with respect to the radial distance from the discharge axis. In zone 1, situated above the target center, the electron density was highest and the electrons exhibited a non-equilibrium EEPF, which could be attributed to the electrons escaping the magnetic trap in front of the target and excitation and ionization processes. High-energetic electrons have sufficient energy to overcome the potential barrier close to the chamber walls and are hence easily lost, which resulted in a bi-Maxwellian EEPF in the intermediate zone 2. This electron loss was concomitant with a decrease of the effective electron temperature. At the edge of the discharge (zone 3), only low-energetic electrons with an equilibrium Maxwellian EEPF were present. Hence, it can be concluded that inelastic electron scattering processes predominantly take place in zone 1. However, only few electrons have an energy exceeding the ionization potential of argon from

the ground state and the predominant type of inelastic collisions is one and two-step excitation of argon.

While the EEPF and the floating potential were practically unaffected by an increase of the discharge power, both the electron density and plasma potential rose with power. This behavior could be attributed to the higher discharge current that needs to be carried by the plasma at higher power and a more efficient plasma shielding. Due to this increased shielding of the plasma, the cathode pre-sheath was found to contract with increasing power. At the lowest power, however, non-linear trends were observed: EEPF, floating potential and electron temperature showed a strongly irregular behavior when the power was increased from 300 to 800 W. This was attributed to the decrease of pressure due to the sputtering wind, which saturates at higher discharge powers. These results therefore indicate, that in order to establish a stable plasma a minimum power is required, which was between 300 and 800 W in the present case.

6. Acknowledgments

The authors would like to thank Dr. Jiři Rezek (Department of Physics, University of West Bohemia) for the help with the sputter deposition plant. This work was financially supported by the Austrian Federal Government (in particular from Bundesministerium für Verkehr, Innovation und Technologie and Bundesministerium für Wissenschaft, Forschung und Wirtschaft) represented by the Österreichische Forschungsförderungsgesellschaft mbH within the project SmartCoat - Eco (project number 843621).

7. References

[1] W.D. Westwood, Sputter Deposition, AVS (2003) New York, USA.
[2] M. Ohring, The Materials Science of Thin Films, Academic Press (1991) San Diego, USA.
[3] J.G. Han, J. Phys. D: Appl. Phys. 42 (2009) 43001.
[4] D.J. Field, S.K. Dew, R.E. Burrell, J. Vac. Sci. Technol. A 20 (2002) 2032.
[5] B.E. Cherrington, Plasma Chem. Plasma Process. 2 (1982) 113–140.
[6] J.A. Thornton, J. Vac. Sci. Technol. 15 (1978) 188.
[7] V.A. Godyak, in: O. Auciello, et al. (Eds.), Plasma-Surface Interactions and Processing of Materials, Springer Netherlands (1990) Dordrecht, Netherlands, pp. 95–134.
[8] S.M. Rossnagel, H.R. Kaufman, J. Vac. Sci. Technol. A 5 (1987) 2276.
[9] S.M. Rossnagel, H.R. Kaufmann, J. Vac. Sci. Technol. A 4 (1986) 1822.

[10] I. Petrov, V. Orlinov, I. Ivanov, J. Kourtev, Contrib. Plasm. Phys. 28 (1988) 157–167.
[11] H. Bingsen, C. Zhou, Surf. Coat. Technol. 50 (1992) 111–116.
[12] T.E. Sheridan, M.J. Goeckner, J. Goree, J. Vac. Sci. Technol. A 9 (1991) 688.
[13] S.-H. Seo, J.-H. In, H.-Y. Chang, J. Appl. Phys. 97 (2005) 23305.
[14] B. Window, N. Savvides, J. Vac. Sci. Technol. A 4 (1986) 196.
[15] P. Kelly, R. Arnell, Vacuum 56 (2000) 159–172.
[16] Pfau S, Tichý M, in: R. Hippler, et al. (Eds.), Low Temperature Plasmas: Fundamentals, Technologies and Techniques, 2nd ed., Wiley-VCH (2008) Weinheim, Germany, pp. 175–213.
[17] V.A. Godyak, V.I. Demidov, J. Phys. D: Appl. Phys. 44 (2011) 269501.
[18] M.A. Lieberman, A.J. Lichtenberg, Principles of Plasma Discharges and Materials Processing, 2nd ed., Wiley-Interscience (2005) Hoboken, USA.
[19] M.J. Druyvesteyn, Z. Physik 64 (1930) 781.
[20] V.A. Godyak, B.M. Alexandrovich, J. Appl. Phys. 118 (2015) 233302.
[21] J.T. Gudmundsson, J. Alami, U. Helmersson, Surf. Coat. Technol. 161 (2002) 249–256.
[22] A. Savitzky, M.J.E. Golay, Anal. Chem. 36 (1964) 1627–1639.
[23] F. Magnus, J.T. Gudmundsson, Rev. Sci. Instrum. 79 (2008) 73503.
[24] U. Stroth, Plasmaphysik: Phänomene, Grundlagen, Anwendungen, Vieweg und Teubner (2011) Wiesbaden, Germany.
[25] J.G. Laframboise, J. Rubinstein, Phys. Fluids 19 (1976) 1900.
[26] T.E. Sheridan, M.J. Goeckner, J. Goree, Jpn. J. Appl. Phys. 34 (1995) 4977.
[27] S.-H. Seo, J.-H. In, H.-Y. Chang, Plasma Sources Sci. Technol. 13 (2004) 409.
[28] S. Konstantinidis, F. Gaboriau, M. Gaillard, M. Hecq, A. Ricard, in: R. Hull, et al. (Eds.), Reactive Sputter Deposition, Springer (2008) Berlin, Germany, pp. 301–335.
[29] E. Passoth, P. Kudrna, C. Csambal, J.F. Behnke, M. Tichý, V. Helbig, J. Phys. D: Appl. Phys. 30 (1997) 1763.
[30] S.Z. Wu, J. Appl. Phys. 98 (2005) 83301.
[31] B.N. Chapman, Glow Discharge Processes: Sputtering and Plasma Etching, John Wiley and Sons (1980) New York, USA.
[32] S.-H. Seo, J.-H. In, H.-Y. Chang, J. Appl. Phys. 96 (2004) 57.
[33] S.M. Borah, H. Bailung, J. Chutia, J. Phys.: Conf. Ser. 208 (2010) 12128.
[34] M.J. Goeckner, J. Goree, T.E. Sheridan, J. Vac. Sci. Technol. A 8 (1990) 3920.
[35] D.R. Lide, L.I. Berger (Eds.), Handbook of Chemistry and Physics: A Ready-Reference Book of Chemical and Physical Data, 85th ed., CRC Press (2004) Boca Raton, USA.
[36] D.W. Hoffman, J. Vac. Sci. Technol. A 3 (1985) 561.

[37] S.M. Rossnagel, J. Vac. Sci. Technol. A 6 (1988) 19.
[38] K.-U. Riemann, J. Phys. D: Appl. Phys. 24 (1991) 493.

Publication II

Effect of discharge power on target poisoning and coating properties in reactive magnetron sputter deposition of TiN

Christian Saringer, Robert Franz, Katrin Zorn, Christian Mitterer

Journal of Vacuum Science and Technology A 34 (2016) 041517

Effect of discharge power on target poisoning and coating properties in reactive magnetron sputter deposition of TiN

Christian Saringer[a,*], Robert Franz[a], Katrin Zorn[b], Christian Mitterer[a]

[a] Department of Physical Metallurgy and Materials Testing, Montanuniversität Leoben, Franz-Josef-Strasse 18, 8700 Leoben, Austria

[b] MIBA High Tech Coatings, Dr.-Mitterbauer-Strasse 3, 4655 Vorchdorf, Austria

Abstract

Reactive magnetron sputtering is a well-established technique for the deposition of high quality functional compound coatings. However, avoiding the undesired hysteresis effect that occurs when the metal target becomes covered by a compound layer at a certain reactive gas flow or partial pressure, typically referred to as target poisoning, is still an intense field of research. In the current work, the effect of the discharge power on target poisoning and coating structure and properties was assessed by determining the hysteresis and by characterizing the sputter-deposited TiN_x coatings, where $x \leq 1$. With increasing discharge power, the hysteresis was shifted to higher N_2 gas flow values. In metallic mode, the increase in discharge power enabled therefore the incorporation of high nitrogen fractions in the TiN_x coatings at stable discharge conditions and high deposition rates. In poisoned mode, all coatings were stoichiometric, but the deposition rates were lower by a factor of 1/3. Regardless of the deposition mode, grain refinement and high stresses generated due to the increase of deposition rate at elevated deposition power increased the hardness and elastic modulus of the deposited TiN_x coatings. At a power density of 34 W/cm² the hysteresis was largely eliminated and a deposition rate of 0.15 µm/min for stoichiometric TiN_x with high hardness of up to ~30 GPa could be achieved. The results presented in this paper demonstrate

* Corresponding author:
E-mail address: christian.saringer@unileoben.ac.at
Tel.: +43/3842 402 4239
Fax: +43/3842 402 4202

that increasing the discharge power density facilitates the deposition of stoichiometric TiN by operating in the metal/transition mode.

1. Introduction

Direct current (DC) reactive magnetron sputter deposition (MSD), which can be defined as the synthesis of compound coatings by the DC sputtering of a metallic target in a chemically reactive atmosphere [1–3], is a method that is widely applied for the deposition of functional films such as hard coatings [3,4], conductive and non-conductive oxide layers [4] and diffusion barriers in microelectronics [5]. DC reactive MSD as a means of depositing compounds has many advantages compared to the sputtering of a compound target, e.g., increased deposition rate, adjustability of the chemical composition and absence of expensive radio frequency equipment in case of insulating materials [1,6]. However, one major issue needs to be considered which is the covering of the metal target by a compound layer at increased reactive gas flows, commonly referred to as “target poisoning” [1].

This poisoning effect usually takes place abruptly at a certain reactive gas flow and leads to a considerable change of the process conditions. One detrimental consequence is a large drop of the deposition rate which scales with a factor of approximately 3 - 4 in the case of nitrides and 10 - 15 in the case of oxides [2]. In order to “de-poison” or “recover” the target and to again obtain a high deposition rate after poisoning, the reactive gas flow needs to be reduced. When the target is in the “unpoisoned” (typically referred to as metallic) state, however, it is usually difficult to deposit compound coatings with the desired stoichiometric chemical composition [1]. Moreover, poisoning and de-poisoning do not occur at the same reactive gas flow which results in the well-known hysteresis behavior [7–9]. In the hysteresis region between poisoning and de-poisoning the discharge is unstable and time-dependent. Since synthesizing coatings exactly in this unstable transition region would be desirable as a stoichiometric coating composition could be achieved at high deposition rates [1], much attention has been paid in order to avoid the target from poisoning and to eliminate the hysteresis effect. Several approaches have been suggested and implemented including extensive reactive gas pressure/flow control by optical emission or voltage monitoring [1,3,10], increasing the inert gas partial pressure [11], decreasing the target erosion area below a critical value [12], increasing the target to substrate distance [13], localized gas addition [8,14], increase of the pumping speed [1,8], use of substoichiometric targets instead of purely metallic targets [15] and use of a so called “baffled target”, where the target is

covered with a box having a small aperture through which the sputtered material is transferred to the substrate [16].

Although there is a vast literature on reactive MSD, only few reports can be found on the impact of the discharge power on target poisoning and hysteresis of DC reactive MSD [8,9,17]. In the case of a high power impulse magnetron sputtering (HiPIMS), however, it has been found that the increased discharge power density during the pulse-on time leads to an elimination of the hysteresis effect due to a stabilization of the transition mode [18–20]. Within this paper, we studied the target poisoning and hysteresis in DC reactive MSD of TiN as a function of the discharge power (frequently also referred to as target power). Further, we discuss the potential of overcoming the decreased deposition rate due to target poisoning by increasing the discharge power during reactive MSD as well as the possibility of depositing in the transition mode at high discharge power. In the current work, a Ti target was sputtered in a reactive Ar/N_2 atmosphere and the target voltage was measured as a function of the reactive N_2 gas flow at different discharge power levels. To investigate the influence of the discharge power on the coating properties, TiN_x ($x \leq 1$) coatings were synthesized at N_2 flows below the poisoning of the target (metallic mode) and at N_2 flows above the transition (poisoned mode). The resulting coating properties were consequently correlated with the conditions during the deposition process.

2. Experimental methods

2.1 Discharge analysis and coating deposition

In order to investigate the influence of the discharge power on target poisoning, hysteresis experiments [21] at discharge power densities ranging from 4.4 to 34 W/cm² (calculated with respect to the size of the racetrack resulting from target erosion) were performed on a lab-scale magnetron sputter deposition system, described in detail elsewhere [22,23]. The magnetron was equipped with a planar circular Ti target with a diameter of 150 mm and a purity of no less than 99.995 %. During each hysteresis experiment, the discharge was regulated on constant power and the target voltage was monitored as a function of the reactive N_2 gas flow. Starting at 0 sccm, the N_2 gas flow was gradually increased in steps of 0.5 sccm, while discharge power and Ar flow were kept constant. The Ar flow was fixed at 50 sccm, if not stated otherwise, which resulted in an Ar partial pressure of ~1.0 Pa. Applying this procedure, the poisoning of the target can be recognized by a sudden and pronounced voltage change usually occurring within a small region of reactive N_2 gas flow

[1,21,24]. After the N_2 flow was increased to a value well above the necessary flow for target poisoning, it was subsequently stepwise decreased to 0 sccm. The removal of the compound layer from the target surface at decreasing reactive N_2 gas flows is associated with a recovery of the cathode voltage to a value before target poisoning. This usually occurs at a lower reactive N_2 gas flow than during poisoning, i.e. the formation of the compound layer and, consequently, the hysteresis behavior can be investigated.

For the synthesis of the Ti and TiN_x coatings the same system was used. Prior to the deposition, a 30 min chamber baking at 400 °C and evacuation to a residual gas pressure of $2·10^{-3}$ Pa were conducted, after which the temperature of the substrate holder was reduced to the actual deposition temperature of 200 °C. A 10 min target cleaning (target current: 1.5 A, Ar flow: 15 sccm) and a 20 min substrate ion etching process (bias voltage: -1250 V, substrate current: 20 mA) were performed after which an Ar gas flow of 50 sccm was introduced to the chamber. The coatings were then synthesized at different discharge power densities from 4.4 to 34 W/cm². N_2 was added with gas flows necessary for the deposition in the desired operational mode (non-reactive as well as reactive in metallic and poisoned mode; see also Fig.2a). The deposition time was varied between 8 and 180 min in order to obtain coatings with a thickness of about 2.0 ± 0.5 µm. Single crystalline silicon wafers with a (100) orientation were used as substrates. They had a thickness of 380 µm, were cut to a size of 6.5 mm × 20.5 mm and were positioned at a distance of ~75 mm to the target. A bias voltage of -40 V was applied to the substrate holder during all deposition runs.

2.2 Coating characterization

The microstructure of the coatings was investigated by X-ray diffraction (XRD) employing a Bruker AXS D8 Advance diffractometer with Cu-K_α radiation. The specimens were measured with parallel beam optics in θ-2θ configuration within a 2θ angle range from 20 to 65° and an increment speed of 1 °/min. The resulting patterns were compared with the corresponding powder diffraction files published by the International Centre for Diffraction Data for Ti [25] and TiN [26], respectively.

The scanning electron microscope (SEM) images of the coating cross sections were recorded with a Zeiss Evo 50, which was equipped with an Oxford Instruments INCA DryCool energy dispersive X-ray (EDX) detector. This detector was used to determine the chemical composition of the coatings. A nitrogen content of less than 15 % could not be resolved by EDX due to the overlap of the titanium and nitrogen peaks in the spectrum. The coating

thickness was obtained from the secondary electron images and the deposition rate was calculated by dividing the coating thickness by the corresponding deposition time.

The room temperature residual stress of the coatings was determined by means of the substrate curvature technique using a custom-built device, described in detail elsewhere [27]. This device measures the curvature of the coated samples utilizing the reflection of two parallel laser beams, which is converted to the residual stress by the modified Stoney equation [28]. For each coating a number of four samples was investigated.

Elastic modulus as well as hardness were determined by means of nanoindentation employing a UMIS nanoindenter by Fischer-Cripps Laboratories equipped with a Berkovich diamond tip. For each coating a series of 20 measurements at different loads varying from 2 to 15 mN was conducted. The maximum load of 15 mN was chosen in order to ensure that the maximum indentation depth was below 10 % of the coating thickness in order to minimize the substrate influence. The resulting load-displacement curves were analyzed using the Oliver and Pharr method [29].

3. Results and discussion

3.1 Target poisoning and hysteresis effect

3.1.1 Influence of pumping speed and inert gas pressure

Figure 1a shows the results of three hysteresis experiments performed at different pumping speeds and Ar partial pressures at a constant discharge power density of 10 W/cm^2. The pumping speed was calculated by dividing the Ar mass flow injected into the chamber by the resulting Ar partial pressure determined with a hot-cathode ion pressure gauge without reactive N_2 gas flow. The pumping speed was varied by changing the rotation frequency of the turbomolecular pump from 1000 to 650 Hz, which resulted in pumping speeds of 83 and 50 l/s, respectively. In all three cases presented in Fig.1a, the typical hysteresis behavior can be noticed which is attributed to poisoning and de-poisoning of the target [1,8]. A comparison of the curves at the low pumping speed of 50 l/s indicates that the N_2 gas flow for transition from metallic to poisoned mode is not influenced by the Ar partial pressure. However, a clear effect on the width of the hysteresis is evident. Basically, there are two main contributions to target

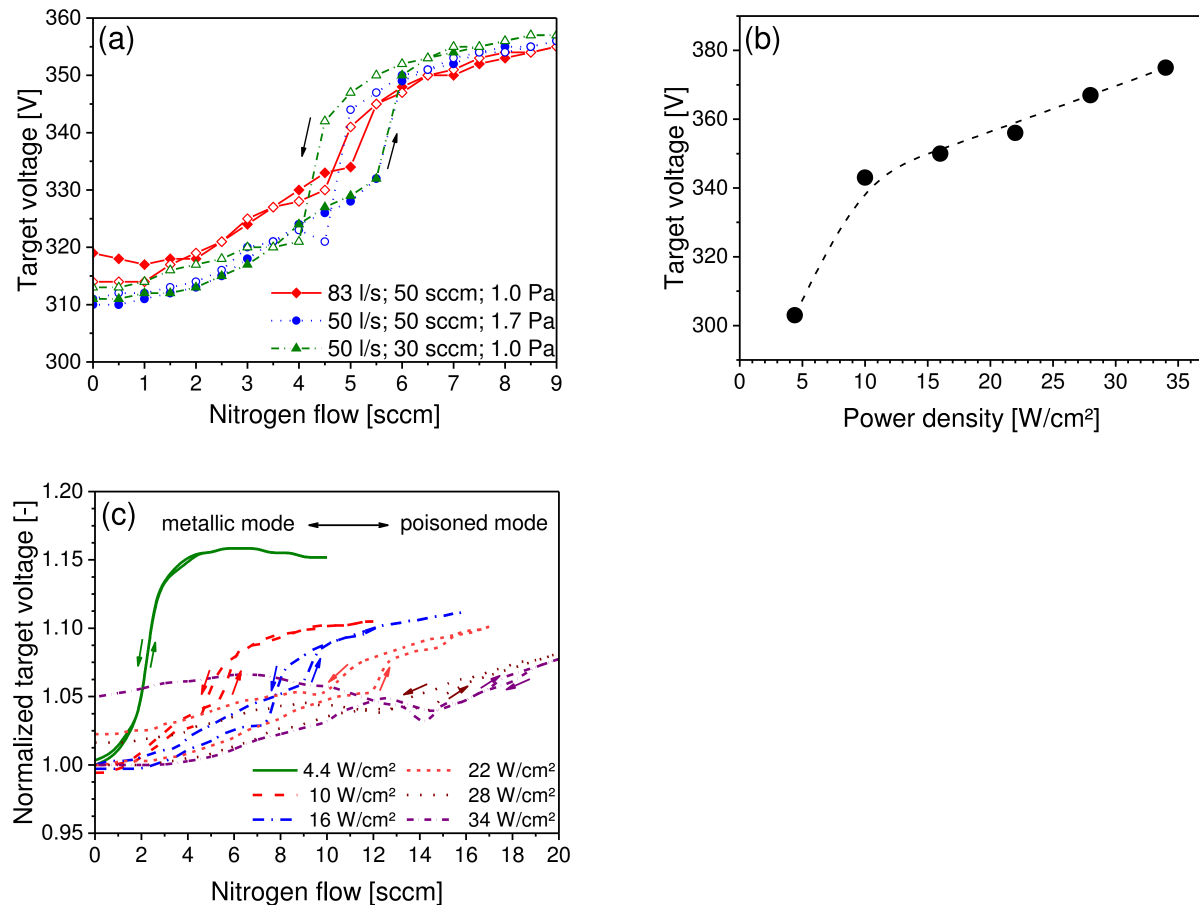

Figure 1: (a) Target voltage as a function of the N_2 gas flow at different pumping speeds (50 and 83 l/s) and pressures (Ar gas flow in sccm and partial pressure in Pa at 0 sccm N_2 flow are also given in the figure). The closed symbols refer to increasing N_2 flow, while the open symbols refer to decreasing N_2 flow. (b) Target voltage as a function of power density in non-reactive Ar atmosphere. (c) Normalized target voltage as a function of the N_2 gas flow at different power densities. The target voltage was normalized using the respective voltage values shown in (b).

poisoning, i.e. chemisorption and reactive ion implantation [8]. Chemisorption is solely dependent on the absolute reactive gas pressure which is not influenced by the Ar partial pressure. However, when the Ar partial pressure is increased, the mole fraction N_2 in the gas is reduced and the amount of nitrogen that is implanted into the target is decreased [8]. This is due to a larger amount of non-reactive Ar ions available in the plasma to remove the target surface. This lowers the concentration of ions implanted and consequently leads to the narrower hysteresis.

The effect of the pumping speed on the hysteresis width is more pronounced, as exemplified by the two curves at the same Ar partial pressure of 1.0 Pa in Fig.1a. As the pumping speed was increased by a factor of 1.7, the hysteresis width decreased to

approximately one third of its initial value. An increase of the pumping speed leads to a stabilization of the process in general as the amount of reactive gas consumed by the target material is reduced [1,8]. In order to keep the hysteresis width minimal, a pumping speed of 83 l/s was chosen for all further experiments.

3.1.2 Influence of discharge power

In order to investigate the influence of the discharge power on target poisoning, the target voltage was monitored at constant discharge powers ranging from 4.4 to 34 W/cm² while the reactive N_2 gas flow was varied during the experiments. Figure 1b displays the target voltage as a function of the discharge power without reactive gas flow, representing the starting points of the corresponding hysteresis experiments shown in Fig.1c. The curve in Fig.1b exhibits a linear relation for discharge powers exceeding 10 W/cm². Below this point, a stronger decrease in voltage can be noticed.

Figure 1c shows the results of the hysteresis experiments with normalized voltage values to facilitate a comparison between the different discharge powers. Three major influences of the discharge power density on the target poisoning could be identified. With increasing power density the voltage change due to target poisoning is shifted towards higher reactive gas flows. This can be explained by the higher amount of target material that is sputtered at higher power. The more metal atoms are transferred into the vapor phase, the greater is the resulting gas consumption [8] and, thus, a higher reactive gas flow is necessary to trigger the switching process from metallic to poisoned mode.

Further, the voltage change due to target poisoning becomes smaller with increasing discharge power. The discharge voltage as a function of the power density depends on the current-voltage characteristic of the target material. In the metallic mode, the target surface consists of titanium and has therefore a different characteristic than in the poisoned mode, where the target surface is comprised of a titanium nitride layer. Hence, the change of the discharge voltage due to target poisoning is not constant with varying discharge power. This leads to the smaller voltage difference observed at increased discharge power densities.

Finally, the discharge power density has a strong effect on the width of the hysteresis. From 4.4 to 22 W/cm² the width increases, which is consistent with the trend found in literature where the Berg model [30] predicts that the hysteresis is broadened with increasing discharge power [8,9]. However, above 22 W/cm² we found that the width of the hysteresis is strongly decreasing until it is even reversed and merely detectable at 34 W/cm², which is in contrast to the above mentioned model. Furthermore, the change of the voltage is less steep

at elevated discharge powers. A reason for both effects might be that above a certain discharge power density not the whole target surface is covered by the reaction product during poisoning at once, but that the target is poisoned gradually. This proceeds, starting from the outer margins of the target erosion zone where the current density is low, inwards [31]. The high plasma density in the center of the erosion zone is sufficient to prevent the target from poisoning, while further away from the center the target is already covered with titanium nitride. During de-poisoning with reducing reactive gas flows, the target is likewise progressively cleaned and consequently the metal/transition mode is stabilized and the hysteresis vanishes.

Other factors controlling the shape of the hysteresis are the (reactive) gas rarefaction close to the target surface [32] and reactive gas dissociation [33]. Both effects are more pronounced at high discharge power and have been found to be beneficial for avoiding the hysteresis effect in HiPIMS [18,33]. Hence, they might also play a role during reactive DCMS at high discharge power densities by stabilizing the metal/transition mode due to a decreased amount of reactive gas atoms close to the target surface, hindering the target poisoning in this way and an increased gas consumption due to a higher chemical reactivity of the gas.

3.2 Deposition rate and coating properties

3.2.1 Deposition rate

Figure 2a shows the part of the hysteresis experiments with increasing N_2 flow with open symbols marking the N_2 flows chosen for the deposition of the coatings at the respective power density. In addition to the two deposition series in metallic mode (rectangles) and in poisoned mode (circles), a deposition series in non-reactive atmosphere (pure Ar flow) was conducted.

Figure 2b shows the resulting deposition rates of the investigated coatings. It can be seen that in all cases a nearly linear relationship between deposition rate and discharge power is present. This can be explained by the fact that at an elevated discharge power the amount of sputtered material is equally increased due to a higher discharge current. As can be expected, there is a vast difference between the coatings deposited in the metallic and poisoned mode [1,2,4,34,35]. The deposition rate of the metallic-mode coatings is approximately three times higher as compared to the deposition rate of the poisoned-mode

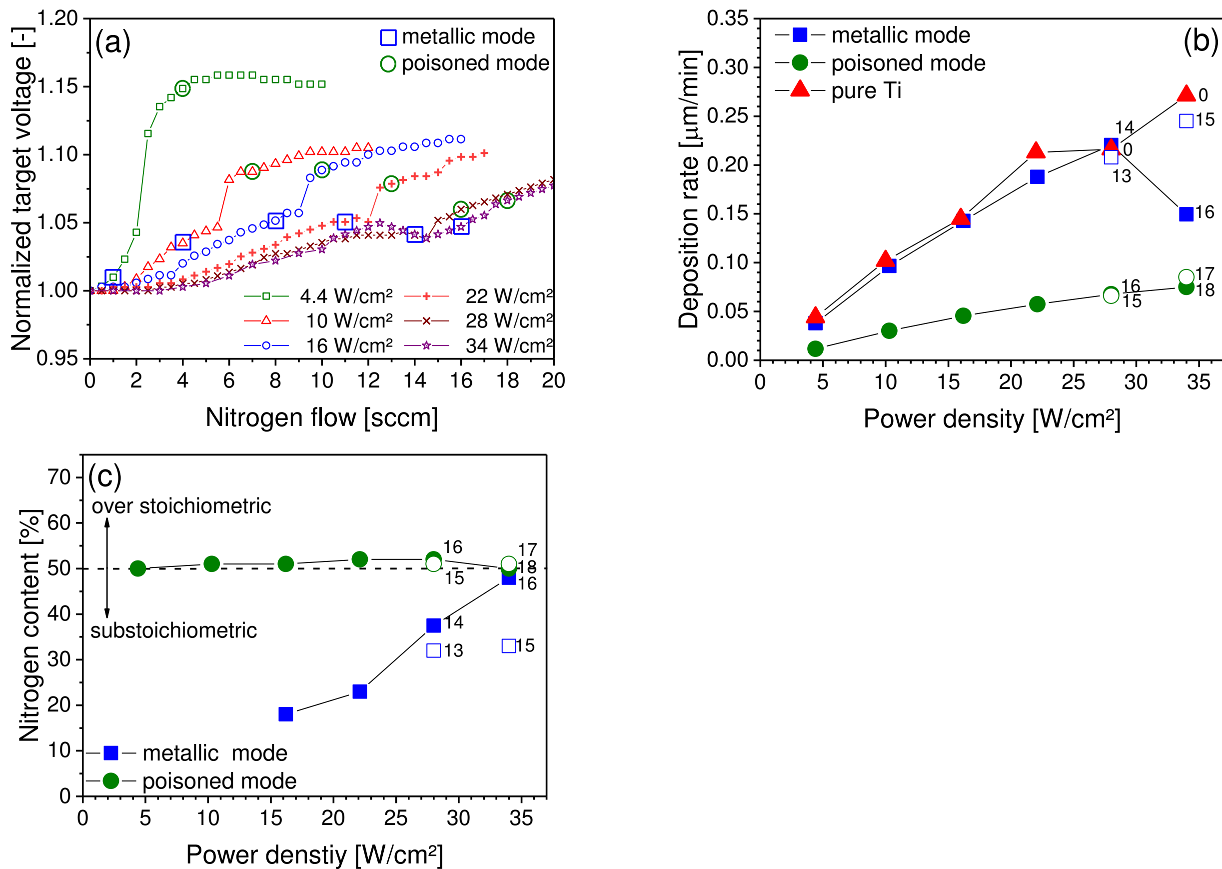

Figure 2: (a) Normalized target voltage as a function of the increasing N_2 gas flow at different power densities. The N_2 gas flows used for the depositions in metallic and poisoned mode are indicated with squares (□) and circles (○), respectively. (b) Deposition rate and (c) chemical composition of the investigated coatings. Triangles refer to coatings deposited in non-reactive atmosphere, i.e. pure Ar. Open symbols show additional depositions at discharge powers of 28 and 34 W/cm². At power densities below 16 W/cm² the nitrogen content in the coating was below the detection limit of the EDX. Additional values given at the power densities of 28 and 34 W/cm² in (b) and (c) refer to the nitrogen mass flow in sccm used for the respective depositions.

coatings. It can further be seen that as long as no target poisoning takes place, the added N_2 does not influence the deposition rate since there is no difference evident between the metallic-mode TiN_x coatings and non-reactive Ti coatings. Furthermore, additional coatings grown at the two highest discharge powers of 28 and 34 W/cm² at intermediate N_2 flows included in Fig.2b (open symbols) suggest that there is a clear transition between metallic and poisoned mode, as the additional coatings can clearly be referred to as either metallic or poisoned mode. Only at a N_2 flow of 16 sccm and a discharge power of 34 W/cm² an intermediate deposition rate was obtained. This can be understood by the instability of the

process in this N_2 flow and power density region, i.e. in the transition regime between the metallic and poisoned deposition mode.

3.2.2 Chemical composition

The chemical composition of the coatings as determined by EDX is displayed in Fig.2c. The TiN_x coatings deposited in the poisoned mode exhibit a stoichiometric composition throughout the whole power range which is in agreement with literature [35]. In contrast, in the case of the metallic-mode TiN_x coatings a clear trend is visible as the nitrogen content in the coatings increases with rising discharge power. This is due to a stabilization of the process with increasing power. At a higher power the deposition run can be performed at a N_2 gas flow value that is, in relative terms, closer to the transition to the poisoned mode. Consequently, the nitrogen content in the coating is increased and thus deposition of a coating with almost stoichiometric composition at the comparatively high deposition rate of 0.15 µm/min is possible, which corresponds to approximately 200 % of the deposition rate in poisoned mode.

3.2.3 Microstructure

Figure 3 displays the X-ray diffractograms of all deposited TiN_x coatings which exhibit a crystalline structure regardless of the deposition mode. In the case of the metallic deposition mode (Fig.3a), a gradual transition from hexagonal Ti at the lowest power density to face-centered cubic (fcc) TiN at the highest power density is evident. This change in structure is caused by the higher amount of nitrogen that is incorporated into the coating due to the increased fraction of N_2 in the sputtering atmosphere at elevated power. The incorporated nitrogen leads to a distortion of the Ti lattice which is more pronounced at increased nitrogen contents [36]. Thus, the (002) and the (101) peaks characteristic for hexagonal Ti are gradually shifted towards the (111) and (200) peaks of fcc-TiN. In the case of a stoichiometric TiN coating at the highest power density, the structure eventually corresponds to fcc-TiN. No indication for the occurrence of a substoichiometric Ti_2N [37] phase could be found in the diffractograms. In addition, a peak broadening is detectable with increasing discharge power which indicates a grain refinement [38] with increasing power and nitrogen content.

The X-ray diffractograms of the coatings deposited in the poisoned mode (see Fig.3b) all indicate that the coatings are comprised of fcc-TiN. However, a change of the preferred orientation is detectable. At the lowest discharge power, a (111) orientation of the coherently diffracting domains can be noticed, whereas with increasing power the preferred orientation changes gradually towards a (100) orientation. A similar trend was reported by Sproul et al.

who found a strong (111) orientation at low power density, changing towards a more random orientation with increasing power [39]. This trend was attributed to a more pronounced surface mobility at higher power densities as a result of increased ion bombardment. Similarly, Mahieu et al. found a change in orientation from (111) to (100) with increasing N_2 partial pressure due to an increased surface mobility at higher partial pressures [40]. As the N_2 gas flow is simultaneously increased with increasing deposition power in our work, this effect is assumed to contribute as well. Besides the change of the orientation, the peaks in Fig.3 are shifted to lower diffraction angles, which is also in agreement with the results found by Sproul et al. [39]. This peak shift is more pronounced at the higher discharge powers indicating that the stress in the coatings increases with rising deposition power.

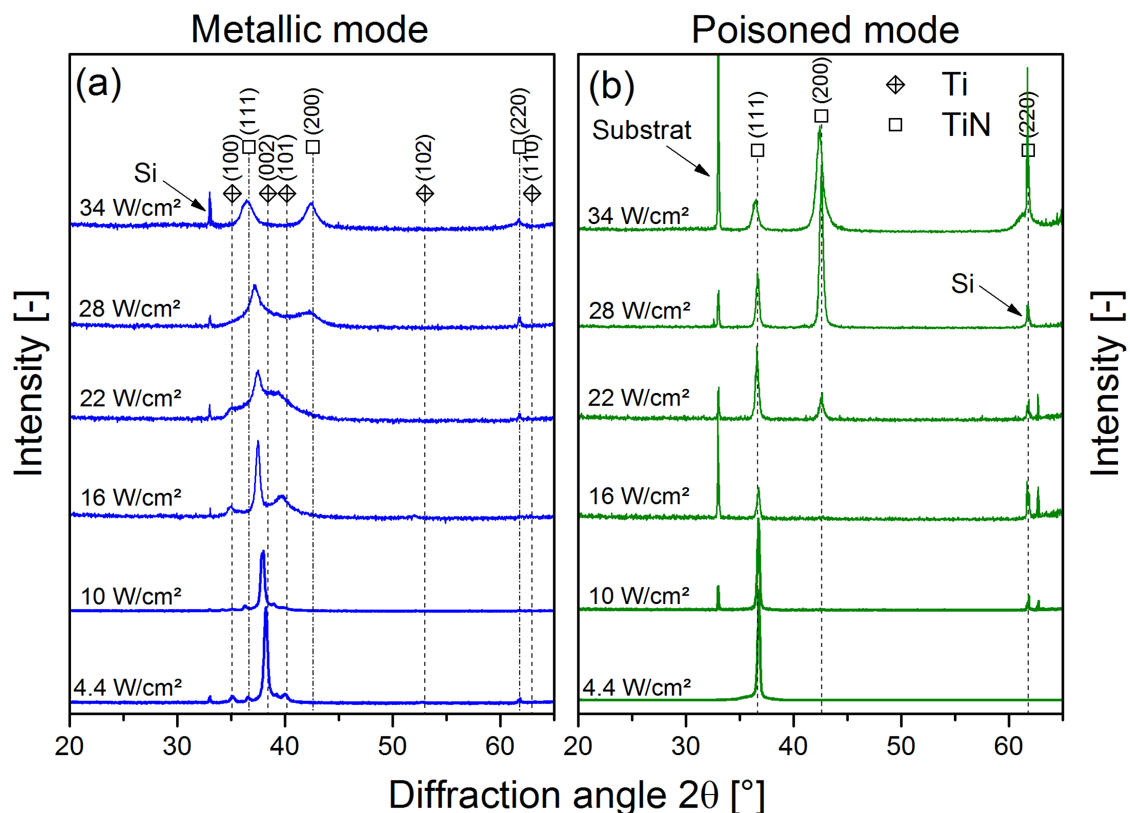

Figure 3: X-ray diffractograms of the investigated TiN_x coatings on Si substrates deposited in (a) metallic mode and (b) poisoned mode. The positions of the standard peaks for hexagonal Ti and fcc-TiN are indicated according to the respective ICDD powder diffraction file [25,26].

In the same way as for the coatings deposited in the metallic mode, a peak broadening is visible for the XRD patterns of the poisoned-mode coatings. One reason for this peak broadening at higher discharge power can be, as already mentioned, grain refinement [38]. This interpretation is confirmed by the SEM micrographs shown in Fig.4 for both deposition

modes. While the fracture cross section of the metallic mode coating at the lowest power density shows a columnar structure, the cross section derived at the highest discharge power appears featureless without discrete grains detectable (Fig.4a). A less pronounced grain refinement with increasing discharge power is visible for the coatings deposited in the poisoned mode as shown in Fig.4b. In this case, the columnar structure is preserved even at the maximum power density of 34 W/cm² applied in this work. This is in concordance with Sundgren [37], who noted that increasing the deposition rate leads to a decreased diameter of the columns in TiN coatings. Nevertheless, all coatings appear dense in the SEM micrographs and exhibit a smooth surface without pronounced asperities.

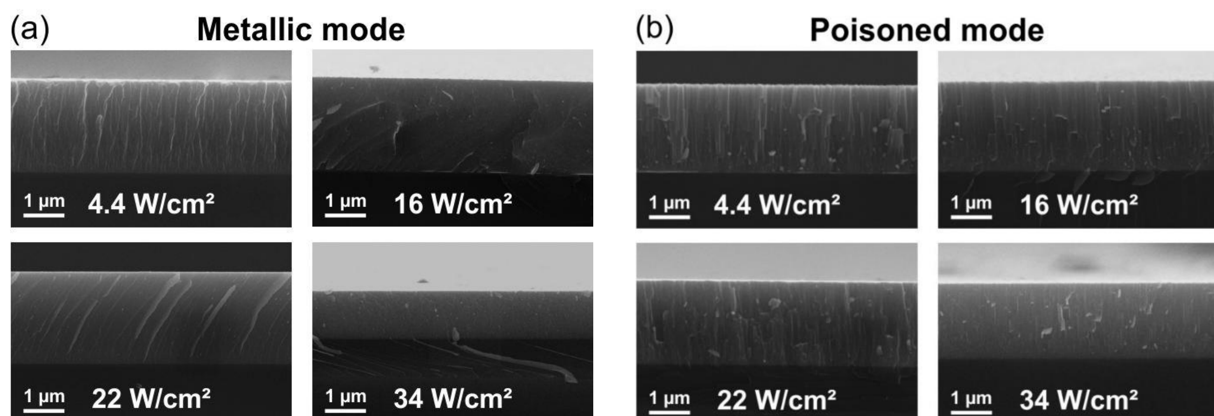

Figure 4: SEM micrographs of the fracture cross sections of coatings deposited on Si substrates in (a) metallic mode and (b) poisoned mode at different discharge power densities.

3.2.4 Mechanical properties

Figure 5a illustrates the residual stress at room temperature as a function of the power density and deposition mode. For both deposition modes, an increase of the compressive stress with increasing discharge power is evident, but the metallic-mode coatings show in general higher compressive stress values. The increase in stress in the poisoned-mode coatings is shifted to higher power density values, where below 28 W/cm² the stress is almost constant. These results can be explained by the fact that the stresses are strongly affected by the deposition rate [6,41]. When the deposition rate is high, the time for thermally activated atom movements on the surface of the growing film is low, i.e. if the deposition rate exceeds a certain threshold value, then the defects generated during deposition cannot be annealed out anymore which results in high stress values [6]. As the deposition rate of the metallic-mode coatings is approximately three times the value of the poisoned-mode coatings at

constant deposition temperature, the critical deposition rate to trigger the increase in stress is reached at a lower power density in metallic than in poisoned mode.

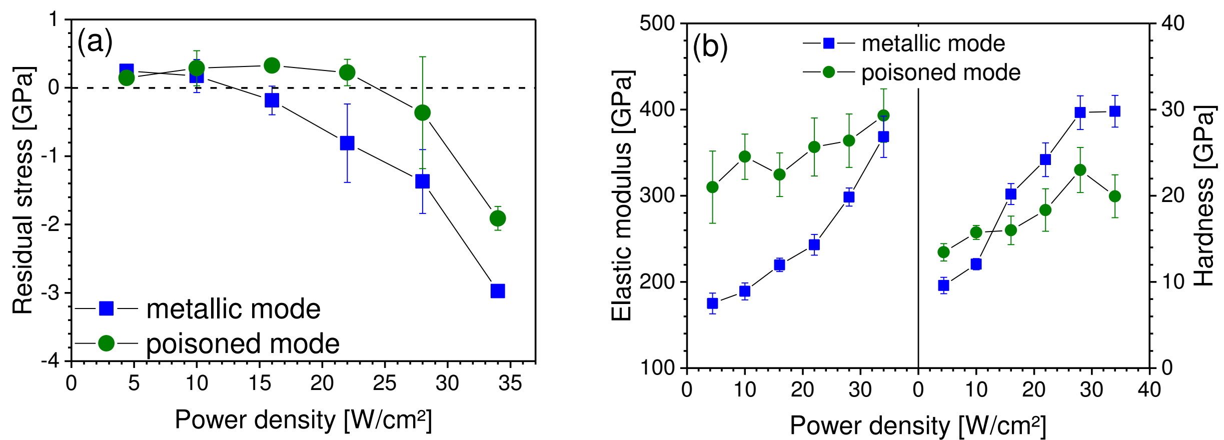

Figure 5: (a) Room temperature residual stress and (b) elastic modulus and hardness of the deposited TiN_x coatings.

The elastic modulus and hardness of the investigated coatings as determined by nanoindentation versus the applied power density can be seen in Fig.5b. An increase of both hardness and elastic modulus can be observed which is more pronounced for the metallic-mode coatings. The increase of the elastic modulus in the case of the metallic-mode coatings is mainly owing to the change in chemical composition and microstructure of the coatings with increasing discharge power (see Figs.2c and 3). At the lowest power density the elastic modulus is low at roughly 175 GPa, which is about 55 GPa above the literature value of metallic Ti [42]. With increasing nitrogen content in the coating at higher discharge power, the elastic modulus increases until at 34 W/cm² it reaches a value that is similar to the elastic modulus of TiN coatings. In the case of the poisoned-mode coatings, the increase of the elastic modulus is less pronounced as the chemical composition remained constant with varying power density. The increase of the modulus can be correlated with the change of the preferred orientation from (111) at the lowest power density towards (100) at the highest power density, since the elastic modulus of TiN in the (100) direction is higher than in the (111) direction [43].

Similar to the elastic modulus, the hardness is increasing as well with increasing power density. Again, this trend is more prominent for the metallic mode coatings. The hardness of the metallic mode coatings is about 10 GPa at the lowest power density, but it increases when the power density is raised and exceeds the values obtained for the stoichiometric poisoned-mode coatings at power densities larger than 10 W/cm². This strong change in hardness in the case of the metallic deposition mode can be attributed to various effects: (i) higher nitrogen

contents result in higher hardness values in the case of substoichiometric TiN_x coatings [34,37], (ii) elevating the deposition rate minimizes the time for the formation of equilibrium structures and a distortion of the lattice is the consequence, leading to a higher hardness [6,37], (iii) as can be seen from the SEM cross sections, the grains are refined at high deposition rates, resulting in higher hardness according to the Hall-Petch effect [6,44] and (iv) the metallic-mode coatings deposited at high deposition power are under a strong compressive stress state which is known to increase the hardness of coatings [44,45].

The hardness evolution with increasing discharge power of the coatings deposited in the poisoned mode can be explained in a similar way. Both, the grain refinement and the increase of the compressive stress lead to a higher hardness. In this case, however, grain refinement and increase in stress are less pronounced than in the case of the metallic-mode coatings. In addition, the composition remains constant with changing power density, which is one of the major reasons for the hardness increase of the coatings deposited in the metallic mode. As a result, the hardness increase of the poisoned-mode coatings is less pronounced. The observed change of the preferred orientation in the poisoned-mode coatings appears to be without influence on the hardness. Chou et al. [46] reported an increased hardness at a preferred (111) orientation, but Sproul et al. [39] found for TiN coatings that a change of the preferred orientation with higher discharge power from (111) towards a more random orientation is accompanied by an increase in stress which is typically associated with an increase in hardness. Due to the fact that the overall change of the mechanical properties of the poisoned-mode TiN_x coatings is small, the influence of the preferred orientation can be considered to be a minor one.

4. Conclusions

Within this work, the effect of the discharge power density on the reactive direct current magnetron sputtering of titanium in N_2 containing atmosphere was investigated. Target poisoning effects were studied at different discharge powers ranging from 4.4 to 34 W/cm² by means of hysteresis experiments. Upon an increase of the discharge power, the target poisoning is shifted towards higher N_2 gas flows in the sputtering gas and the width of the hysteresis is minimized. This enables the deposition of TiN_x coatings with high nitrogen contents in the metallic/transition mode. By increasing the discharge power it was possible to deposit a close-to-stoichiometric TiN_x coating at a high deposition rate of 0.15 µm/min, which was found to be 200 % of the respective deposition rate in poisoned mode. Elevating the discharge power can therefore be used as an approach to reduce the detrimental influences

of target poisoning and hysteresis effect during reactive sputter deposition of stoichiometric TiN_x, while enabling high deposition rates.

The properties of the synthesized TiN_x coatings are also strongly affected by the change in discharge power. Elastic modulus and hardness increased with power density regardless of the deposition mode, i.e. metallic or poisoned mode. This was mainly attributed to the elevated deposition rate impeding defect annihilation, which results in grain refinement and higher compressive stress states and, hence, in improved mechanical properties. The increased nitrogen content in the metallic-mode deposited TiN_x also contributed to the enhancement of hardness and elastic modulus.

5. Acknowledgements

This work was financially supported by the Austrian Federal Government (in particular from Bundesministerium für Verkehr, Innovation und Technologie and Bundesministerium für Wissenschaft, Forschung und Wirtschaft) represented by the Österreichische Forschungsförderungsgesellschaft mbH within the project SmartCoat - Eco (project number 843621).

6. References

[1] I. Safi, Surf. Coat. Technol. 127 (2000) 203–218.
[2] J. Musil, P. Baroch, J. Vlček, K.H. Nam, J.G. Han, Thin Solid Films 475 (2005) 208–218.
[3] W.D. Sproul, Vacuum 51 (1998) 641–646.
[4] S. Schiller, U. Heisig, C. Korndörfer, G. Beister, J. Reschke, K. Steinfelder, J. Strümpfel, Surf. Coat. Technol. 33 (1987) 405–423.
[5] M. Wittmer, J. Vac. Sci. Technol. A 3 (1985) 1797.
[6] M. Ohring, The Materials Science of Thin Films, Academic Press (1991) San Diego, USA.
[7] F.C. Stedile, J. Vac. Sci. Technol. A 10 (1992) 3272.
[8] D. Depla, Magnetrons, Reactive Gases and Sputtering, 3rd ed., Diederick Depla (2014) Ghent.
[9] S. Berg, T. Nyberg, Thin Solid Films 476 (2005) 215–230.
[10] W.D. Sproul, D.J. Christie, D.C. Carter, Thin Solid Films 491 (2005) 1–17.
[11] E. Särhammar, K. Strijckmans, T. Nyberg, S. van Steenberge, S. Berg, D. Depla, Surf. Coat. Technol. 232 (2013) 357–361.
[12] T. Nyberg, S. Berg, U. Helmersson, K. Hartig, Appl. Phys. Lett. 86 (2005) 164106.

[13] S. Schiller, G. Beister, W. Sieber, Thin Solid Films 111 (1984) 259–268.
[14] D. Depla, J. Haemers, R. de Gryse, Surf. Coat. Technol. 235 (2013) 62–67.
[15] H. Ohsaki, Y. Tachibana, A. Hayashi, A. Mitsui, Y. Hayashi, Thin Solid Films 351 (1999) 57–60.
[16] F. Engelmark, J. Westlinder, T. Nyberg, S. Berg, J. Vac. Sci. Technol. A 21 (2003) 1981.
[17] S. Berg, J. Vac. Sci. Technol. A 4 (1986) 594.
[18] J.T. Gudmundsson, N. Brenning, D. Lundin, U. Helmersson, J. Vac. Sci. Technol. A 30 (2012) 30801.
[19] E. Wallin, U. Helmersson, Thin Solid Films 516 (2008) 6398–6401.
[20] M. Aiempanakit, T. Kubart, P. Larsson, K. Sarakinos, J. Jensen, U. Helmersson, Thin Solid Films 519 (2011) 7779–7784.
[21] D. Depla, A. Colpaert, K. Eufinger, A. Segers, J. Haemers, R. de Gryse, Vacuum 66 (2002) 9–17.
[22] S. Grasser, R. Daniel, C. Mitterer, Surf. Coat. Technol. 206 (2012) 4666–4671.
[23] P. Losbichler, C. Mitterer, P.N. Gibson, W. Gissler, F. Hofer, P. Warbichler, Surf. Coat. Technol. 94-95 (1997) 297–302.
[24] I. Petrov, A. Myers, J.E. Greene, J.R. Abelson, J. Vac. Sci. Technol. A 12 (1994) 2846.
[25] Powder diffraction file 00-044-1294, International Center for Diffraction Data, PDF-2/Release, 2007.
[26] Powder diffraction file 00-038-1420, International Center for Diffraction Data, PDF-2/Release, 2007.
[27] C. Saringer, M. Tkadletz, C. Mitterer, Surf. Coat. Technol. 274 (2015) 68–75.
[28] G. Janssen, M.M. Abdalla, F. van Keulen, B.R. Pujada, B. van Venrooy, Thin Solid Films 517 (2009) 1858–1867.
[29] W.C. Oliver, G.M. Pharr, J. Mater. Res. 7 (1992) 1564–1583.
[30] S. Berg, H.-O. Blom, T. Larsson, C. Nender, J. Vac. Sci. Technol. A 5 (1987) 202.
[31] S. Schiller, U. Heisig, K. Goedicke, K. Schade, G. Teschner, J. Henneberger, Thin Solid Films 64 (1979) 455–467.
[32] S.M. Rossnagel, J. Vac. Sci. Technol. A 6 (1988) 19.
[33] S. Konstantinidis, R. Snyders, Eur. Phys. J. Appl. Phys. 56 (2011) 24002.
[34] F. Elstner, A. Ehrlich, H. Giegengack, H. Kupfer, F. Richter, J. Vac. Sci. Technol. A 12 (1994) 476.
[35] J.-E. Sundgren, B.-O. Johansson, S.-E. Karlsson, Thin Solid Films 105 (1983) 353–366.
[36] B. Holmberg, M. Yhland, R. Dahlbom, J. Sjövall, O. Theander, H. Flood, Acta Chem. Scand. 16 (1962) 1255–1261.

[37] J.-E. Sundgren, Thin Solid Films 128 (1985) 21–44.

[38] M. Birkholz, Thin Film Analysis by X-Ray Scattering, Wiley-VCH (2006) Weinheim, Germany.

[39] W.D. Sproul, P.J. Rudnik, C.A. Gogol, Thin Solid Films 171 (1989) 171–181.

[40] S. Mahieu, P. Ghekiere, D. Depla, R. de Gryse, Thin Solid Films 515 (2006) 1229–1249.

[41] A.J. Perry, M. Jagner, W.D. Sproul, P.J. Rudnik, Surf. Coat. Technol. 39-40 (1989) 387–395.

[42] M. Spittel, T. Spittel, in: W. Martienssen, H. Warlimont (Eds.), Materials, Springer (2002) Berlin, London, pp. 77–80.

[43] J.O. Kim, J.D. Achenbach, P.B. Mirkarimi, M. Shinn, S.A. Barnett, J. Appl. Phys. 72 (1992) 1805.

[44] P.H. Mayrhofer, C. Mitterer, L. Hultman, H. Clemens, Prog. Mater. Sci. 51 (2006) 1032–1114.

[45] P.H. Mayrhofer, C. Mitterer, J. Musil, Surf. Coat. Technol. 174-175 (2003) 725–731.

[46] W.-J. Chou, G.-P. Yu, J.-H. Huang, Surf. Coat. Technol. 149 (2002) 7–13.

Publication III

Influence of discharge power and bias potential on microstructure and hardness of sputtered a-C coatings

Christian Saringer, Christoph Oberroither, Katrin Zorn, Robert Franz, Christian Mitterer

Submitted for publication to the Journal of Vacuum Science and Technology A

Influence of discharge power and bias potential on microstructure and hardness of sputtered a-C coatings

Christian Saringer[a,*], Christoph Oberroither[a], Katrin Zorn[b], Robert Franz[a], Christian Mitterer[a]

[a] Department of Physical Metallurgy and Materials Testing, Montanuniversität Leoben, Franz-Josef-Strasse 18, 8700 Leoben, Austria

[b] MIBA High Tech Coatings, Dr.-Mitterbauer-Strasse 3, 4655 Vorchdorf, Austria

Abstract

This work reports on the influence of the power density and bias potential on the structure-property relations of sputter deposited amorphous carbon coatings. Coatings were deposited at power densities between 4.4 and 28 W/cm² in both Ar and Ne atmospheres at pressures of 1 and 1.25 Pa, respectively. Measurements of the substrate temperature during deposition indicate that the coating is subjected to a substantial thermal load during deposition, which leads to growth of the graphitic clusters at higher power densities. This change of the microstructure results in a drop of the hardness of up to 40 % when the power density increased to 28 W/cm². A high hardness of up to 30 GPa, however, can be achieved when either a bias potential of -100 V is applied or when Ne instead of Ar is used as process gas. This can be attributed to the high compressive stresses present as a result of an enhanced ion bombardment.

1. Introduction

The term amorphous carbon (a-C) comprises a versatile class of thin film materials [1,2]. Owing to the different types of bonding occurring in carbon, a-C can have a broad variety of properties ranging from a graphite-like to a diamond-like character [3,4]. When the amount

* Corresponding author:
E-mail address: christian.saringer@unileoben.ac.at
Tel.: +43/3842 402 4239
Fax: +43/3842 402 4202

of diamond-like sp^3 bonding is high, a high hardness, density and large band gap is achieved, while predominately sp^2-bonded a-C shows a low band gap at moderate hardness and low density [1]. By adjusting the ratio of these two types of bonding, the properties can be continuously controlled over a large range. Furthermore, a-C coatings are biocompatible [5]. Due to this variety of properties, different a-C variants are used today as protective and tribological coatings [6–8] and thin films for optical [9] and medical applications [5,7].

Magnetron sputtering is one of the most widely employed technologies for the deposition of a-C [2] and many studies report on sputter deposition of a-C from graphite targets [10–15]. This technology offers the possibility of independently adjusting numerous process parameters like pressure [14], temperature [16] and ion bombardment [17], which allows for a simultaneous adjustment of the coating properties. However, the maximum sp^3-content that can be achieved with magnetron sputtering is usually small compared to cathodic arc evaporation or chemical vapor deposition, for instance [1,18]. This results in a graphite-like character and consequently in a comparatively low hardness of sputtered a-C coatings. Furthermore, the deposition rate is quite low and only a few ten nm/min are reported for sputter deposition [19–22]. In order to be able to cost-effectively deposit a-C coatings in industry, however, an elevated deposition rate is necessary. This can in principle be achieved by raising the deposition power delivered to the target. However, the microstructure of a-C strongly depends on the temperature present during film growth, where an elevated temperature leads to graphitization for sputtered and arc evaporated coatings [16,23,24]. This graphitization results in an undesired change of the structural and mechanical properties. Since the substrate temperature strongly depends on the power delivered to the system, a change of the structure and consequently the properties can be expected when the discharge power is raised.

In order to assess the influence of the discharge power on the resulting coating properties, we therefore deposited a-C films at different target power densities between 4.4 and 28 W/cm² employing an unbalanced dc magnetron sputtering system. Two different process gasses, i.e. Ar and Ne, were used for the deposition. Furthermore, various bias potentials between floating potential and -100 V were applied. During the deposition process, the substrate temperature was monitored by a thermocouple to qualitatively estimate the thermal load as a function of the process parameters and, consequently, its influence on film morphology and properties. The chemical composition and microstructure were investigated by elastic recoil detection analysis and Raman spectroscopy, respectively. The characterization of the mechanical properties by nanoindentation finally allowed to establish the scientific

chain between synthesis conditions, microstructure and properties of a-C films grown at high growth rates.

2. Experimental methods

2.1 Coating deposition

All coatings investigated within this work were deposited using a lab-scale unbalanced d.c. magnetron sputtering system which is described in detail elsewhere [25]. The magnetron was equipped with a graphite target (FHR, Germany), which consisted of a 6 mm thick carbon disc (purity ≥ 99.99 %) with a diameter of 150 mm bonded onto a 4 mm Mo backing plate using a Sn solder. Coatings were deposited in Ar and Ne atmospheres at discharge powers ranging from 531 to 3358 W, which resulted in power densities between 4.4 and 28 W/cm². These power densities were calculated by dividing the applied discharge powers by the area of target erosion (∼120 cm²). The deposition time was varied in accordance with the power density between 30 and 188 min to obtain a coating thickness of around 2 µm for all samples. Coating runs over the full power density range were performed for Ar and Ne at floating potential (determined as the potential between substrate holder and grounded deposition chamber, approximately -25 and -60 V for Ar and Ne, respectively) and for Ar at a bias of -50 V. To assess the influence of the bias voltage on the coating properties, additional coatings were deposited in Ar at bias potentials of -68 and -100 V at a single power density of 10 W/cm^2. The gas flows during the depositions were set to 50 and 68 sccm for the depositions in Ar and Ne, which resulted in pressures of 1 and 1.25 Pa, respectively. Single crystalline silicon (100) wafers with a thickness of 380 µm and a size of 20 mm × 7 mm were used as substrates, positioned at a distance of 75 mm from the target surface. No substrate heating other than the heating originating from the plasma was applied to the substrate. The substrate temperature during the deposition was monitored by an electrically insulated K-type thermocouple, which was screwed onto a steel sample positioned in the vicinity of the silicon strips. Prior to deposition, the chamber was evacuated down to a base pressure of 2×10^{-3} Pa. Furthermore, a 10 min target conditioning procedure (Ar flow: 15 sccm and target current: 0.15 A) as well as a 30 min substrate etching (bias voltage -1250 V and substrate current 20 mA) to improve the coating adhesion were performed. In the case of the depositions in Ne and at high bias potentials (-68 and -100 V) in Ar, however, the coating adhesion was nonetheless insufficient. Therefore, a carbon base layer grown in a 1 Pa Ar atmosphere at floating potential was initially deposited before switching to Ne as process gas or before

applying the bias voltage. The deposition time for the base layer was 1/8 of the total deposition time, which resulted in a thickness of the base layer of 400 ± 100 nm.

In order to calculate the sputter yields for ion bombardment of the target and for the re-sputtering of the growing coating at the substrate holder, Monte Carlo simulations were carried out. For this purpose the software package SRIM 2013 [26] was used. In order to obtain reasonable statistics, the yields were calculated using 10^5 bombarding ions.

2.2 Coating characterization

The cross-sectional images of the coatings were recorded employing a Zeiss Evo 50 scanning electron microscope (SEM). These images were also used to determine the total thickness of the coatings and the carbon sublayers, which were needed to calculate the deposition rate by dividing the obtained coating thicknesses by the corresponding deposition times.

The chemical composition of the coatings was analyzed by elastic recoil detection analysis (ERDA). The measurements and analyses were performed at the Helmholtz Zentrum Dresden Rossendorf, Germany. The probing beam was a $^{35}Cl^{7+}$ ion beam with an energy of 43 MeV and the probed area was 1.5 mm × 1.5 mm. The Bragg Ionization Chamber for the detection of the recoiled sample atoms was positioned at a scattering angle of 31°.

The microstructure of the a-C coatings was investigated by Raman spectroscopy. Spectra were recorded for each deposited coating at Raman shifts between 500 and 2200 cm^{-1} using a Jobin Yvon LabRamspectrometer equipped with a Nd-YAG laser (wavelength: 532 nm). The resulting spectra were fitted by a single Gaussian function for the peak situated near 1350 cm^{-1} (referred to as D-peak) and a single Breit-Wigner-Fano (BWF) function for the peak at 1580 cm^{-1} (referred to as G-peak) [27]:

$$I_{BWF}(x) = \frac{I_0[1+2(x-x_0)/Q\Gamma]}{1+[2(x-x_0)/\Gamma^2]}. \quad (1)$$

Here, $I_{BWF}(x)$ is the intensity of the peak as a function of the Raman shift x, x_0 is the peak position, I_0 is the peak intensity, Q is the skewness of the peak, and Γ is the full width at half maximum. The position of the peak maximum x_{max}, is then given by [27]

$$x_{max} = x_0 + \frac{\Gamma}{2Q}. \quad (2)$$

The D and the G peaks correspond to the breathing mode of carbon hexagons and stretching of C-C bonds, respectively [1,27]. The resulting peak intensities and positions were used to qualitatively assess the microstructure and to estimate the amount of sp^3 bonding according to the three stage model [27].

The overall residual stress at room temperature was determined by the wafer curvature technique employing a custom-built measurement apparatus [28]. This device uses the reflection of two parallel laser beams to determine the curvature of the substrate-coating composite resulting from the stresses present in the coating. The residual stress was then calculated from the measured curvature using the modified Stoney equation [29].

An Ultra Micro Indentation System from Fischer-Cripps laboratories equipped with a Berkovich diamond tip was employed to determine the coating hardness. Plateau tests at 20 different loads decreasing from 15 to 5 mN in steps of 0.5 mN were carried out for each coating. The resulting curves were analyzed using the Oliver and Pharr method [30]. In order to avoid any influence of the substrate, the maximum indentation depth was chosen to be smaller than 10 % of the coating thickness.

3. Results and discussion

3.1 Discharge and deposition

Figure 1a shows the influence of the target power density on the discharge voltage for studied discharges. In general, the discharge voltage increases with power density. However, the values for Ne are much less affected by the power than those obtained for Ar, and above 10 W/cm² they are approximately constant. Furthermore, the values in Ne atmosphere are considerably lower (-400 to -450 V) compared to the values in Ar atmosphere (-550 to -650 V). This can be explained by the higher secondary electron emission coefficient in the case of Ne ions bombarding C [31,32]. Also, the pressure is with 1.25 Pa higher in the case of Ne compared to Ar, which favors a lower discharge voltage [31]. Apparently, applying a bias voltage does not have any significant effect on the discharge voltage, since both curves in Fig.1a recorded for Ar are practically congruent.

The influence of the discharge power and bias potential on the substrate ion current is presented in Fig.1b. The substrate ion current was determined as the current supplied by the bias voltage generator. It is assumed that all electrons originating from the plasma are repelled by the negative bias potential and that secondary electron emission at the substrate is

negligible. Since the ion and electron currents sum up to zero in the case of an electrically insulated substrate without bias potential, i.e. in case of a floating substrate, no curves for the Ar and Ne discharges at floating potential are shown in this graph. The substrate ion current is obviously linearly increasing with power density. This is due to the fact that at higher power densities, and therefore also higher target currents, the plasma density is increased [33].

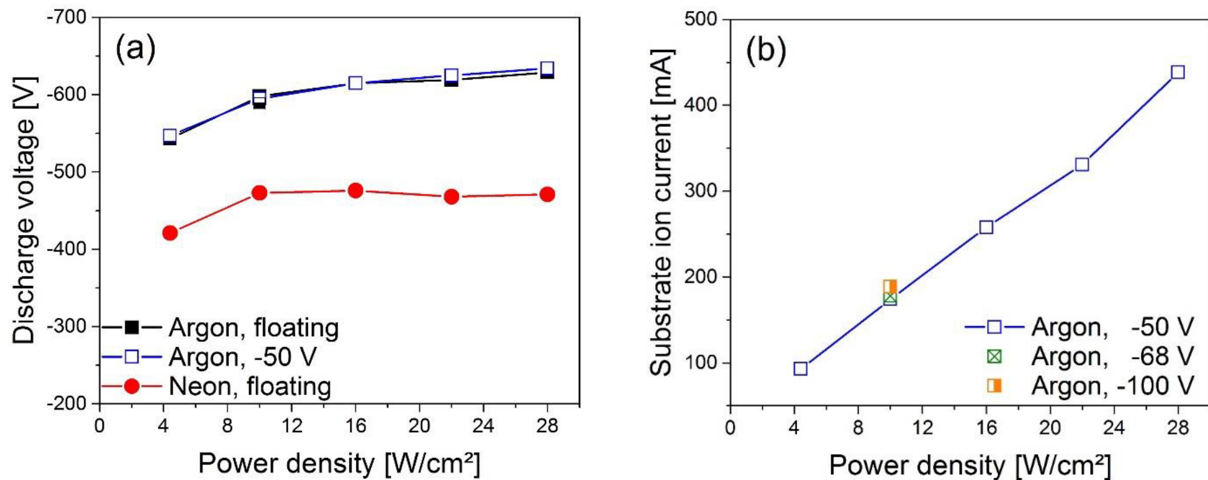

Figure 1: (a) Discharge voltage as a function of the power density for the coatings deposited in Ar at floating potential and at a bias potential of -50 V and for the coatings deposited in Ne at floating potential. (b) Substrate ion current as a function of power density and bias potential for the coatings deposited in Ar.

Hence, more ions are present in the plasma which can be attracted by the bias potential, consequently increasing the number of ions arriving at the substrate holder. Raising the bias potential on the other hand only leads to a minor increase of the substrate ion current. However, the attracted ions gain a higher kinetic energy due to the increasing potential difference between plasma and substrate when the bias is raised.

Figure 2 displays the substrate temperature as a function of the deposition time for different depositions in Ar and Ne at floating potential and in Ar at a power density of 10 W/cm² at different values of the bias potential. In all cases, the substrate temperature is increasing during deposition as a result of bombardment with energetic particles originating from the plasma [21,34]. The graphs show that the thermal load of the coating during deposition strongly depends on power density, process gas and the applied bias potential. In general, the higher the power density, the more pronounced is the increase of the substrate temperature [35]. This is evident in Figs.2a and 2b for both gases, Ar and Ne. Furthermore, at the end of the deposition process the substrate temperature is considerably higher at

elevated power densities. As a result, the temperature over the coating thickness is not constant for the different power densities and the coatings deposited at elevated power densities experience in total a higher thermal load.

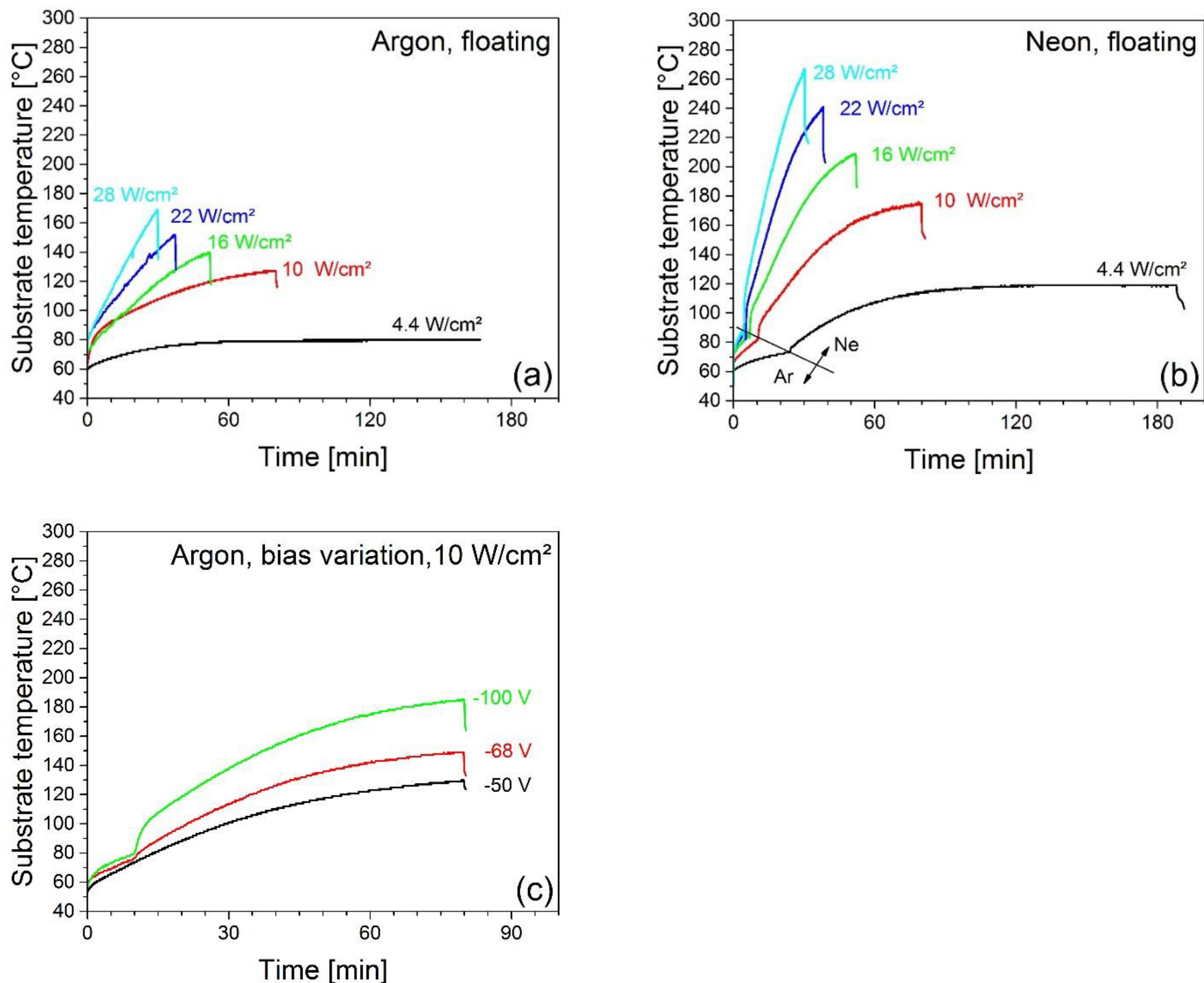

Figure 2: Substrate temperature as a function of the deposition time at various power densities for the coatings deposited in Ar (a) and Ne (b) at floating substrate and in Ar at a power density of 10 W/cm² at different bias potentials (c).

A comparison of the two gases presented in Figs.2a and 2b, leads to the conclusion that the thermal load for the depositions in Ne is considerably higher compared to Ar. While the maximum temperature at the maximum power density is only 170 °C in the case of Ar, the substrate temperature is around 270 °C at the same power density for Ne. The same effect can also be recognized from the pronounced change in heating rate when the gas is switched from Ar to Ne (Fig.2b) at the end of the base layer deposition. The most important reason for the more pronounced thermal load during the deposition with Ne is its higher thermal conductivity compared to Ar. The thermal conductivity of Ne at these low pressures is more

than twice as high as the one of Ar [36]. Furthermore, the pressure is slightly higher in the case of Ne, which also contributes to a higher thermal conductivity [36]. Thus, the energy that is put into the system at the target is more effectively transported to the substrate in the case of the deposition processes in Ne. Another contribution to the higher thermal load in Ne could stem from the higher floating potential (approximately -60 V) compared to Ar (around -25 V). Due to the larger floating potential, the ions from the plasma arriving at the substrate are bombarding the growing film with a higher kinetic energy which consequently results in a higher temperature. The same argumentation can be used to explain the increasing substrate temperature with increasing bias voltage (Fig.2c). It should be noted that the tolerable substrate temperatures for the deposition of hard coatings on e.g. temperature-sensitive steels are often limited to 180 °C [37].

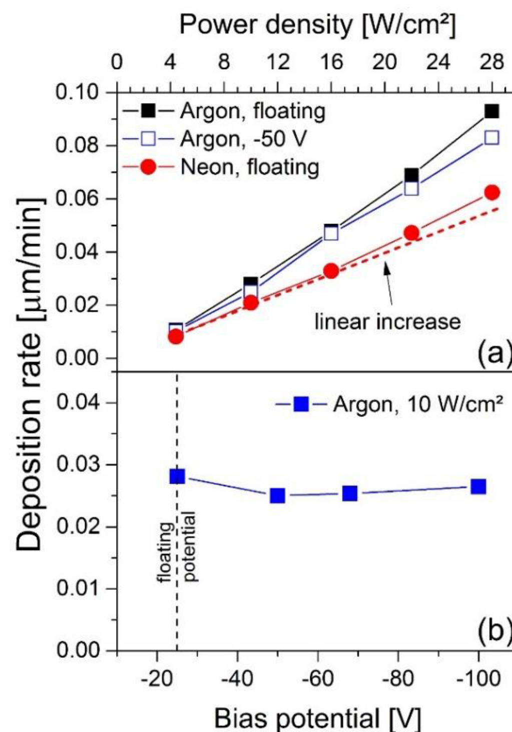

Figure 3: Deposition rate as a function of the power density for the coatings deposited in Ar at floating potential and at a bias potential of -50 V and Ne at floating potential (a) as well as of the bias voltage for coatings deposited in Ar at a power density of 10 W/cm² (b). The dashed line in (a) indicates a hypothetical linear increase of the deposition rate with power density.

When the power density at the target is raised, the current of inert gas ions bombarding the target is concurrently increased as well. This leads to a higher amount of sputtered atoms, consequently increasing the deposition rate of the coatings, see Fig.3a. However, the increase was found to be slightly superlinear with power density in all three cases. The reason for this is most probably a decrease in the density of the coatings. Savvides and Window [10] and Cho

et al. [13] reported a decreased density of a-C coatings grown at higher sputtering powers. Cho et al. assigned the decrease in the density to atomic scale voids present at higher power densities. Mounier et al. found that a higher substrate temperature results in a decreased density of the coatings [16]. Similarly, in the case of arc evaporated coatings Chhowalla et al. [24] reported that increasing the substrate temperature results in an enhanced deposition rate due to a lower mass density. This was attributed to the transformation of high density sp^3 bonded a-C towards the sp^2 bonded type. Although sputter deposited a-C coatings are generally characterized by a small amount of sp^3 bonds [1], this effect might nevertheless have some influence (see also Raman results in section).

The bias potential on the other hand only has a small influence on the deposition rate (Fig.3a and 3b), where just a small decrease for a bias potential of -50 V compared to floating potential was found. Further increasing the bias potential, however, does not lead to a significant change. Two effects can be considered leading to the lower deposition rate with bias: Firstly, the enhanced ion bombardment leads to a densification of the film, as reported by various authors [12,38–40]. Secondly, re-sputtering of the deposited material might take place during deposition, thus decreasing the net amount of deposited atoms.

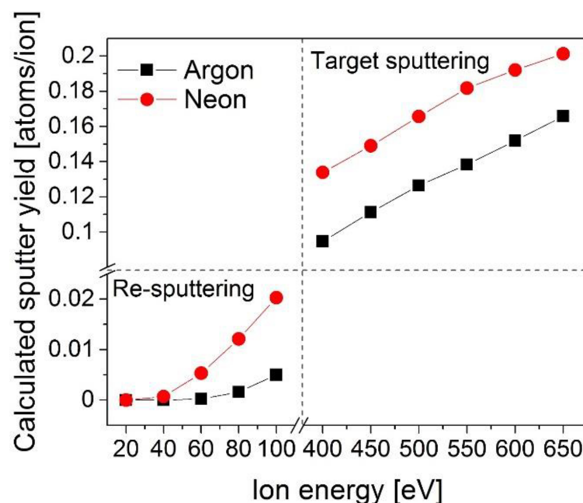

Figure 4: Sputter yields of C exposed to Ar and Ne ion bombardment for ion energy ranges relevant for the sputtering at the target and re-sputtering at the substrate, calculated with TRIM.

In order to assess the second argument, sputtering yields of carbon under Ar and Ne bombardment at incident ion energies relevant for re-sputtering at the substrate were calculated using the Monte-Carlo simulation software “TRIM”. The outcome of these computations are shown in the lower left corner of Fig.4. They revealed that the sputter yield of C subjected to Ar ion bombardment with an energy below -100 V is very low ($\lesssim 0.005$). Also,

if re-sputtering would be the main reason for the lower sputtering yield at higher bias, the deposition rate would decrease with increasing bias. Since this is obviously not the case (see Fig.3b), re-sputtering can be excluded as an important factor for the observed behavior.

Although a higher deposition rate for Ne compared to Ar would be expected at the same power according to literature [15], an opposite behavior was observed within the present work. TRIM calculations also support the assumption of a higher deposition rate in the case of Ne. For target voltages of -600 V and -475 V, which correspond to the target voltages observed at a discharge power of 10 W/cm² for Ar and Ne, respectively, the calculated sputtering yield is with ~0.15 practically the same, see Fig.4. Since the discharge voltage for Ne is lower at the same power density, however, a higher discharge current compared to Ar evolves. Therefore, an elevated sputtering and deposition rate is expected, which is, however, not observed. Three effects are possible explanations for this behavior: (1) coating densification, (2) re-sputtering of the growing atoms and (3) scattering in the gas phase. The ion bombardment of the coating during the deposition in Ne is more intense compared to Ar [15] leading to a densification of the film, as argued above. Also, re-sputtering is more likely compared to the deposition in Ar (sputter yield = 0.005, see Fig.4). However, this is not very pronounced and both effects cannot explain the 30 % lower deposition rate in the case of Ne. Consequently, a more pronounced scattering in the gas phase must be the determining factor for the lower deposition rate in the case of Ne. This is partly due to the higher deposition pressure. The more important reason, however, is the much more efficient energy transfer from energetic C atoms to Ne compared to Ar. The elastic energy transfer coefficient $\Delta E/E$ is given by [34]

$$\frac{\Delta E}{E} = \frac{4m_1m_2}{(m_1+m_2)^2}, \tag{4}$$

where ΔE is the transferred energy, E is the initial energy of species 1 and m_1 and m_2 are the masses of the two colliding species. The transfer coefficients of C with Ar and Ne are 0.71 and 0.94, respectively. The more pronounced energy transfer in the case of Ne leads to a higher degree of thermalization. Therefore, the sputtered carbon atoms are scattered into all directions, which hence decreases the deposition rate at the substrate compared to Ar.

3.2 Coating microstructure and properties

ERDA was carried out on selected samples to determine the amount of inert gas atoms incorporated within the coatings. Figure 5 displays the Ar and Ne contents of the investigated coatings as a function of the power density and bias potential. In case of deposition on a floating substrate, the inert gas content was found to be below 1 at.-% and to decrease with

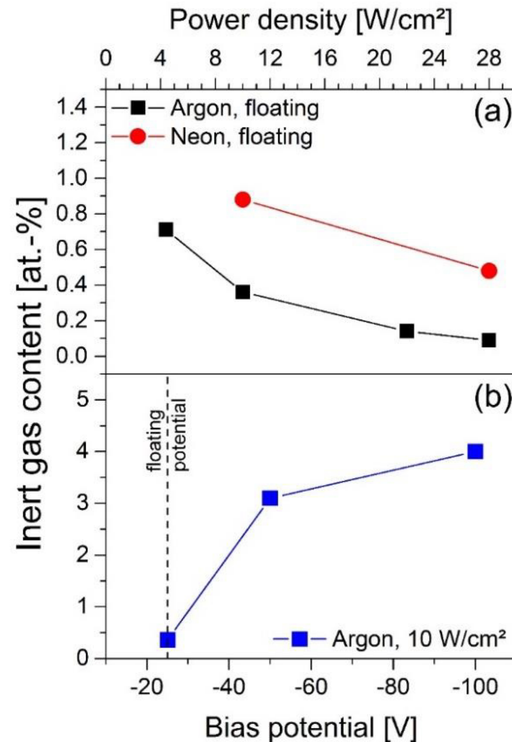

Figure 5: Inert gas (Ar and Ne) content in the synthesized a-C coatings as a function of the power density (a) and bias potential (b) of selected depositions determined by ERDA.

power density. This effect can be explained by the adsorption and desorption of gases on surfaces, which strongly depends on pressure and temperature [41]. The pressure during the depositions was constant when the power was varied, while the temperature increased. Therefore, adsorption is hindered while desorption is enhanced at higher power densities [41]. Furthermore, diffusion is more pronounced at elevated temperatures which enables sub-planted atoms to diffuse to the surface and re-evaporate there. Thus, the higher temperature leads to a lower amount of incorporated inert gas atoms at higher power density. The Ne content in the coatings, although being deposited at greater temperatures, are noticeably higher. This is an indication for the more intense ion bombardment during growth mentioned above [15]. This leads to an enhanced Ne incorporation into the coatings, even though the temperatures are considerably higher. With increasing bias voltage the inert gas content significantly increases from below 0.5 at.-% at floating potential to around 4 at.-% at a bias potential of -100 V (Fig.5b). This is in accordance with previous studies [12,42,43], where an increased amount of inert gas with bias potential was found for various coating systems.

The cross sections of the coatings deposited in Ar and Ne at the lowest and highest power densities of 4.4 and 28 W/cm², respectively, are displayed in Fig.6. It can be seen that

all coatings have thicknesses of approximately 2 µm. However, the coatings deposited at 28 W/cm² are somewhat thicker, which indicates a decreased density at higher discharge powers. In case of the coatings sputtered in Ne, the base layer deposited in Ar for adhesion improvement can be recognized as an area with different contrast. Both coatings deposited at 4.4 W/cm² do not exhibit any features in the fracture cross section, which is typical for amorphous or nanocrystalline structures. The coatings deposited at 28 W/cm² on the other hand show some minor features, which might be an indication for a somewhat higher crystallinity. However, no grain boundaries or columnar structures typical for sputter deposited crystalline coatings [44] can be identified.

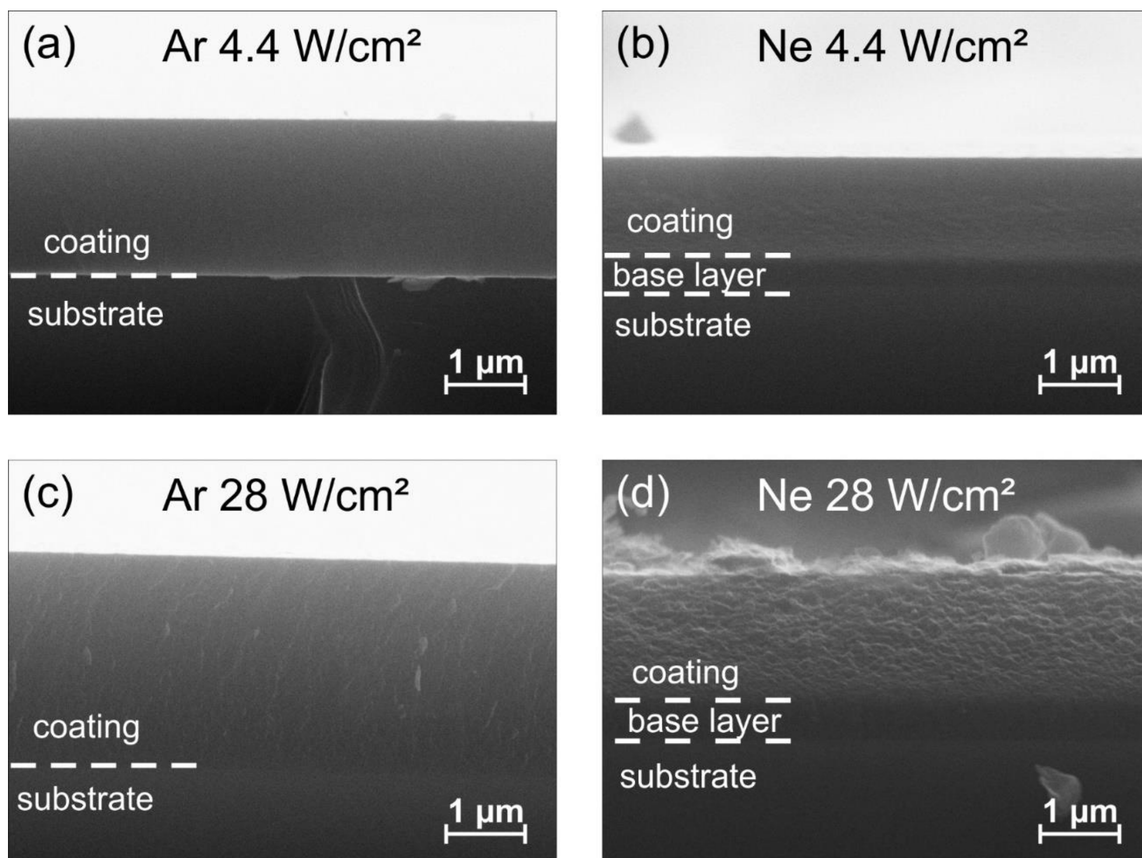

Figure 6: SEM cross sectional images of the coatings deposited at the lowest and highest power densities in Ar and Ne.

The results of the evaluation of the obtained Raman spectra are shown in Fig.7. The position of the G-peak ranges from 1550 to 1580 cm^{-1}, while the intensity ratio of the D-peak over the G-peak $I(D)/I(G)$ is in the range of 0.7 to 1.1. These values correspond to stage 2 a-C in the three structure model proposed by Ferrari and Robertson [27]. Such coatings consist of a combination of nanocrystalline graphite clusters and areas of disordered carbon rings and are characteristic for sputtered a-C coatings [1,18,23,45]. In stage 2 carbon, the sp^2 phase is

by far the dominant one and the amount of sp^3 bonding observed is comparatively low (< 10 %) [1,18].

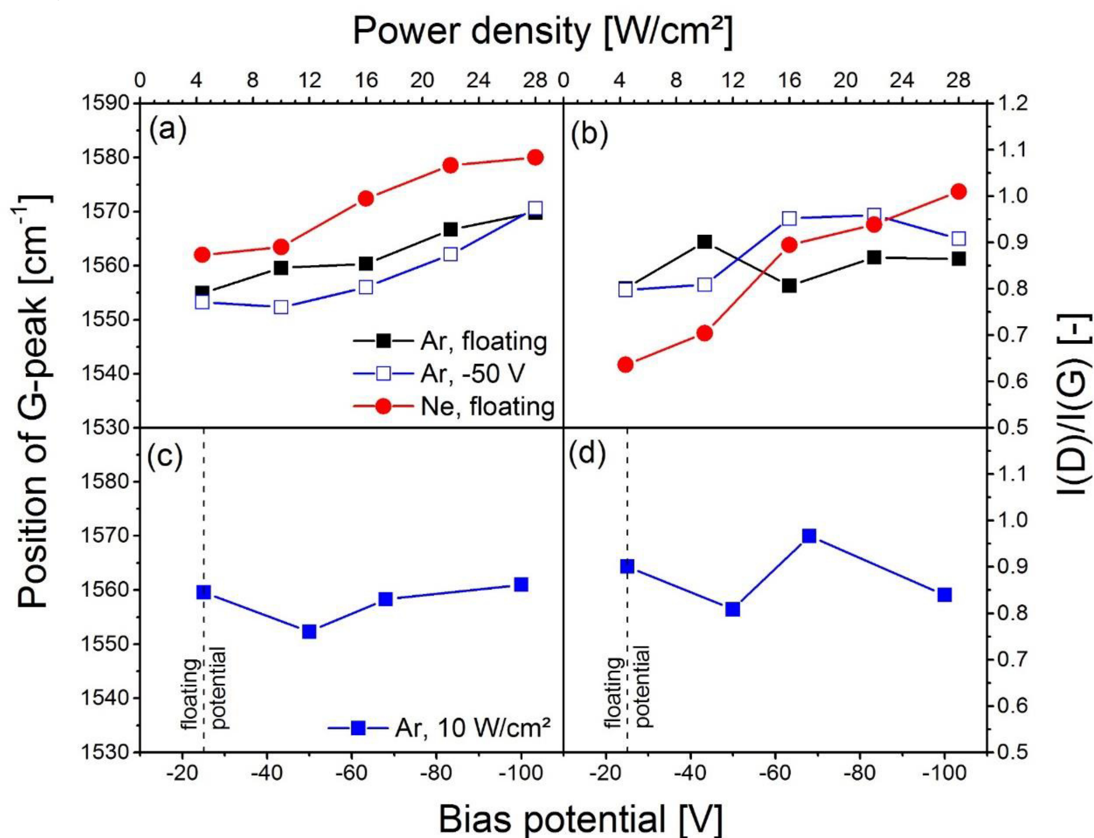

Figure 7: Results of the Raman evaluation procedure as described in 2.2. (a) and (b) show the position of the G-peak and the intensity ratio of the D-peak over the G-peak as a function of the power density for the coatings deposited in Ar at floating potential and at a bias potential of -50 V, and Ne at floating potential. (c) and (d) present the same parameters for the bias variation at a power density of 10 W/cm² in Ar.

Figure 7 indicates that the G-position rises with power density in all cases, while $I(D)/I(G)$ only shows a slight increase. This corresponds to a decreased number of defects and to larger [27] or an increased number of clusters [46]. The coating evolves from a highly defected, i.e. amorphous structure towards a higher crystallinity. Furthermore, the increase of both, G-position and $I(D)/I(G)$, indicates that the amount of sp^3 bonds, although being generally very low for sputtered a-C, is by trend decreasing. The increase of clusters and consequent loss of sp^3 bonds with increasing power density is a result of the elevated substrate temperature [21,23,46]. With enhanced thermal activation, the annealing of defects is favored and larger clusters evolve.

The influence of the bias on the G-position and $I(D)/I(G)$ is shown in Figs. 7c and 7d. Both values appear to be essentially unaffected by the bias potential. Although a disordering

due to the energetic particle bombardment would generally be expected for increasing ion energy [21], no clear change of the two parameters is observed. This can be explained by the fact that substrate temperature and ion bombardment are competitive effects [21]. The increased temperature during deposition, see Fig.2c, promotes a higher crystallinity, while the energetic particles favor the generation of an amorphous structure. Consequently, both effects tend to cancel out and the microstructure remains essentially unaffected.

In order to qualitatively assess the residual stress level of the coatings, wafer curvature measurements were carried out with the results presented in Fig.8. Generally, residual stresses in coatings are comprised of three contributions, namely extrinsic, intrinsic and thermal stresses [42]. The extrinsic stresses result from epitactic misfits and adsorbing molecules from the environment and can be neglected in sputtered a-C coatings [12]. The intrinsic stresses are generated during the growth of the coating and the thermal stresses are induced during cooling after deposition [42].

$$\sigma_{th} = \frac{E_C}{1-\nu_C} \cdot (\alpha_s - \alpha_C) \cdot (T - T_D) \quad (3)$$

can be used for the estimation of the thermal stress σ_{th}, where E_C is the elastic modulus of the coating, ν_C is the coating´s Poisson´s ratio, α_s and α_C are the thermal expansion coefficients of the substrate and the coating, respectively, T is the temperature, and T_D is the deposition temperature. Since the substrate temperature was not constant during deposition (see Fig.2), assessing the exact amount of the thermal stress is not possible. However, with this equation it is possible to roughly estimate the thermal stresses. For this purpose we calculated the maximum difference in thermal stress $\Delta\sigma_{th} = \sigma_{th,1} - \sigma_{th,2}$ for the coatings deposited at the highest and lowest power densities. E_C was determined by nanoindentation and an average value for each coating of the power density variations was used. ν_C was estimated to be 0.2 [47] and the thermal expansion coefficient of graphite was used (20.0 × 10^{-6} K^{-1}) [48] for the coating, while the thermal expansion coefficient of the substrate is that of Si (2.7 × 10^{-6} K^{-1}) [49]. For T_D the maximum deposition temperature reached during deposition was inserted (see Fig.2). The thus obtained value only represents an upper limit for the thermal stress induced, since the temperature difference during deposition was not constant over the deposited layer thickness. The calculation resulted in tensile thermal stress values of 270, 390 and 650 MPa for the power density variations performed in Ar at floating potential and a bias of -50 V and in Ne at floating potential, respectively. An analogous calculation for the bias variation resulted in a maximum difference of the thermal stress of 290 MPa. These values were used for the error bars in Fig.8, which therefore do not represent

a statistical measurement error, but rather an estimation of the error introduced by the different deposition temperatures. As can be seen, the thermal stress difference is small compared to the absolute value of the stress. Therefore it can be assumed that the qualitative trend follows the intrinsic stress evolution with reasonable agreement.

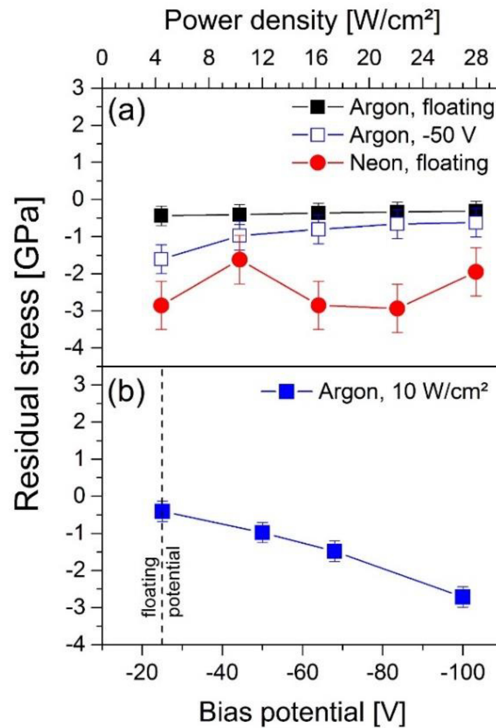

Figure 8: Total residual stress as a function of the power density (a) and bias potential (b). The error bars indicate the maximum difference in thermal stress that may have been induced during cooling for each set of depositions, calculated with equation 3 (see text for further details).

It can be seen from Fig.8 that all coatings exhibit compressive residual stresses. The stress level of the coatings deposited in Ar at floating potential is lowest at around -300 to -450 MPa (see Fig.8a). For the coatings deposited in Ar the variations of stress with power density are small. Some minor decrease of the stress with power can be found, which is probably due to the induced thermal tensile stresses. The coatings deposited in Ne show the highest residual stress values in the range of -1.5 to -3 GPa. These high values can be explained by the pronounced ion bombardment during film growth [15], which consequently increases the amount of defects. These coatings do not exhibit a clear evolution with power density, but show a pronounced scattering around approximately -2.5 GPa. Overall, however, the intrinsic stress level remains constant over the power density for all three power density variations. Similar results were reported for comparable conditions by Mounier and Pauleau (Ar with a base pressure of 1 Pa) [11] and by Rubin et al. (Ar, 1.33 Pa) [19]. They have found constant residual compressive stresses in a-C coatings when increasing the sputtering power by a factor

of 4 [11] and even 100 [19]. When a bias voltage is applied the compressive stresses increase (see Fig.8b), which is a result of the enhanced bombardment by ions producing a larger amount of defects [44]. Furthermore, the amount of incorporated working gas increases with bias as evidenced by ERDA (Fig.5). The incorporation of the large Ar atoms distorts the lattice and consequently compressive stresses evolve. Thus, the residual stresses are elevated to around -3 GPa when the bias is increased to -100 V.

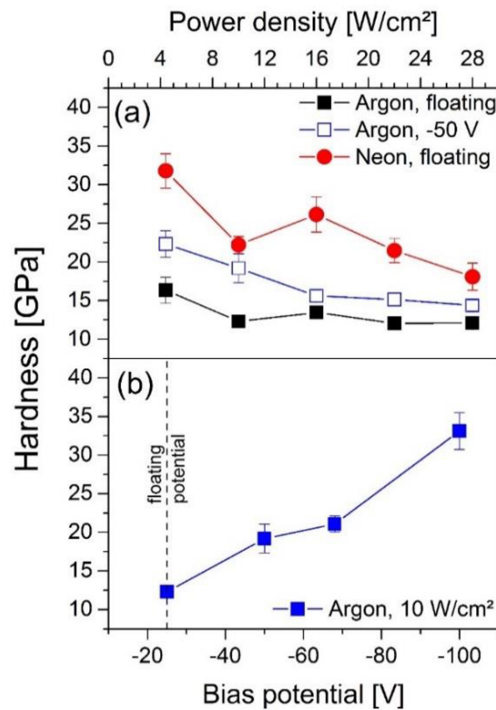

Figure 9: Coating hardness as a function of the power density (a) and bias potential (b).

Figure 9 shows the hardness of the investigated coatings. The influence of bias potential and sputtering gas on the hardness evidently resembles their influence on the residual stress. Both hardness and stress strongly increase with bias potential and when the gas is changed from Ar to Ne. While the hardness is comparatively low without bias ($\lesssim$ 20 GPa), applying a bias voltage of -100 V results in values above 30 GPa. Similar values can also be reached by the use of Ne instead of Ar. This is owing to the high compressive stresses, which are generally known to increase the hardness of sputtered coatings [44]. However, in contrast to the residual stress, the hardness is not constant over the power density but substantially decreases in all cases. The coatings deposited in Ne show the strongest drop of 15 GPa from 4.4 W/cm² to 28 W/cm². As can be seen from the Raman results, the coatings evolve from an amorphous microstructure towards higher crystallinity, i.e. larger clusters, with power density. This change is accompanied by a decrease of the hardness [13]. Furthermore, as stated above the amount of sp^3 bonding and the density of the coatings are decreasing with

power, which results in lower hardness as well [1,13]. The microstructural changes can be attributed mainly to the different thermal loads during deposition. Because the difference in substrate temperature was highest for the coatings deposited in Ne, the largest change in the mechanical properties can be found for these coatings.

4. Conclusions

Amorphous carbon coatings were deposited in Ar and Ne discharges at power densities between 4.4 and 28 W/cm² and at different bias potentials using an unbalanced d.c. magnetron sputtering system. Irrespective of the used process gas or applied bias potential, coating density and inert gas content in the coatings decrease with rising power density, while a simultaneous increase of the graphite cluster size was observed. These microstructural changes are a result of the more pronounced thermal load of the coatings during film growth at elevated power densities. In contrast, the residual stress was not affected by the power density but is strongly connected with the energetic particle bombardment during deposition. At the most intense energetic bombardment conditions, i.e. with Ne as process gas, or when a bias potential of -100 V was applied, the residual stress increases to values around -3 GPa. At these high compressive stresses, hardness values of more than 30 GPa were observed. In contrast to the stresses, the hardness was not constant over the power density, but a considerable drop due to the microstructural changes was found. In conclusion it can be stated, that increasing the power is a potential way to increase deposition rate and productivity of the magnetron sputter deposition of amorphous carbon coatings. However, the thermal load increases simultaneously, which causes microstructural changes within the coatings, the consequent deterioration of the hardness as well as possible softening of temperature sensitive substrate materials. Hence, additional measures need to be taken to control the thermal load on the substrates at elevated power densities in order to fully benefit from the higher deposition rate achieved by raising the discharge power.

5. Acknowledgements

This work was financially supported by the Austrian Federal Government (in particular from Bundesministerium für Verkehr, Innovation und Technologie and Bundesministerium für Wissenschaft, Forschung und Wirtschaft) represented by the Österreichische Forschungsförderungsgesellschaft mbH within the project SmartCoat-Eco (project number 843621).

6. References

[1] J. Robertson, Mat. Sci. Eng. R 37 (2002) 129–281.

[2] C.V. Deshpandey, J. Vac. Sci. Technol. A 7 (1989) 2294.

[3] Y. Lifshitz, Diam. Relat. Mater. 8 (1999) 1659–1676.

[4] A. Grill, Diam. Relat. Mater. 8 (1999) 428–434.

[5] G. Dearnaley, J.H. Arps, Surf. Coat. Technol. 200 (2005) 2518–2524.

[6] C. Donnet, A. Erdemir, Tribology of Diamond-like Carbon Films: Fundamentals and Applications, Springer (2008) New York, USA.

[7] R. Hauert, Tribol. Int. 37 (2004) 991–1003.

[8] H. Tsai, D.B. Bogy, J. Vac. Sci. Technol. A 5 (1987) 3287–3312.

[9] A.H. Lettington, Carbon 36 (1998) 555–560.

[10] N. Savvides, B. Window, J. Vac. Sci. Technol. A 3 (1985) 2386–2390.

[11] E. Mounier, Y. Pauleau, J. Vac. Sci. Technol. A 14 (1996) 2535–2543.

[12] E. Mounier, Y. Pauleau, Diam. Relat. Mater. 6 (1997) 1182–1191.

[13] N.-H. Cho, K.M. Krishnan, D.K. Veirs, M.D. Rubin, C.B. Hopper, B. Bhushan, D.B. Bogy, J. Mater. Res. 5 (1990) 2543–2554.

[14] L.G. Jacobsohn, F.L. Freire, J. Vac. Sci. Technol. A 17 (1999) 2841–2849.

[15] I. Petrov, I. Ivanov, V. Orlinov, J. Kourtev, J. Jelev, Thin Solid Films 185 (1990) 247–256.

[16] E. Mounier, F. Bertin, M. Adamik, Y. Pauleau, P.B. Barna, Diam. Relat. Mater. 5 (1996) 1509–1515.

[17] S. Seo, D.C. Ingram, H.H. Richardson, J. Vac. Sci. Technol. A 13 (1995) 2856–2862.

[18] A.C. Ferrari, A. Libassi, B.K. Tanner, V. Stolojan, J. Yuan, L.M. Brown, S.E. Rodil, B. Kleinsorge, J. Robertson, Phys. Rev. B 62 (2000) 11089–11103.

[19] M. Rubin, C.B. Hopper, N.-H. Cho, B. Bhushan, J. Mater. Res. 5 (1990) 2538–2542.

[20] E. Mounier, P. Juliet, E. Quesnel, Y. Pauleau, Surf. Coat. Technol. 76-77 (1995) 548–552.

[21] A.A. Onoprienko, V.V. Artamonov, I.B. Yanchuk, Surf. Coat. Technol. 200 (2006) 4174–4178.

[22] J. Vetter, M. Stüber, S. Ulrich, Surf. Coat. Technol. 168 (2003) 169–178.

[23] L. Shaginyan, A. Onoprienko, V. Britun, V. Smirnov, Thin Solid Films 397 (2001) 288–295.

[24] M. Chhowalla, J. Robertson, C.W. Chen, S.R.P. Silva, C.A. Davis, G.A.J. Amaratunga, W.I. Milne, J. Appl. Phys. 81 (1997) 139–145.

[25] P. Losbichler, C. Mitterer, Surf. Coat. Technol. 97 (1997) 567–573.

[26] J.F. Ziegler, J.P. Biersack, M.D. Ziegler, URL http://www. srim.org (2013).

[27] A.C. Ferrari, J. Robertson, Phys. Rev. B 61 (2000) 14095–14107.

[28] C. Saringer, M. Tkadletz, C. Mitterer, Surf. Coat. Technol. 274 (2015) 68–75.

[29] G. Janssen, M.M. Abdalla, F. van Keulen, B.R. Pujada, B. van Venrooy, Thin Solid Films 517 (2009) 1858–1867.
[30] W.C. Oliver, G.M. Pharr, J. Mater. Res. 7 (1992) 1564–1583.
[31] I. Petrov, I. Ivanov, V. Orlinov, J. Kourtev, Contrib. Plasm. Phys. 30 (1990) 223–231.
[32] B. Szapiro, J.J. Rocca, J. Appl. Phys. 65 (1989) 3713–3716.
[33] S.Z. Wu, J. Appl. Phys. 98 (2005) 83301.
[34] B.N. Chapman, Glow Discharge Processes: Sputtering and Plasma Etching, John Wiley and Sons (1980) New York, USA.
[35] W.D. Westwood, Sputter Deposition, AVS (2003) New York, USA.
[36] F. Soddy, A.J. Berry, P. Roy. Soc. Lond. A Mat. 83 (1910) 254–264.
[37] A.J. Perry, D.G. Teer, Surf. Coat. Technol. 97 (1997) 244–249.
[38] Y. Pauleau, Vacuum 61 (2001) 175–181.
[39] M.A. Tamor, W.C. Vassell, J. Appl. Phys. 76 (1994) 3823–3830.
[40] S. Logothetidis, M. Gioti, P. Patsalas, C. Charitidis, Carbon 37 (1999) 765–769.
[41] H. Lüth, Solid Surfaces, Interfaces and Thin Films, 4th ed., Springer (2001) Berlin, Germany.
[42] H. Oettel, R. Wiedemann, Surf. Coat. Technol. 76-77 (1995) 265–273.
[43] J.J. Cuomo, R.J. Gambino, J. Vac. Sci. Technol. 14 (1977) 152–157.
[44] P.H. Mayrhofer, C. Mitterer, L. Hultman, H. Clemens, Prog. Mater. Sci. 51 (2006) 1032–1114.
[45] O. Jantschner, S.K. Field, D. Music, V.L. Terziyska, J.M. Schneider, F. Munnik, K. Zorn, C. Mitterer, Tribol. Int. 77 (2014) 15–23.
[46] R. O. Dillon, John A. Woollam, and V. Katkanant, Phys. Rev. B 29 (1984) 3482–3489.
[47] J. Robertson, Surf. Coat. Technol. 50 (1992) 185–203.
[48] Pierre Villars (Chief Editor), PAULING FILE in: Inorganic Solid Phases, SpringerMaterials (online database), C gra hex thermal expansion (Springer, Heidelberg, 2016), http://materials.springer.com/isp/physical-property/docs/ppp_029729, accessed June 2017.
[49] Pierre Villars (Chief Editor), PAULING FILE in: Inorganic Solid Phases, SpringerMaterials (online database), Si rt thermal expansion (Springer, Heidelberg, 2016), http://materials.springer.com/isp/physical-property/docs/ppp_105073, accessed June 2017.

Publication IV

Restrictions of stress measurements using the curvature method by thermally induced plastic deformation of silicon substrates

Christian Saringer, Michael Tkadletz, Christian Mitterer

Surface and Coatings Technology 274 (2015) 68-75

Restrictions of stress measurements using the curvature method by thermally induced plastic deformation of silicon substrates

Christian Saringer[a,b,*], Michael Tkadletz[b], Christian Mitterer[a]

[a] Department of Physical Metallurgy and Materials Testing, Montanuniversität Leoben, Franz-Josef-Strasse 18, 8700 Leoben, Austria

[b] Materials Center Leoben Forschung GmbH, Roseggerstrasse 12, 8700 Leoben, Austria

Abstract

Within this study, the effect of plastic deformation of coated single-crystalline silicon substrates on stress measurement of hard coatings by the curvature method was illuminated. Silicon substrates with different thicknesses (380 and 500 µm) and orientations ((100) and (111)), coated with TiN and TiAlN, were examined and compared to each other with respect to their high-temperature plasticity. The curvature was measured during thermal cycling and isothermal annealing. Coated samples were additionally annealed in vacuum and subsequently characterized using scanning and transmission electron microscopy. The presence of plastic deformation of the silicon substrate was confirmed after thermal exposure by the detected high dislocation density. The resolved shear stress in the 500 µm thick substrate at 600 °C was calculated to 25 MPa, which is in the range of the critical value of silicon at this temperature. Plastic substrate deformation, corroborated by experimental and theoretical approaches, is thus a significant source of error in estimating residual stress from curvature measurements performed at elevated temperatures or applied to coatings with pronounced stresses grown at moderate/high substrate temperatures.

* Corresponding author:
E-mail address: christian.saringer@unileoben.ac.at
Tel.: +43/3842 402 4239
Fax: +43/3842 402 4202

1. Introduction

Thin hard coatings of e.g. transition metal nitrides or carbides are commonly used to enhance the wear and oxidation resistance of tools or components [1]. Frequently, they are deposited by physical vapor deposition, which typically generates residual stresses within the coatings [2,3]. These residual stresses influence the properties of coatings, and therefore their performance to a great extent [2,4–7]. Compressive residual stresses for example hinder crack propagation, because they reduce harmful tensile stresses generated under mechanical or thermal loads [2]. However, in order to optimize the lifetime of coated tools or components, knowledge of the coating stress state is of vital importance. A frequently used method for the determination of the residual stress is the so-called curvature method, which has recently been reviewed by Janssen et al. [8,9]. As a result of the residual stress in the coating, a flexible substrate becomes elastically deflected. This is used by the curvature method to determine the biaxial residual stress, using the modified Stoney equation [10]. The major advantage of this technique is its simple applicability to both, crystalline and amorphous coatings. Thus, it is frequently used to determine the stress evolution *in situ* during film growth [11,12]. Also, the samples can be placed on a heating device within a vacuum chamber, which enables the *ex situ* determination of the temperature dependence of the stress, also referred to as biaxial stress-temperature measurement (BSTM) [13]. This allows the investigation of stress relaxation effects, that occur at elevated temperatures due to annihilation of defects, as well as the calculation of the coefficient of thermal expansion (CTE) of the coating [14–16]. However, there are also disadvantages of this method which need to be mentioned: the measured stress is only averaged over the film thickness and thus stress gradients are not considered. Furthermore, the elastic properties of the film are not taken into account when using the Stoney equation, which may lead to large errors in the case of comparatively thick coatings [17,18]. This is particularly true when the elastic constants of film and substrate differ strongly from each other.

A typical BSTM curve determined for a Cr/CrN bilayer coating grown by sputter deposition at a substrate temperature T_D of 350 °C on a Si (100) strip is shown in Fig.1. During heating, the compressive stress first changes thermo-elastically due to the different CTEs of coating and substrate. The slope is either negative, if the CTE of the coating is larger than that of the substrate (as shown in Fig.1), or positive in the opposite case. At temperatures exceeding T_D, the stress starts to relax as a result of the annihilation of defects generated by the deposition process, often referred to as recovery [13]. During cooling, the stress again decreases thermo-elastically with decreasing temperature, with a slope that is parallel to the

heating curve, provided that phase transformation, recrystallization or decomposition processes have not taken place.

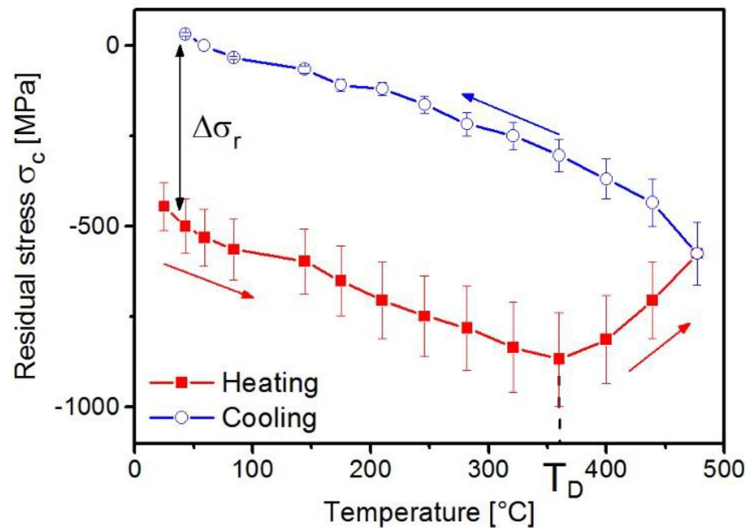

Figure 1: Stress-temperature dependence of a Cr/CrN bilayer coating grown at a deposition temperature T_D of 350 °C onto Si (100) substrates. The curve represents a single measurement. The error bars refer to the experimental error, resulting from coating thickness and substrate curvature measurements, which is estimated to ~15 %. Due to recovery of coating defects above T_D, the residual stress in the coating decreases by $\Delta\sigma_r$.

Within this work, the temperature dependence of the residual stress of sputtered hard coatings on single crystalline Si was investigated to elucidate an unexpectedly large deflection of the substrate observed at high temperatures/residual stress. Samples were additionally annealed in vacuum and subsequently investigated with scanning electron microscopy (SEM) and transmission electron microscopy (TEM). Furthermore, a mathematical relation to calculate the maximum stress in the substrate was deduced from mechanical force and momentum equilibria, to compare the maximum resolved shear stress in the substrate to the critical resolved shear stress of Si at elevated temperatures. Finally, experimental difficulties in performing curvature measurements at elevated temperatures for hard coatings with a thickness of a few microns are addressed, along with the validity of the modified Stoney equation for such coatings.

2. Experimental methods

One TiN and two TiAlN coatings were reactively deposited using an industrial scale, unbalanced magnetron sputter deposition plant type CemeCon CC800/9MLT. This device is equipped with four bipolarily pulsed DC magnetrons of size 500 × 88 mm². The deposition temperature T_D was 500 - 550 °C. Additional information about the deposition process can be found in [19] and [20]. The single-crystalline Si substrates were strips of size 21 × 7 mm, with thicknesses of 380 and 500 µm for (100) and 380 µm for (111) orientation. Coatings were deposited at bias voltages of -40 V (TiAlN) and -50 V (TiN, TiAlN). The thickness of the TiN coating, as measured by ball cratering, was 4.7 µm on the (100) and 5.1 µm on the (111) oriented Si, while the TiAlN coatings had thicknesses of 5.4 µm (-40 V bias, substrate thickness 380 µm) and 5.6 µm (-50 V bias, substrate thicknesses 380 and 500 µm), respectively. The chemical composition of both, the TiN and TiAlN coatings were close to stoichiometry, with an Al/(Ti+Al) atomic ratio of ~0.6 for the TiAlN coating, determined with energy dispersive X-ray spectroscopy (EDX). X-ray diffraction (XRD) indicated that both coatings had a single-phase face-centered cubic crystal structure. Furthermore, a Cr/CrN bilayer coating was deposited in an industrial scale unbalanced magnetron sputtering system type Oerlikon Balzers Rapid Coating System at T_D = 350 °C in DC mode. A planar Cr target with a diameter of 145 mm was used to coat (100) oriented Si strips with a thickness of 380 µm. The Cr base layer had a thickness of 2 µm and was deposited with a bias of -40 V, while the 3 µm thick CrN layer was grown at -80 V [21]. The Al_2O_3 coatings used for the temperature calibration were grown by thermally activated chemical vapor deposition, which had a thickness of 8 µm on a 10 µm TiCN base layers [22,23].

BSTMs were carried out on a home-made device utilizing the reflection of two parallel laser beams provided by a He-Ne laser (λ = 632.8 nm), to determine the curvature radius of the samples. The distance between the two laser beams on the samples was 15 mm with an overall travel path after reflection of 2,720 mm. The residual stress was then calculated by means of the modified Stoney equation [10,24]:

$$\sigma_c = M_s \cdot \frac{d^2}{6 \cdot t \cdot R} \quad (1)$$

There, σ_c denotes the mean stress in the coating, d and t are the thicknesses of the substrate and the coating, R is the determined radius of curvature and M_s is the biaxial modulus of the substrate, which depends, in the case of single-crystalline materials on the orientation [24]. For Si, the biaxial moduli are 2.29×10^{11} Pa for the (111) orientation and 1.80×10^{11} Pa for the

(100) orientation [8]. The presented stress-temperature curves are each results of single measurements. Hence, the error bars refer to the experimental error of the stress measurements and the determination of the coating thickness, which is assumed to be no more than 15 % in total. They were added to the data points where no plastic deformation takes place and stress values are thus reliable. The samples were placed in a vacuum chamber (base pressure < 5 × 10^{-3} Pa) on a ceramic Si_3N_4 heating plate (see Fig.2a), which enables to investigate the temperature dependence of the coating stress up to a sample temperature of ~650 °C. A homogenous temperature distribution on the heating device is of vital importance, particularly when more than one sample is measured at the same time. Moreover, the precise knowledge of the sample temperature is crucial in order to achieve accurate results. Therefore, a diligent temperature calibration was conducted. The temperature homogeneity was investigated using an infrared camera of type Titanium SC 7500MB from FLIR, with the AltaIR software for analysis. The emissivity of radiation was assumed to be 0.95, which is a reasonable value for Si_3N_4 for a wavelength up to 8 µm [25]. A BaF_2 glass was used as an infrared transmitting window into the vacuum chamber. Subsequently, an additional temperature calibration was performed by melting pure metals (In, Sn, Pb) and comparing the measured melting temperatures with literature values.

The coating thickness was determined by means of the ball cratering technique using a CSM Calowear instrument. The ball size was 30 mm with a 1 µm diamond dispersion, grinding for ~2.5 min. The evaluation of the residual crater size and the microscopic investigation were conducted on a Polyvar MET light microscope. The error in the coating thickness measurement for coatings with thicknesses in the µm-range is no more than 5 % [26].

Additionally, samples were annealed in a vacuum furnace type HTM Reetz at a base pressure ≤ 5 × 10^{-4} Pa. The annealing temperatures were between 800 and 1000 °C in steps of 50 °C and the annealing time at maximum temperature was 15 min. The heating rate was 20 °C/min.

The SEM imaging and the sample preparation for the TEM investigation were conducted on a SEM Zeiss SMT Auriga, which is equipped with a field emission gun. The installed EDAX Apollo 40+ EDX detector was used to determine the chemical composition of the coatings. The bright-field TEM images were taken with a Tecnai F20, which is also equipped with a field emission gun, operated at 200 kV. The samples for TEM were prepared using a focused ion beam extension, type Orsay Physics Cobra Z-05, attached to the SEM. XRD investigations were

conducted on a Bruker-AXS D8 Advance diffractometer in grazing incidence configuration with an inclining angle of 2°, using Cu K_α-radiation.

3. Temperature calibration

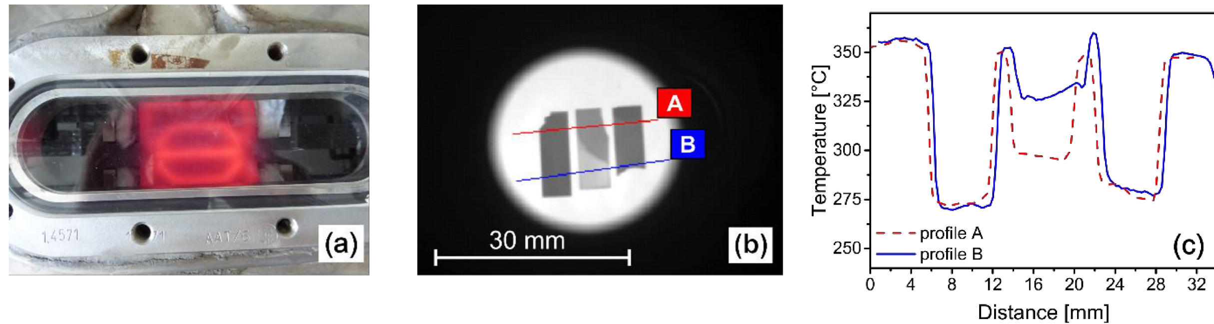

Figure 2: Temperature calibration of the heating plate in the BSTM system; (a) Si_3N_4 heating plate during heating, (b) temperature distribution of three Si strips placed on the heating plate, as measured with the infrared camera, (c) temperature profiles as indicated in (b).

The temperature distribution obtained by the infrared measurements on samples placed in the BSTM device is shown in Fig.2. Three samples were placed on the Si_3N_4 heating plate (Fig.2a), one uncoated and polished Si sample and two Si samples with an α-Al_2O_3/TiCN bilayer coating. The temperature of the heating plate was set to 350 °C and investigated after a waiting period of 20 min for temperature homogenization. Figure 2b evidences a homogenous temperature distribution on the heating plate; only a minor change in the recorded intensity is detectable outside the sample area. Unlike the two coated samples, the Si strip in the center shows an inhomogeneous temperature distribution, which is due to reflection of infrared radiation within the vacuum chamber. Therefore, the recorded temperature on the uncoated sample does not correspond to its actual temperature, and has no meaning for the measurement. Although the emissivity of the other two coated samples is not exactly known, it is obvious that they have a significantly lower temperature than the heating plate. This vast difference in intensity, and thus also in temperature, stems from limited heat transfer, mainly because of two reasons:

i. Convective heat transfer is excluded due to the absence of a required medium. This assumption was fostered by additionally performed tests under ambient pressure, which revealed that the temperature is raised by ~50 °C compared to vacuum conditions. However, elevated temperature measurements at ambient pressure will result in undesired sample oxidation.

ii. Similar to convection, heat conduction is not pronounced either. The samples, in particular with coatings under high stress resulting in pronounced bending, have only limited contact to the heating plate, which leads to a large thermal resistance between the samples and the heating plate.

Thus, heat transfer from the heating plate to the samples can be assumed to mainly occur via radiation. Consequently, it is not sufficient to solely measure the heating plate temperature, but the sample temperature needs to be determined as well. Within this work, this was achieved by an uncoated and thus flat reference Si sample that was positioned on the heating device during measurement, with a thermocouple placed on its top. However, also the heat transfer from the Si substrate to the thermocouple is not ideal and therefore a smaller temperature value than the actual one is measured. In order to determine the precise values, In, Sn and Pb were placed on a Si sample and subsequently melted. The measured melting temperatures of these metals were compared to their corresponding literature values [27], see Table 1. There is still a difference of up to ∼30 °C between the measured and the real melting temperatures, which is attributed to the mentioned non-ideal contact conditions. Therefore, the temperatures provided by the thermocouple placed on the Si reference sample were corrected by 30 °C.

Table 1: Difference T_{diff} between the melting temperature from literature T_{lit} and the melting temperature measured in the BSTM device $T_{measured}$ of various metals used for temperature calibration.

Metal	**T_{lit} [°C]**	**$T_{measured}$ [°C]**	**T_{diff} [°C]**
In	156.4	127	29.4
Sn	231.8	216	15.8
Pb	327.0	295	32

4. Results and discussion

BSTM curves of the TiAlN coatings deposited with different bias voltages on (100) Si with different thicknesses are shown in Fig.3a. During heating, a linear thermo-elastic stress increase is visible, which is a result of different CTEs of coating and substrate [28,29]. At higher temperatures close to T_D, in particular near 500 °C for the coatings on the 380 µm and 600 °C for the coating on 500 µm substrate, however, the stress is apparently strongly increasing. This is entirely in contrast to the anticipated stress reduction, initiating at or slightly above T_D, due to annihilation of defects in the coating [13]. The reason for this dramatically increasing

deflection observed at elevated temperatures cannot be understood in terms of thermo-elasticity, defect annihilation and recovery or even recrystallization, representing origins for thermally driven changes in the stress state. Furthermore, XRD measurements yielded that no spinodal decomposition of the metastable cubic TiAlN solid solution [30] has taken place during thermal exposure. Thus, phase changes can also be excluded as possible reason for this deformation. The origin of this unexpected substrate deformation is discussed in the following sections.

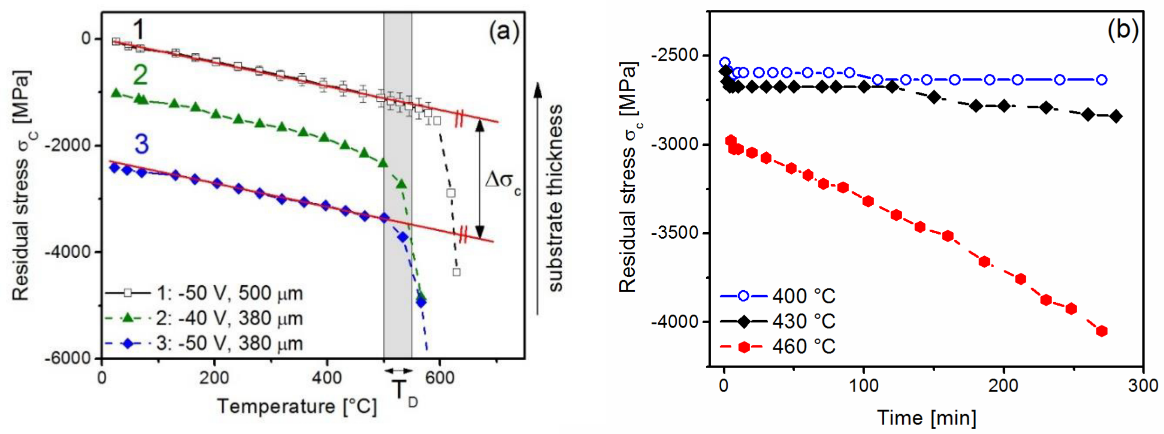

Figure 3: Stress-temperature measurements of TiAlN coatings deposited on Si (100) substrates at a deposition temperature T_D of 500-550 °C; (a) BSTM curves for coatings deposited with two different bias voltages and on two different substrate thicknesses, (b) isothermal tests performed at 400, 430 and 460 °C for TiAlN coatings deposited on 380 µm thick (100) Si at -50 V bias voltage. Each curve is the result of a single measurement. The error bars refer to the experimental error, resulting from coating thickness and substrate curvature measurements, which is estimated to ~15 %. They were added where valid stress values were measured due to the absence of plastic substrate deformation.

In general, the total residual stress σ_{tot} in coatings consists of three contributions, namely the intrinsic σ_i, the thermal σ_{th} and the extrinsic stresses σ_e [3]:

$$\sigma_{tot} = \sigma_i + \sigma_{th} + \sigma_e \quad (2)$$

σ_e, which stems mainly from structural misfits, relaxes by misfit dislocations within the first few atomic layers and can thus be neglected [2,3]. Likewise, σ_{th} is zero at T_D, because it is generated during cooling after deposition due to the different CTEs of substrate and coating [3,28]. σ_{th} is not affected by the substrate thickness and therefore equal for the samples 1 and 3 in Fig.3a. Hence, also the change in σ_{th} with temperature is the same, which is evidenced by the parallel lines in Fig 3a. It can also be assumed that the coating growth conditions are the same for both samples, as both were grown in the same deposition run with the Si strips

mounted on adjacent positions. Thus, also σ_I has to be presumed to be equal for samples 1 and 3. Figure 3a, however, shows that there is a vast stress difference of ~2200 MPa between these samples, denoted as $\Delta\sigma_C$. Curve 1 reveals an intrinsic stress value determined at the deposition temperature of roughly - 1100 MPa, while curve 3 yields an apparent intrinsic stress of ~ - 3300 MPa. Following the arguments above, the large stress difference has to be attributed to effects occurring in the substrate, where the huge increase in curvature above T_D might be a result of plastic deformation taking place during the deposition process itself. After deposition, the plastic deformation is still present and the curvature of the plastically deformed sample is higher compared to an only elastically deformed sample. Consequently, an apparent stress value considerably larger than the actual one is measured. In Fig.3a, samples 2 and 3 grown at slightly different bias voltages show a similar stress-temperature behavior, despite of the initial deflection level. Both samples are characterized by a parallel thermo-elastic increase of the stress with a subsequent onset of plastic deformation at ~500 °C. Because of its compressive stress level well above sample 1 (-50 V bias, 500 µm thick Si substrate), it is likely that sample 2 (-40 V bias, 380 µm thick Si substrate) has already plastically deformed during coating deposition. However, plastic deformation during deposition or during the measurements at elevated temperatures disables an accurate stress determination, as the Stoney formula does not consider plasticity of the substrate. Therefore, the determined stress values are not valid above the onset temperature for plastic deformation, or if the substrate has already plastically deformed during the deposition process.

In addition, isothermal stress measurements were performed for a TiAlN coating, sputter deposited with a bias voltage of -50 V on 380 µm thick (100) Si substrates. For BSTM, the temperature was raised within 3 min to constant values of 400, 430 and 460 °C, respectively, and subsequently the deflection was determined as a function of time. Figure 3b indicates that there is a transition from a merely elastic deformation at 400 °C to a constantly ongoing deformation with time, i.e. creep[1], at 460 °C. This measured change in mechanical behavior corresponds to the brittle to ductile transition of silicon, which starts between 400 and 500 °C [31,32]. Therefore, a plastic deformation needs to be expected in this

[1] It needs to be mentioned here that at high temperatures deformation by dislocation movement, i.e. plastic deformation, and by diffusion, i.e. creep, cannot be unambiguously distinguished. Most probably, both mechanisms contribute to the overall deformation observed. Therefore, the terms plastic deformation and creep are here used synonymously.

temperature region for quasi-static loads. However, it has to be noted that this temperature is considerably below the deposition temperature of the coating. Thus, the isothermal measurements also support the assumption of plastic deformation concluded from the BSTM cycles in Fig.3a. The curve in Fig.3b measured for 430 °C additionally shows two regions: A time-independent, i.e. elastic, deformation at first, where the stress stays constant with time, and creep deformation after ∼130 min. Thus, if plastic deformation occurs already during coating synthesis, the deposition time has to be assumed to play a role as well: For low growth rates and thus long deposition times at moderate to high substrate temperatures, the probability of plastic deformation is higher and an accurate measurement of the stress is becoming more and more problematic. Consequently, it has to be concluded that extremely high stress levels apparently determined by the curvature method can be disturbed by plastic

Figure 4: TiAlN (bias voltage: -50 V) coated Si (100) strips with a thickness of 380 µm after 15 min vacuum annealing at different temperatures.

substrate deformation.

To expand the annealing temperature to higher values than those available in the BSTM device, TiAlN coated 380 µm thick (100) Si samples were annealed in a vacuum furnace in the temperature range from 800 to 1000 °C. The samples show a strong deflection after annealing, see Fig.4, similar as after BSTM. It is evident that this deformation is proportional to the temperature, as it would be expected for plastic deformation. Due to softening of the Si substrate at elevated temperatures and simultaneous thermal stress increase, the resulting stress in the substrate exceeds its yield strength, consequently leading to its plastic deformation. This is more pronounced the higher the temperature is, owing to the decreasing critical resolved shear stress of Si [31,33–35]. An additionally conducted microscopic investigation of the sample annealed at the highest temperature yielded that neither buckling nor delamination occur, which might falsify the measured stress as well.

In order to confirm plastic deformation of the Si substrate after thermal exposure, SEM images of the fracture cross-section of the TiAlN coated 380 µm thick (100) Si sample after vacuum annealing at 1000 °C were taken (Fig.5a). There, the visible plane is perpendicular to

the (011) direction. The fracture cross-section is characterized by parallel lines that exhibit a constant angle with the surface, forming visible V-shaped features. The parallel lines are attributed to traces of the slip planes, on which dislocations are moving during plastic deformation, as also observed for Si in Ref. [32]. Face-centered cubic materials such as Si favorably have a {111}<110> slip system, where {111} represents the planes with the highest lattice plane spacing and <110> the directions with the smallest atomic distance, respectively [36]. Thus, the parallel lines are traces of the {111} planes. Corresponding <110> Burger's vectors are indicated in Fig.5a.

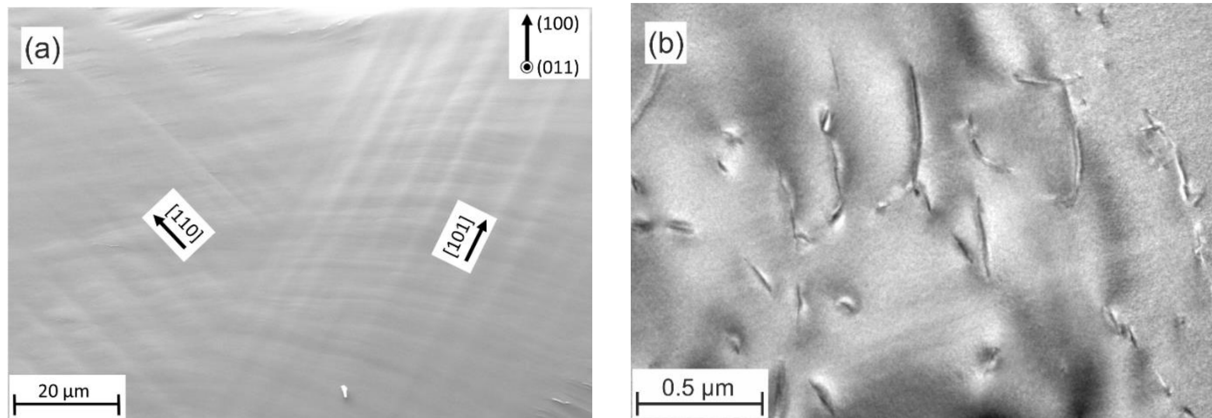

Figure 5: TiAlN (bias voltage, -50 V) coated Si (100) strips with a thickness of 380 µm after vacuum annealing at 1000 °C for 15 min; (a) SEM micrograph of the (011) fracture cross-section and (b) bright-field TEM micrograph of the $(0\bar{1}1)$ direction of the Si substrate.

TEM lamellas were prepared parallel as well as perpendicular to the fracture cross-section shown in Fig.5a, both being {110} oriented. Bright-field TEM images were then taken, which revealed a similar appearance for both directions. An image taken from the lamella prepared perpendicular to the fracture cross-section is shown in Fig.5b. As the substrates are single-crystalline and manufactured by crystal pulling with subsequent floating zone process [37], a low number of dislocations in the as-received state can be expected [38]. Figure 5b, in contrast, shows a rather high dislocation density, confirming plastic deformation of the Si substrate. Despite the high dislocation density, recrystallization does obviously not take place at the temperatures applied [39], which is evidenced by the absence of grain boundaries in the SEM cross-section in Fig.5a.

To investigate the effect of substrate orientation on its plastic deformation and thus, to explore the possibility to extend BSTMs to higher stresses and/or temperatures, TiN coatings were deposited on Si strips with (111) and (100) orientation, respectively. Figure 6 indicates that apparently both substrates are plastically deforming at higher temperatures. However, the plastic deformation of the (111) sample is less pronounced and a small coating stress

relaxation effect, starting at a temperature of ∼470 °C (i.e. before the onset of plastic substrate deformation, which occurs at ∼530 °C), is detectable. In the (100) substrate, on the other hand, plastic deformation takes place already at 500 °C. There is no evidence for coating stress relaxation, since it is superimposed by plastic deformation, and the elastic region of the curve seems to be extended. This different behavior observed for the substrate orientations is related to their different elastic properties. The biaxial modulus of (111) Si is 229 GPa, which is larger than the biaxial modulus of (100) Si, being 180 GPa [8]. In general, higher elastic constants reduce the creep rate, being inversely proportional to the shear modulus [40] and, hence, also to the biaxial modulus. Due to the anisotropy of Si with a difference in the modulus of 27 %, the thermo-elastically linear range can thus be extended to higher temperatures for the (111) compared to the (100) orientation.

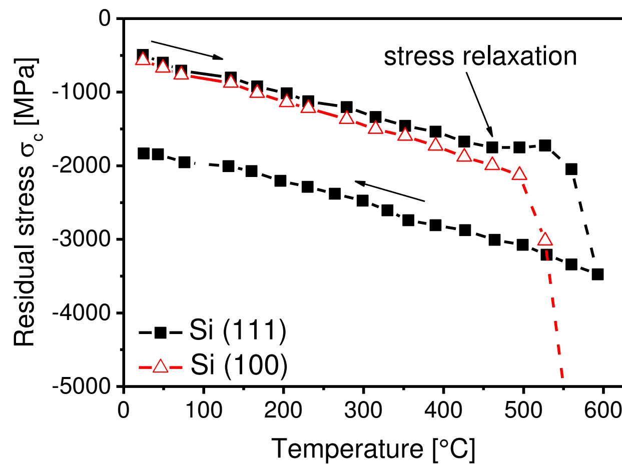

Figure 6: Stress-temperature measurements of a TiN coating deposited at 500 - 550 °C on 380 µm Si strips with two different orientations. Both curves are results of single measurements. The error bars refer to the experimental error, resulting from coating thickness and substrate curvature measurements, which is estimated to ∼15 %. They were added where valid stress values were measured due to the absence of plastic substrate deformation.

The maximum stress in the [110] direction of the substrate σ_{max} can be calculated considering the equilibria of mechanical forces and momenta (see Appendix). This procedure yields the following simple relationship:

$$\sigma_{max} = -4 \cdot \sigma_c \cdot \frac{t}{d}, \quad (3)$$

where σ_c is the coating stress, t is the coating thickness and d is the substrate thickness. Plastic deformation in the substrate occurs when the resolved shear stress equals a critical value [33]. Therefore, the resolved shear stress in the substrate was calculated for curve 1 in Fig.3a and

compared to the critical resolved shear stress at high temperature. This particular sample obviously starts to plastically deform at ~600 °C, where the stress value in the coating is ~1400 MPa. If this value is inserted into equation (3) with the corresponding thickness of 5.5 µm for the coating and 500 µm for the substrate, the maximum calculated stress is about ~62 MPa. In order to evaluate the amount of this stress which contributes to the movement of dislocations, it has been resolved to the <110>{111} primary slip system of fcc. This was done by applying Schmid´s law [40] under the assumption that the different slip planes do not influence each other during the deformation. The necessary Schmid factor was determined to be $1/\sqrt{6}$. Hence, the resolved shear stress is $1/\sqrt{6} \cdot \sigma_{max}$, or 25 MPa for this specific case. This value corresponds well with the critical resolved shear stress of Si, which has been reported to be slightly above this value, in the region of a few ten MPa at 600 °C [33]. However, at higher temperature plastic deformation is likely to occur at lower stresses than the theoretical values, owing to time-dependent effects, see also Fig.3b. The occurrence of plastic deformation is thus also corroborated from a theoretical point of view.

Figure 7 gives a graphical representation of this subject for three different t/d-ratios. The limit of σ_c where the substrate deforms plastically was calculated using the calculation procedure demonstrated above with the critical values from Ref. [33]. The results of these calculations are represented by solid curves, being the upper limit of the colored areas in the figure. However, when performing stress measurements it is necessary to have a σ_c well below this critical value in order to prevent plastic deformation due to time-dependent effects, such as creeping. This consequently limits the applicability of the curvature method on Si to considerably lower stress values. For the given t/d-ratios the colored areas represent the range of temperature below the theoretical maximum coating stress where plastic deformation is still likely to evolve during the curvature measurement, or deposition process as well. At a given temperature Si can hence safely be used as a substrate material for stress measurement only when the coating stress is below the lower limit of each area, which is indicated by a dotted line. These lower stress limits were chosen regarding to the experimentally found values shown in Figs.3 and 6.

As a final point, it needs to be recapitulated that due to the averaged coating stress and the omission of the coating´s elastic constants, Stoney´s equation is only a rough approximation for coating/substrate thickness ratios higher than ~1 %, where the bending of the substrate may generate a considerable amount of stress in the coating [17]. The errors in the calculation may become excessively large at high coating/substrate thickness ratios, or when the elastic constants of coating and substrate differ to a considerable extent [17,18]. In

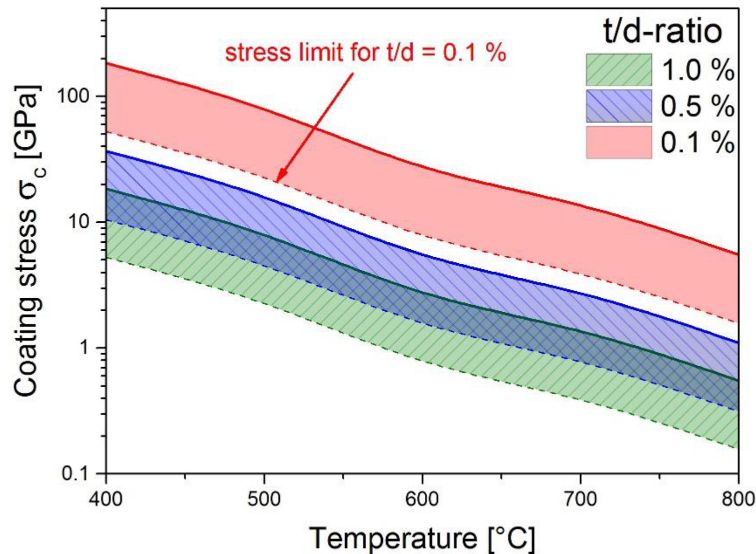

Figure 7: Maximum advised coating stress for different coating to substrate thickness ratios t/d (dotted lines) in order to avoid plastic substrate deformation as a function of the temperature. The colored areas represent the zone where plastic deformation is likely to arise even below the critical resolved shear stress (solid lines) due to time-dependent effects. The coating stress limit for the applicability of the curvature method is exemplarily indicated with an arrow for a t/d ratio of 0.1 %.

the case treated above, for example, the error resulting from the coating/substrate thickness ratio of ~1.1 % and from the difference in elastic constants (Young´s modulus of TiAlN ~450 GPa [6], biaxial modulus of (100) Si ~180 GPa [8]) is already 10 - 15 % [17]. This can be assumed as a considerable error and the validity of Stoney´s approach is thus questionable. Nevertheless, coating thickness and Young´s modulus are in the range of typical values for hard coatings, and the curvature method with Si as substrate is commonly used in the hard coatings community due to its simplicity and practicability. However, it needs to be decided for every specific situation whether the error estimated by Stoney´s equation is tolerable or not.

5. Conclusions

Biaxial stress-temperature measurements using the curvature method are commonly performed to determine the temperature dependence of the residual stresses in hard coatings. In this study, limitations of this technique are addressed. When silicon is used as substrate material, it works well for coatings deposited at low temperatures or with low residual stress. However, at elevated temperature during coating deposition or stress measurement, plastic deformation of the substrate may occur, which falsifies the stress values obtained by the modified Stoney formula.

Finally, two approaches to expand the applicability of the curvature method are suggested:

i. Choosing substrate orientations with higher biaxial modulus, e.g. (111) instead of the commonly used (100) orientation of silicon, leads to an increased resistance against plastic deformation. This is hence a suitable approach for measurements on highly stressed coatings grown at moderate to high substrate temperatures or for measurements at elevated temperatures.

ii. From the derived relation between coating stress and maximum stress in the substrates, it is inferred that the maximum stress level can be reduced by changing the ratio of substrate to coating thickness. This can be achieved by a) increasing the substrate thickness and/or b) decreasing the coating thickness, in order to prevent the substrate from plastic deformation. It is important to consider, however, that the sensitivity of the method is decreased simultaneously, due to a smaller deflection of the samples.

6. Acknowledgment

Parts of this work were financially supported by the Austrian Federal Government (in particular from Bundesministerium für Verkehr, Innovation und Technologie and Bundesministerium für Wissenschaft, Forschung und Wirtschaft) represented by Österreichische Forschungsförderungsgesellschaft mbH and the Styrian and the Tyrolean Provincial Government, represented by Steirische Wirtschaftsförderungsgesellschaft mbH and Standortagentur Tirol, within the framework of the COMET Funding Programme and by the Österreichische Forschungsförderungsgesellschaft mbH within the project SmartCoat-Eco (project number 843621). Dr. Beata Oswald-Tranta and Roland Schmidt (Chair of Automation, Montanuniversität Leoben) are gratefully acknowledged for assistance with the temperature calibration. The authors would also like to thank Dr. Rostislav Daniel (Chair of Functional Materials and Materials Systems, Montanuniversität Leoben) for fruitful discussions. The Al_2O_3 coated samples were provided by CERATIZIT Austria GmbH, Reutte, Austria.

7. Appendix

A relation to calculate the maximum stress in the substrate was derived from mechanical force and momentum equilibria [8,41], to enable a comparison of the present stress with the critical resolved shear stress of Si. The derivation of the relation is based on two assumptions:

1. The coating is thin compared to the substrate. Therefore, the coating stress can be assumed to be constant over the coating thickness [42].
2. The stress in the substrate is linearly decreasing from the interface [8,18,43].

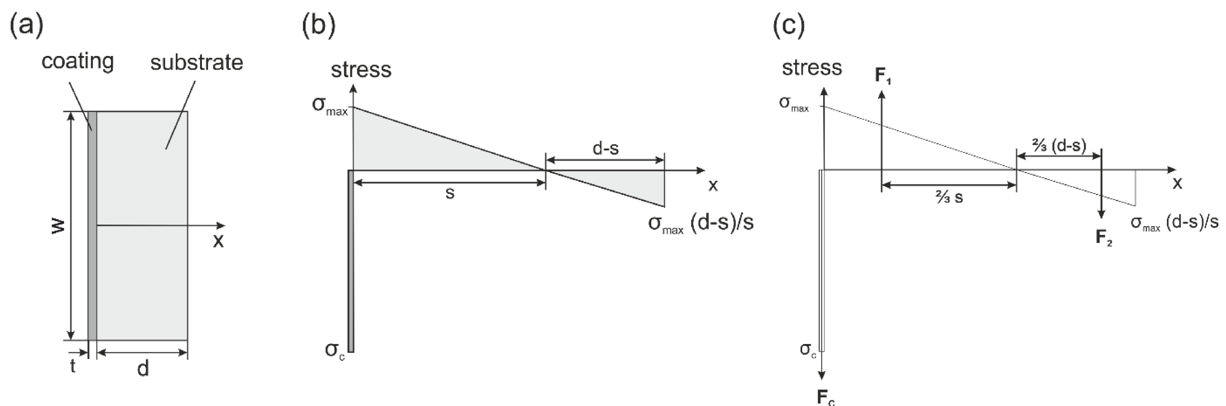

Figure 8: (a) Schematic of a cross-section of a coated substrate, (b) stress-depth profile and (c) forces corresponding to the acting stresses.

A schematic cross-section of a coated sample with the resulting stress distribution is shown in Figs.8a and b. There, σ_c is the stress in the coating, σ_{max} is the maximum stress in the substrate, *t* and *d* are the thicknesses of the coating and the substrate, respectively, and *w* is the width of the sample. The distance between the interface and the point of zero stress is indicated with *s*. This stress distribution results in the equivalent forces F_1, F_2 and F_c, see Fig.8c. The forces F_1 and F_2 apply in a distance from the point of zero stress that is 2/3 of the width of the corresponding triangular stress distribution. There are two unknown parameters, σ_{max} and s, that are calculated using the equations of the corresponding force equilibrium

$$F_1 = F_C + F_2 \tag{A.1}$$

and momentum equilibrium with respect to the point of zero stress

$$F_C \cdot s = \frac{2}{3} \cdot F_1 \cdot s + \frac{2}{3} \cdot F_2 \cdot (d - s). \tag{A.2}$$

The forces are linked to the stresses with their equivalent cross-section areas. Inserting the stresses and the cross-sections yields

$$\frac{1}{2} \cdot \sigma_{max} \cdot s \cdot w = \sigma_c \cdot t \cdot w + \frac{1}{2} \cdot \sigma_{max} \cdot \frac{d-s}{s} \cdot (d-s) \cdot w \quad \text{(A.3)}$$

for the force equilibrium and

$$\sigma_c \cdot s \cdot t \cdot w = \frac{2}{3} \cdot \frac{1}{2} \cdot \sigma_{max} \cdot w \cdot s^2 + \frac{2}{3} \cdot \frac{1}{2} \cdot \sigma_{max} \cdot \frac{(d-s)^3}{s} \cdot w \quad \text{(A.4)}$$

for the momentum equilibrium. Crossing out w and rearranging equation (A.3) leads to the following expression for σ_{max} (Note that σ_{max} is compressive when the coating stress is tensile and vice versa. Therefore, a minus sign is added in A.5):

$$\sigma_{max} = - \frac{2 \cdot \sigma_c \cdot t}{s - \frac{(d-s)^2}{s}}. \quad \text{(A.5)}$$

By inserting equation (A.5) into equation (A.4) and once again crossing out w and rearranging the formula, an expression for s can be formed:

$$s = \frac{2}{3} \cdot d. \quad \text{(A.6)}$$

This simple relationship correlates exactly with the distance between the point of zero stress and the interface recorded in [8] and [18]. The last unknown is σ_{max}, which can now easily be calculated by inserting equation (A.6) into equation (A.5). Subsequent rearrangement yields:

$$\sigma_{max} = - 4 \cdot \sigma_c \cdot \frac{t}{d}. \quad \text{(A.7)}$$

8. References

[1] U. Schleinkofer, C. Czettl in: V.K. Sarin (Ed.), Comprehensive Hard Materials, Elsevier (2014) Oxford, UK, pp. 453–469.

[2] H. Oettel, R. Wiedemann, Surf. Coat. Technol. 76-77 (1995) 265–273.

[3] R. Daniel, K.J. Martinschitz, J. Keckes, C. Mitterer, Acta Mater. 58 (2010) 2621–2633.

[4] T.Z. Kattamis, M. Chen, S. Skolianos, B.V. Chambers, Surf. Coat. Technol. 70 (1994) 43–48.

[5] O. Gonzalo, V. García Navas, B. Coto, I. Bengoetxea, U. Ruiz de Gopegi, M. Etxaniz, Procedia Engineer. 19 (2011) 106–111.

[6] T. Sprute, W. Tillmann, D. Grisales, U. Selvadurai, G. Fischer, Surf. Coat. Technol. 260 (2014) 369–379.

[7] C. Mitterer, P.H. Mayrhofer, J. Musil, Vacuum 71 (2003) 279–284.
[8] G.C.A.M. Janssen, M.M. Abdalla, F. van Keulen, B.R. Pujada, B. van Venrooy, Thin Solid Films 517 (2009) 1858–1867.
[9] G.C.A.M. Janssen, Thin Solid Films 515 (2007) 6654–6664.
[10] G.G. Stoney, Proc. R. Soc. Lond. A 82 (1909) 172–175.
[11] E. Chason, B.W. Sheldon, Surf. Eng. 19 (2003) 387–391.
[12] A. Fillon, G. Abadias, A. Michel, C. Jaouen, Thin Solid Films 519 (2010) 1655–1661.
[13] L. Hultman, C. Mitterer, in: A. Cavaleiro, J.T.M. De Hosson (Eds.), Nanostructured Coatings, Springer (2006) New York, USA, pp. 464–510.
[14] K.J. Martinschitz, R. Daniel, C. Mitterer, J. Keckes, Thin Solid Films 516 (2008) 1972–1976.
[15] P.H. Mayrhofer, G. Tischler, C. Mitterer, Surf. Coat. Technol. 142-144 (2001) 78–84.
[16] J.P. Lokker, A.J. Kalkman, H. Schellevis, G.C.A.M. Janssen, S. Radelaar, Microelectron. Eng. 33 (1997) 129–135.
[17] H. Windischmann, K.J. Gray, Diam. Relat. Mater. 4 (1995) 837–842.
[18] A. Mézin, Surf. Coat. Technol. 200 (2006) 5259–5267.
[19] N. Schalk, C. Mitterer, J. Keckes, M. Penoy, C. Michotte, Surf. Coat. Technol. 209 (2012) 190–196.
[20] N. Schalk, T. Weirather, C. Polzer, P. Polcik, C. Mitterer, Surf. Coat. Technol. 205 (2011) 4705–4710.
[21] R. Daniel, K.J. Martinschitz, J. Keckes, C. Mitterer, J. Phys. D. Appl. Phys. 42 (2009) 1–13.
[22] A. Riedl, N. Schalk, C. Czettl, B. Sartory, C. Mitterer, Wear 289 (2012) 9–16.
[23] N. Schalk, C. Mitterer, C. Czettl, B. Sartory, M. Penoy, C. Michotte, Tribol. Lett. 52 (2013) 147–154.
[24] W. Nix, Metall. Trans. A 20A (1989) 2217–2245.
[25] N.M. Ravindra, S. Abedrabbo, W. Chen, F.M. Tong, A.K. Nanda, A.C. Speranza, IEEE Trans. Semicond. Manuf. 11 (1998) 30–39.
[26] K. Nitzsche, Schichtmeßtechnik, Vogel (1997) Würzburg, Germany.
[27] R.B. Ross, Metallic Materials, Chapman and Hall (1968) London, UK.
[28] M. Ohring, The Materials Science of Thin Films, Academic Press, (1992) New York, USA.
[29] M.F. Doerner, W.D. Nix, Crit. Rev. Solid State 14 (1988) 225–268.
[30] A. Hörling, L. Hultman, M. Odén, J. Sjölén, L. Karlsson, J. Vac. Sci. Technol. A 20 (2002) 1815–1823.
[31] L.J. Vandeperre, F. Giuliani, S.J. Lloyd, W.J. Clegg, Acta Mater. 55 (2007) 6307–6315.
[32] J. Tan, S.X. Li, Y. Wan, F. Li, K. Lu, Mater. Sci. Eng. B 103 (2003) 49–56.

[33] A. Fischer, T. Grabolla, H. Richter, G. Obermeier, P. Krottenthaler, R. Wahlich, Microelectron. Eng. 45 (1999) 209–223.

[34] A. Moulin, M. Condat, L.P. Kubin, Acta Mater. 47 (1999) 2879–2888.

[35] M´b. Omri, C. Tete, J.-P. Michel, A. George, Philos. Mag. A 55 (1987) 601–616.

[36] D. Hull, D.J. Bacon, Introduction to Dislocations, 4th ed., Elsevier (2001) Oxford, UK.

[37] http://www.crystec.de/silizium-d.html, accessed 03. December 2014.

[38] K.T. Wilke, Kristallzüchtung, VEB Deutscher Verlag der Wissenschaften (1973) Berlin, Germany.

[39] J.D. Verhoeven, Fundamentals of Physical Metallurgy, John Wiley & Sons (1975) New York, USA.

[40] G. Gottstein, Physical Foundations of Materials Science, Springer, (2004) Berlin Germany, 2004.

[41] K. Röll, J. Appl. Phys. 47 (1976) 3224–3229.

[42] J.D. Wilcock, D.S. Campbell, Thin Solid Films 3 (1969) 3–12.

[43] A. Brenner, S. Senderoff, J. Res. Nat. Bur. Stand. 42 (1949) 105–123.